Università degli Studi di Catania

Doctoral Thesis

Microwave accelerating structures: an innovative parallel coupled electron LINAC

Author:
Giovanni Castorina

Supervisor:
Prof. Gino Sorbello

Co-Supervisor:
Dr. Bruno Spataro

A thesis submitted in fulfilment of the requirements
for the degree of Doctor of Philosophy

in

Ingnegneria dei Sistemi, Energetica, Informatica e delle Telecomunicazioni

November 2017

Declaration of Authorship

I, Giovanni Castorina, declare that this thesis titled, 'Microwave accelerating structures: an innovative parallel coupled electron LINAC' and the work presented in it are my own. I confirm that:

- This work was done wholly or mainly while in candidature for a research degree at this University.
- Where any part of this thesis has previously been submitted for a degree or any other qualification at this University or any other institution, this has been clearly stated.
- Where I have consulted the published work of others, this is always clearly attributed.
- Where I have quoted from the work of others, the source is always given. With the exception of such quotations, this thesis is entirely my own work.
- I have acknowledged all main sources of help.
- Where the thesis is based on work done by myself jointly with others, I have made clear exactly what was done by others and what I have contributed myself.

Signed: _____

Date: _____

UNIVERSITÀ DEGLI STUDI DI CATANIA

Abstract

Ingnegneria dei Sistemi, Energetica, Informatica e delle Telecomunicazioni

Doctor of Philosophy

Microwave accelerating structures: an innovative parallel coupled electron LINAC

by Giovanni CASTORINA

Particle accelerators are employed in many fields of the physics, engineering and medicine science. Although the idea of acceleration of charged particles by means of time varying electromagnetic field is an almost century old, the research and development in this field is active more than ever. An efficient particle accelerator gives the opportunity to reach energy levels not yet achieved and allows the study of the deepest laws of the physics. Also a better performance of the particle accelerators is desirable in order to develop compact table-top machine for medical or industrial purpose. The work here presented takes place in this framework. A parallel coupled electron LINAC has been studied for high gradient operation in the X-band frequency. This kind of device can address some issues of high gradient accelerating LINAC. Due to decoupled propagation axes for RF power and beam it is possible to increase the structure shunt impedance without affecting the cell to cell coupling, combining the advantages of travelling and standing wave structures. Besides in case of a breakdown only the energy stored in one cell is involved in the discharge process and not the total energy stored of the section, thus the damages caused by the breakdown event are expected to be smaller. Following a discussion on how the proposed configuration was conceived, full wave simulations were carried out to numerically validate the idea and to optimize the single cell in order to minimize the probability of breakdowns. After a successful cold simulation a beam dynamics analysis has been done in order to estimate the properties of the beam moving inside the device. Due to the small irises dimension the transverse wakefield can be source of instability for the bunch propagation. Therefore this issue has been investigated by means of numerical methods. Finally, the problem of the beam alignment with respect to the accelerating section is addressed and the results of a device suitable to beam position measurement are presented.

Acknowledgements

This work is made possible thanks to the help of many people. Firstly I would to express my gratitude to my supervisors, Prof. Gino Sorbello, who helped me with his deep knowlodege of electromagnetism in writing this dissertation and, Dr. Bruno Spataro, who taught (and keep teach) me the physics of a such complex topic like particle accelerators.

During these years I was lucky enough to meet qualified people in this field. In particular I would to thank Dr. Valery Dolgashev, Dr. Mikhail Zobov and Dr. Claudio Marcelli for their useful and helpful suggestions.

I am also grateful to the SPARC_LAB people which gave me the opportunity to learn on the field.

Last but not least, I want to thank Marzia for her help and understanding during these years.

Contents

List of Figures

List of Tables

Abbreviations

BBU	**B**eam **B**reak **U**p
BPM	**B**eam **P**osition **M**onitor
DTL	**D**rift **T**ube **L**INAC
FEL	**F**ree **E**lectron **L**aser
FEM	**F**inite **E**lement **M**ethod
HOM	**H**igher **O**rder **M**odes
LINAC	**LIN**ear **AC**celerator
PCAS	**P**arallel **C**oupled **A**ccelerating **S**tructure
RF	**R**adio **F**requency
RHS	**R**ight **H**and **S**ide
LHS	**L**eft **H**and **S**ide
TE	**T**ransverse **E**lectric
TM	**T**ransverse **M**agnetic
TWT	**T**ravelling **W**ave **T**ube

Physical Constants

Speed of Light	c	$=$	$2.997\ 924\ 58 \times 10^{8}\ \mathrm{ms}^{-1}$
Permittivity of Vacuum	ε_0	$=$	$8.854\ 187\ 817 \times 10^{-12}\ \mathrm{Fm}^{-1}$
Permeability of Vacuum	μ_0	$=$	$4\pi\ \times 10^{-7}\ \mathrm{NA}^{-2}$
Elementary Charge	q	$=$	$1.602\ 176\ 6208\ \times 10^{-19}\ \mathrm{C}$
Electron Mass	m_e	$=$	$9.109\ 383\ 56\ \times 10^{-31}\ \mathrm{kg}$
Proton Mass	m_p	$=$	$1.672\ 621\ 898\ \times 10^{-27}\ \mathrm{kg}$
Conductivity of Copper	σ	$\simeq$	$5.98\ \times 10^{7}\ \mathrm{Sm}^{-1}$
Impedance of Free Space	Z_0	$=$	$376.730\ \Omega$

Symbols

Symbol	Name	Unit
α	Attenuation Constant in Waveguide	m^{-1}
α_0	Attenuation Constant	m^{-1}
α_c	Coverage Angle	deg
$\beta = \frac{v}{c}$	Ratio of the particle velocity and speed of light	
β	Coupling Factor	
β_z	Phase constant along z axis	$\mathrm{rads{\cdot}m}^{-1}$
β_m	Betatron Function	m
c_ϵ	Specific Heat	J/K
d	Single Cell Length	m
δ	Skin Depth	m
$\Delta\phi$	Phase Advance per Cell	deg
E_z	Complex Electric Field on Axis	V/m
E_a	Average Accelerating Gradient	V
ϵ_n	Normalized Emittance	mm·mrad
ϵ_{nl}	Energy Spread	eV
η	High Gradient Comprehensive Term	$(\mathrm{W{\cdot}\Omega{\cdot}V}^2)/\mathrm{m}$
η_{TE}	Transverse Impedance for TE mode	Ω
ϕ_c	Phase Advance in Cavity	deg
ϕ_w	Phase Advance in Waveguide	deg
$G_\parallel$	Longitudinal Wake Function	V/C
$G_\perp$	Transverse Wake Function	V/C
$G'_\perp$	Dipole Perpendicular Wake Function	V/C/m
Γ	Reflection Coefficient	
$J_0(\cdot)$	Bessel Function of the First Kind	

k	Thermal Conductivity of the Material	W/(m·K)
k_0	Wavenumber	m^{-1}
K_n	Wavenumber of the n-th Space Harmonic	m^{-1}
$k_{\parallel}$	Loss Factor	V/C
$k_{\perp}$	Kick Factor	V/C/m
I	Current of The Equivalent Circuit	A
L	Section Total Length	m
λ_0	Wavelength in Free Space	m
n	Transformer Ratio	
ω	Angular frequency	$rads^{-1}$
ω_{RF}	Angular Frequency of the RF Signal	$rads^{-1}$
P_{in}	Average Input Power	W
P_{diss}	Average Dissipated Power	W
p_{diss}	Average Dissipated Power per Unit Length	W/m
P_c	Power Dissipated in the cavity	W
P_{ex}	Power Dissipated in the External Load	W
P_s	Scaled Power	W
Q_0	Intrinsic Quality Factor	
Q_{ex}	External Quality Factor	
Q_L	Loaded Quality Factor	
ρ	Density of a Material	kg/m^3
R	Resistance of the Equivalent Circuit	Ω
r^{-1}	Ratio Factor between Phase Advance	
R_s	Surface Resistance	$\Omega \cdot m$
r_s	Shunt impedance	Ω/m
$\frac{r}{Q}$	r over Q	Ω
S_c	Modified Poynting Vector	W/m^2
S_x	Position Sensitivity (x-axis)	
S_y	Position Sensitivity (y-axis)	
σ	Conductivity of a Material	S/m
T	Transit time factor	
τ	Time Constant	s
τ_0	Power Attenuation	

t	Time Variable	s
t_p	RF Pulse Length	s
V	Voltage of the Equivalent Circuit	V
v_0	Velocity of the Synchronous Particle	m/s
v_{ph}	Phase Velocity	rad/s
v_g	Group Velocity	m/s
W	Stored Energy	J
w	Stored Energy per Unit Length	J/m
$W_\parallel$	Longitudinal Wake Potential	V/C
$W_\perp$	Transverse Wake Potential	V/C
Z	Series Impedance	$\Omega \cdot m^2$
Z_c	Cavity Impedance of the Equivalent Circuit	Ω
Z_s	Source Impedance	Ω
$Z_\parallel$	Parallel Coupling Impedance	Ω
$Z_\perp$	Dipole Perpendicular Coupling Impedance	Ω/m

A Marzia

Chapter 1

RF acceleration in LINAC

The accelerators of charged particles are used as tool to study the matter at nuclear or sub-nuclear level. In the last seventy years the experimental outcomes obtained through these machines have been fundamental to develop the Standard Model. The application fields of particle accelerators are several. They are used for cancer treatment or radioisotope production, in the semiconductor industrial field for ions implantation and for Free Electron Laser (FEL).

Theoretical and technological improvements are needed to optimize and extend its application range. On this background, superconducting cavities has been used in order to increase the repetition factor of the machine. The design of a particle accelerator requires the knowledge of many areas of the classical physics and engineering, in particular electromagnetism and mechanics, as well as the special relativity theory. The dissertation topic is the linear accelerator, the abbreviation LINAC will be used in the following. The straight-line trajectory provides high quality beam and avoids the power losses due to synchrotron radiation. In this chapter the main components and the fundamental RF theory of linear accelerators is presented.

1.1 LINAC Structures

The main systems and hardware parts of an electron linear accelerator are summarized in the fig. 1.1. A general description of the main LINAC parts is provided. The electron bunch is generated within a specific device. In the case of thermionic emission a cathode is heated and a continuous flow of electrons is generated. The electrons are commonly accelerated by DC electric field and confined by means of a magnetic field. A chopper (or another bunching mechanism) is installed afterwards in order to obtain an electron bunch with a finite length. A photo-injector is more suitable for short bunch applications. In this kind of system the electron cloud is generated by photo-emission through a short laser pulse on a copper (or other materials) surface, called photocathode. The first

accelerating section of the photo-injector is the RF gun. The electrons are accelerated to a relativistic velocity in the gun. Afterwards the electrons are pushed toward the main LINAC section and they reach the desired energy. The first sections of the accelerating machine can be also used for other purposes other than the acceleration, like the bunching or in general manipulation of the beam. When the final energy is achieved the bunch reaches the *target*. This latter can be a physical one, but also another bunch, like in the collider accelerator, or a undulator in the FEL applications. Along the beam line many devices are installed in order to measure and control the path of the bunches.

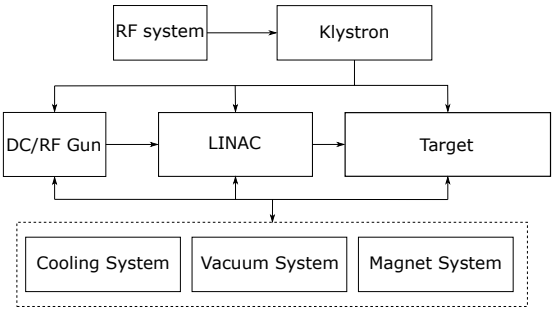

FIGURE 1.1: Simplified block diagram for an electron linear accelerator.

The power for RF gun and accelerating sections is provided by one or more klystrons. This RF source is commonly used because it can be tuned in phase, unlike magnetron, and because of the output power is in the order of the MW, unlike Travelling Wave Tube (TWT) or solid state sources. The RF control system drives the klystron and the power modulator for pulsed operation. Typically, the RF system by implementing some safety controls avoids catastrophic damage of the klystron and/or LINAC.

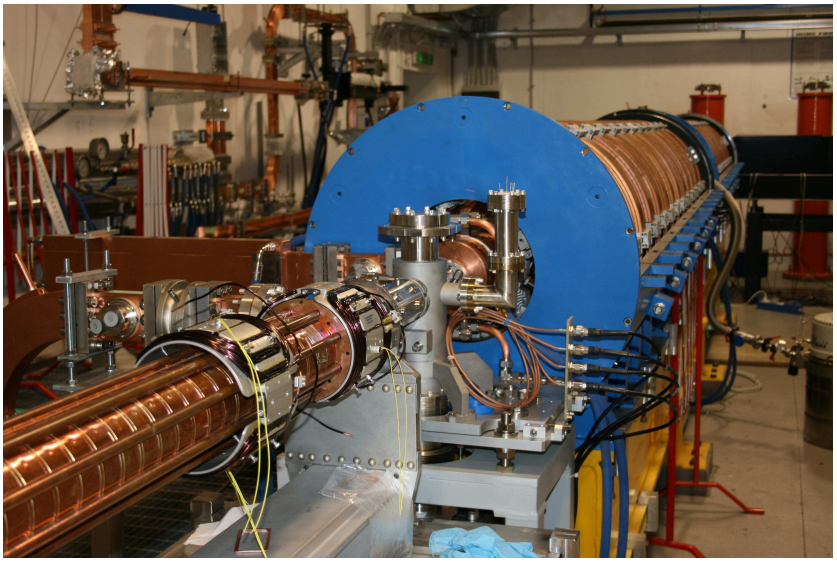

FIGURE 1.2: Electron LINAC of the INFN-SPARC_LAB facility.

At least other three systems are necessary for the proper operation of an accelerator: the cooling system, the vacuum system and the magnet system. The high power employed is in large part dissipated in the conductive walls of the RF cavities. To avoid an overheating of the copper is necessary to remove the heat generated with a proper cooling system. In normal conducting LINAC water is employed, meanwhile in superconducting accelerator liquid helium with a 2 K temperature is commonly used. The beam should propagate in an ultra high vacuum ambient to guarantee an efficient beam transmission. The set of the magnet lens allow to control the beam. For example, the magnet dipole can steer the electron beam, or alternatively, triplets of quadrupole lens can focus the beam. Other employed systems are the control, diagnostic and laser (in the case of RF gun) systems.

1.2 Energy gain in LINAC

In modern LINAC the energy is delivered to the electron bunch by a time varying electric field. Two regimes, distinguished by RF power flow, are possible. The power flows inside the LINAC and the remaining part is dissipated by a load placed at the end of the accelerating section. In this case the section is Travelling Wave (TW) one. Alternatively, the accelerating tube can be terminated with a short circuit and the wave is reflected back until a stationary mode is established. This type of regime is called Standing Wave (SW) operation. The beam and the electric field must be synchronous to obtain a net energy gain. This condition can be obtained by tuning the longitudinal dimension of the single accelerating cavity, as it will be discussed later. The typical geometry of an accelerating cavity is shown in fig. 1.3 for beam passage. The most common geometry is pillbox cavity with two irises at the beginning and end of it. Typically a rounding radius r is specified to avoid sharp edges, where the electric field can be enhanced beyond the safe limit. In the hypothesis of standing wave section and considering only the z component, the time varying electric field on the axis is equal to [1, pp. 33]:

$$E_z(r=0,z,t) = E(0,z)\cos[\omega t(z) + \phi] \tag{1.1}$$

where $t(z)$ is the time of the particle arrival in the z position. The energy gain of a particle with charge q is then:

$$\Delta W = q\int_{-d/2}^{d/2} E(0,z)\cos[\omega t(z) + \phi]dz \tag{1.2}$$

using the trigonometric addition formula (1.2) can be written as:

$$\Delta W = q\int_{-d/2}^{d/2} E(0,z)[\cos(\omega t(z))\cos\phi - \sin(\omega t(z))\sin\phi]dz \tag{1.3}$$

introducing the axial RF voltage:

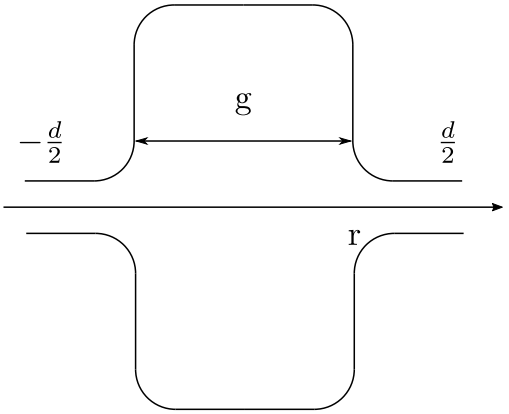

FIGURE 1.3: Cavity geometry and gap.

$$V_0 = \int_{-d/2}^{d/2} E(0,z)dz \tag{1.4}$$

equation (1.2) can be written as:

$$\Delta W = qV_0 T \cos\phi \tag{1.5}$$

where T is called transit time factor and it is defined as:

$$T = \frac{\int_{-d/2}^{d/2} E(0,z)\cos(\omega t(z))dz}{\int_{-d/2}^{d/2} E(0,z)dz} - \tan\phi \frac{\int_{-d/2}^{d/2} E(0,z)\sin(\omega t(z))dz}{\int_{-d/2}^{d/2} E(0,z)dz} \tag{1.6}$$

Typically the electric field on axis $E(0,z)$ is an even function of z and therefore:

$$\int_{-d/2}^{d/2} E(0,z)\sin(\omega t(z))dz = 0; \tag{1.7}$$

and the transit time factor reduces to:

$$T = \frac{\int_{-d/2}^{d/2} E(0,z)\cos(\omega t(z))dz}{\int_{-d/2}^{d/2} E(0,z)dz} \tag{1.8}$$

in the above form it is clear that the transit time factor has the maximum value when the cosine term is equal to one. From equation 1.8 it is clear that the transit time factor is an average of $E(0,z)$ weighted by the cosine function and it is maximized when the gap of the cell is zero [1, pp. 35].

It is possible to explicit the length of the cell in the equation 1.2 with the substitution $V_z = E(0,z)d$:

$$\Delta W = qE(0,z)T\cos\phi\, d \tag{1.9}$$

where the averaged static value of $E(0,z)$ is considered. Some general considerations can be taken from the above equation. The energy gain ΔW is maximized when $\phi = 0$, which is the common choice for the phase in electron LINACs. However, in some case, it is necessary to use a different phase from the optimal one in order to do some arrangement of the electron bunches. For a given cell cavity with length d, the energy gain is proportional to the average electric field $E(0,z)$. The common goal of an accelerator project is to maximize the average field $E(0,z)$ to achieve efficient acceleration. The energy gain is always less in a time varying RF accelerator than in a constant DC type with electric field equal to the one in the centre of the gap due to the transit time factor. Therefore the value of T is a measure of this penalty with respect to the DC case. Anyway, in a RF accelerator, the energy gain is not limited by the fixed potential difference making them more scalable.

For electron LINAC another simplification is possible in most cases. If the velocity increase of the electrons is smaller than the initial velocity in the cell cavity it is possible to approximate the cosine argument as:

$$\omega t(z) \approx \omega\frac{z}{v} = \frac{2\pi z}{\beta\lambda} \tag{1.10}$$

where $\beta = v/c$ and λ is the wavelength. Therefore the transit time factor simplifies to:

$$T = \frac{\displaystyle\int_{-d/2}^{d/2} E(0,z)\cos\left(\frac{2\pi z}{\beta\lambda}\right)dz}{\displaystyle\int_{-d/2}^{d/2} E(0,z)dz} \tag{1.11}$$

A typical design value for transit time factor is $T > 0.64$ [2, pp. 15] and a good value is $T = 0.85$ [3] [4].

1.3 Figure of Merit for LINAC

In the previous paragraph the definition of axial RF voltage and transit time factor have been introduced. However to characterize, at least from the RF point of view, an accelerating cavity more figures of merit are needed. In the table 1.1 a summary of the most useful RF definitions for accelerator design are provided, where d is the length of the cell, ω_{RF} is the angular frequency of the RF signal, S is the transverse section of the

cell, R_s is the surface resistance of the material used for the cell fabrication and S_{ext} is the superficial surface of the cell. These definitions will be used in the next chapters.

TABLE 1.1: RF definitions for accelerator design.

Quantity	Description	Unit
$E_z = E(0,z)$	Complex electric field on axis	(V/m)
$V_z = \left\| \int_0^d E_z e^{j\omega_{RF} z/c} dz \right\|$	Integrated voltage on axis	(V)
$E_a = \frac{V_z}{d}$	Average accelerating gradient	(V/m)
$P_{in} = \frac{1}{2}\int_S \Re(\mathbf{E} \times \mathbf{H}^*) \cdot \hat{z} dS$	Average input power	(W)
$P_{diss} = \frac{1}{2} R_s \int_{S_{ext}} \lvert H_{tan} \rvert^2 dS_{ext}$	Average dissipated power	(W)
$p_{diss} = \frac{P_{diss}}{d}$	Average dissipated power for unit length	(W/m)
$W_e = \frac{\epsilon_0}{4}\int_V \mathbf{E} \cdot \mathbf{E}^* dV$	Electric stored energy	(J)
$W_h = \frac{\mu_0}{4}\int_V \mathbf{H} \cdot \mathbf{H}^* dV$	Magnetic stored energy	(J)
$W = W_e + W_h$	Stored Energy	(J)
$w = \frac{W}{d}$	Stored energy per unit length	(J/m)

With the definitions of table 1.1 it is possible to introduce the main figures of merit for accelerating cavity. The effective shunt impedance per unit length is:

$$r_s = \frac{(E_a T)^2}{p_{diss}} \quad \left(\frac{\Omega}{m}\right) \tag{1.12}$$

From the definition it is clear that r_s should be maximized. Thanks to a high shunt impedance per unit length, the cavity is capable to sustain an high accelerating gradient and the dissipated power is low. This quantity can be considered as the efficiency of the structure against the losses on the cavity walls. At very high level an accelerating cavity can be considered as a resistor with impedance equal to r_s per unit length when connected to a voltage source (klystron). The delivered power into the cavities is quasi-entirely dissipated in the cavity walls when the beam loading effect of the fundamental mode is negligible. Instead, when the input power should be taken into account, the

series impedance can be used:

$$Z = \frac{E_a^2}{P_{in}} \qquad \left(\frac{\Omega}{m^2}\right) \tag{1.13}$$

in this case the impedance is not per unit length but per unit of area.

The quality factor of a resonator can be defined in terms of the dissipated power per unit cycle on walls:

$$Q_0 = \frac{\omega_{RF}\, w}{p_{diss}} \tag{1.14}$$

The ratio of the shunt impedance and of the quality factor is called r/Q (or r *over* Q):

$$\frac{r}{Q} = \frac{(V_z T)^2}{\omega_{RF} w} \qquad (\Omega) \tag{1.15}$$

this quantity measures the efficiency of the cavity per unit stored energy for a given working frequency of the RF source. This quantity is function only of the cavity geometry and it is independent from the surface property of the cavity walls.

1.3.1 Frequency Scaling

The ongoing in accelerator design research is directed towards higher operational frequency. While in the past the most common working frequency for electron LINACS has been the S-BAND (SLAC, DAFNE, KEK), but nowadays most of the future LINAC designs employee higher frequencies, C- or X-band, [5] [6]. Indeed the shunt impedance, i.e. the acceleration efficiency versus the dissipated power, is better at higher frequency and this can be demonstrated within few passages [1]. As it is well known from the literature the surface resistance is proportional to the squared frequency:

$$R_s \propto \sqrt{f} \tag{1.16}$$

and the power dissipated is proportional to the surface resistance and the surface area, which scales with the squared frequency. Therefore the dissipated power scales as $f^{-3/2}$. If the energy gain (and therefore the fields inside the cavity) is retained constant with the frequency the shunt impedance scaling is inversely proportional to dependence of the power dissipated and directly proportional with the dependence of cavity length:

$$r_s = \frac{(E_a T)^2}{p_{diss}} \propto \frac{f^{-1}}{f^{-3/2}} = f^{+1/2} \tag{1.17}$$

thanks to this scaling high frequency LINAC are more power efficient.

[1] This is exactly true only in the case of cavity shape perfectly scaled.

The quality factor scales as:

$$Q_0 = \frac{\omega_{RF}\, w}{p_{diss}} \propto \frac{f^1 \times f^{-3}}{f^{-3/2}} = f^{-1/2} \tag{1.18}$$

and it is clear from 1.17 and 1.18 that r/Q has a linear scaling within the frequency.

1.4 Power Coupling and Steady State Solution

The most common methods for power coupling in RF cavity are the coaxial line, the antenna coupling and the waveguide line [1, pp.140]. However the first and second solution are not used in very high power scenario due to the presence of the inner conductor or of the probe which can be cause of electric breakdown or multipacting [7] [8]. Therefore for multi-MW power levels the waveguide coupling is the best solution, see fig. 1.4.

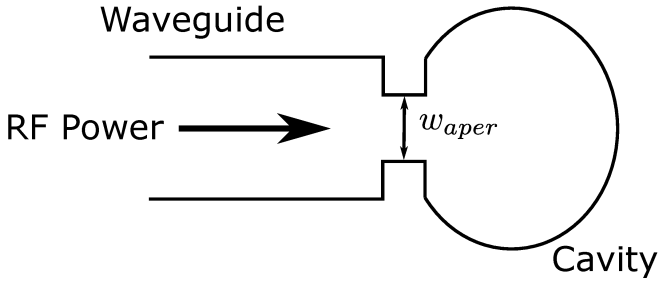

FIGURE 1.4: Power coupling from waveguide to a cavity.

The aperture gap w_{aper} can be tuned with the aid of numerical simulations in order to find the matched condition for the waveguide and the cavity. In the following a SW section and the zero beam loading condition are assumed. Typically in order to protect the RF source from the reflected power a circulator and a matched load is inserted between the waveguide and the source itself.

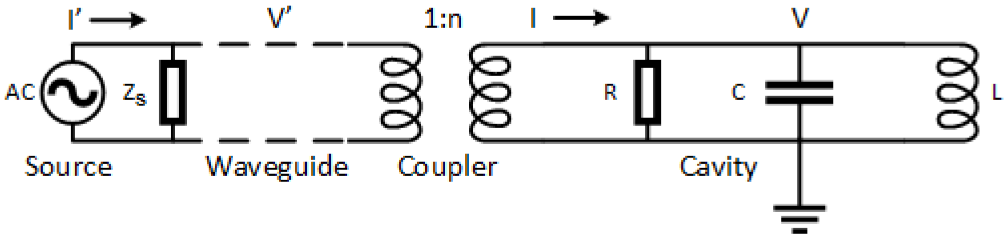

FIGURE 1.5: Equivalent circuit for coupling from waveguide to cavity.

The steady state voltage V can be derived with the aid of an equivalent circuit shown in fig. 1.5, where $R = r_s/2$. The relations between the currents and voltages in

the external load and in the cavity part are:

$$V = nV' \text{ and } I = \frac{I'}{n} \tag{1.19}$$

The dissipated powers in the cavity and in the external load are:

$$P_c = \frac{V^2}{2R} = \frac{n^2 V'^2}{2R} \text{ and } P_{ex} = \frac{V'^2}{2Z_s} \tag{1.20}$$

where Z_s is the impedance of the source. The quality factors of a resonator are for cavity and external load equal to:

$$Q_0 = \frac{\omega_{RF} * w}{P_c} \text{ and } Q_{ex} = \frac{\omega_{RF} * w}{P_{ex}} \tag{1.21}$$

and the total dissipated power is $P = P_c + P_{ex}$. The quality factor of the whole system, Q_L is then equal to:

$$\frac{1}{Q_L} = \frac{1}{Q_0} + \frac{1}{Q_{ex}} \tag{1.22}$$

For coupled cavity it is common to define the ratio of the dissipated power in the external circuit and in the cavity with the β letter[2]:

$$\beta = \frac{P_{ex}}{P_c} = \frac{Q_0}{Q_{ex}} \tag{1.23}$$

When $\beta = 1$ the cavity is defined as critically coupled, for $\beta > 1$ overcoupled and for $\beta < 1$ undercoupled. For critical coupling the quality factors are equal, $Q_0 = Q_{ex}$, and substituting equation 1.23 in 1.22 the relation between the loaded and unloaded quality factor is found:

$$Q_L = \frac{Q_0}{1+\beta} \tag{1.24}$$

From equations 1.20 and 1.23 it is possible to derive the transformer ratio n in function of β:

$$n = \sqrt{\frac{R}{Z_s \beta}} \tag{1.25}$$

The power forwarded to cavity can be derived by considering the equivalent circuit seen from the generator, see fig 1.6.

The current flowing in the matched load Z_s is equal to $I'/2$ and the voltage is therefore $I' Z_s/2$. The forwarded power is then:

$$P_+ = \frac{VI}{2} = \frac{1}{2}\frac{RI}{2\beta}\frac{I}{2} = \frac{I^2 R}{8\beta} = \frac{I^2 r_s}{4\beta} \tag{1.26}$$

[2]The β letter in accelerator science can express the power coupling, but also the ratio between the velocity of the particles. From the context the right meaning should be clear.

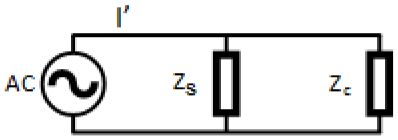

FIGURE 1.6: Equivalent circuit seen from the generator.

Using the equations $I' = nI$ and 1.25, it can be written as:

$$P_+ = \frac{I^2 R}{8\beta} \tag{1.27}$$

For the calculation of the cavity voltage is convenient to use the equivalent circuit seen from the cavity, see fig. 1.7. The current in the resistor of the cavity model can be found

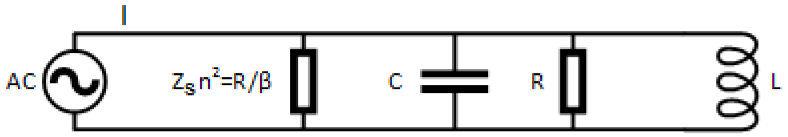

FIGURE 1.7: Equivalent circuit seen from the cavity.

with the current divider rule at the resonant frequency, i.e. capacitor and inductor are open:

$$I_R = \frac{R/\beta}{R/\beta + R} I = \frac{I}{1+\beta} \tag{1.28}$$

and the voltage is:

$$V = \frac{RI}{1+\beta} = \frac{2\sqrt{P_+ r_s \beta}}{1+\beta} \tag{1.29}$$

For $\beta = 1$, the definition of shunt impedance is found. However, for a cavity not critically coupled a correction factor function of β should be taken into account. The reflection coefficient is:

$$\Gamma = \frac{\beta - 1}{\beta + 1} \tag{1.30}$$

and the power delivered to the cavity is equal to:

$$P_- = P_+(1 - \Gamma^2) = P_+ \frac{4\beta}{(1+\beta)^2} \tag{1.31}$$

which has the maximum value for $\beta = 1$.

1.5 Transient Solution

The steady state solution can be extended to include the transient response [1, pp. 146]. The time dependence is an exponential function of the time constant τ:

$$\Gamma(t) = (1 - e^{-t/\tau})\frac{2\beta}{\beta + 1} - 1 \tag{1.32}$$

and the ratio of the reflected wave is then:

$$P_{-}(t)/P_{+} = \left[(1 - e^{-t/\tau})\frac{2\beta}{\beta + 1} - 1\right]^2 \tag{1.33}$$

The above equation is plotted for three values of β in the figure 1.8.

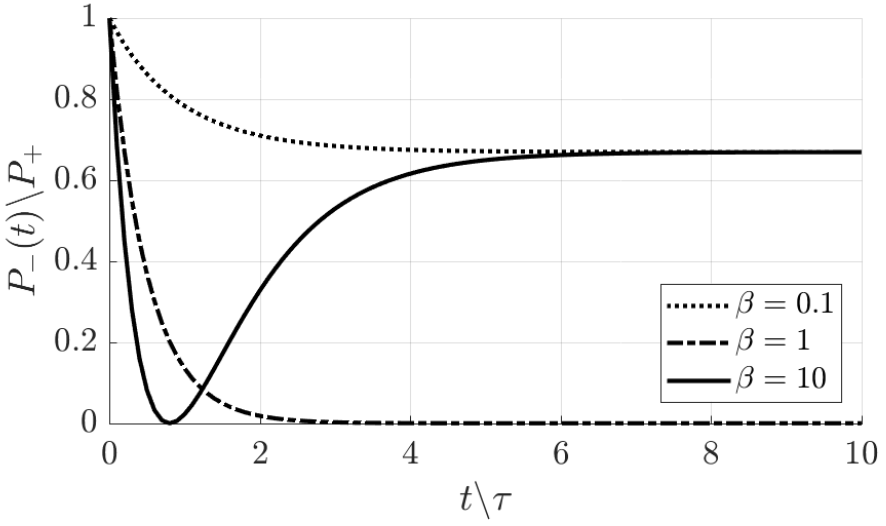

FIGURE 1.8: Ratio of the reflected power and forward power for different value of β.

For the critical coupling case the cavity is filled within three or four times the time constant τ and until the RF power is on no power is reflected back to the source. For the overcoupled case the reflected power is zero during at roughly one τ. This regime can be used when a short filling time is required and the small relative time around the zero point is sufficient to accelerate the bunch, i.e. short bunch applications. The undercoupled case has no practical interest because the power reflected is always greater than zero.

1.6 Periodic Accelerating Structure

The single accelerating cell has been discussed until now. However, common LINAC sections are realized as periodic, or quasi-periodic, array of coupled cells. It is well know that in a waveguide the phase velocity is always greater than c and therefore some wave

slowing method must be employed. A TW section can be pictured as a circular waveguide where the wave is slowed (for both phase and group velocity) by the periodically inserted irises. Periodic structures can be studied by means of the Floquet theorem. It states: *in a given mode of an infinite periodic structure, the fields at two different sections that are separated by one period differ only by a constant factor, which in general is a complex number* [1, pp. 55]. If the constant is real waves cannot propagate and the modes are evanescent. Otherwise if the constant is complex the mode is propagating. For propagating modes the Floquet theorem relates the field in the in the elementary cell and the period:

$$\overrightarrow{E}(r, z + d) = \overrightarrow{E}(r, z)e^{\pm jk_0 d} \tag{1.34}$$

where d is the length of the period and k_0 is the wavenumber. The sign depends on the propagation direction. Because the field inside the section are periodic they can be expanded in a Fourier series:

$$E_z(r, z, t) = \sum_{n=-\infty}^{+\infty} E_n J_0(K_n r)e^{j(\omega t - k_n z)} \tag{1.35}$$

where $k_n = k_0 + 2\pi n/d$ and

$$K_n = \left(\frac{\omega}{c}\right)^2 - k_0^2 \tag{1.36}$$

The solution of equation (1.35) can be interpreted as an infinite number of travelling waves which propagate in both directions inside the structure. They are called space harmonics. The slowing method of the accelerating mode ($n = 0$) by use of irises can be physically explained as the addition of the reflected high order modes to the fundamental one.

Periodic system are typically described by the Brillouin diagram or the $\omega - k$ plot which is a plot of resonant frequency versus wavenumber. Each normal mode is represented by a single point on this plot [1, pp. 58]. With the Brillouin diagram it is possible to identify the frequencies regions where the modes are evanescent, called stopbands, and the frequencies where the modes are propagating, passbands. A slightly modified version of the Brillouin diagram is used in accelerator design. The angular frequency is replaced with resonant frequency and the wavenumber with the phase advance over a single cell length. In the figure 1.9 an example of dispersion diagram with this notation is shown. For coupled oscillators with a finite number of cells, a finite number of modes exists in the accelerating structure. The number of modes and cells is the same. It relates to a cell with a nominal operational frequency of 11.424 GHz and a phase advance of 120 deg. The desired working frequency and phase advance are sufficient in order to found

the length of the single cell, which for efficient acceleration it is equal to [1, pp. 72]:

$$l = \frac{\Delta\phi\lambda_0}{2\pi}\frac{v_0}{c} \tag{1.37}$$

where $\Delta\phi$ is the phase advance per cell, λ_0 the wavelength and v_0 the velocity of the synchronous particle. The dashed line is called the speed of light line, it is equal to:

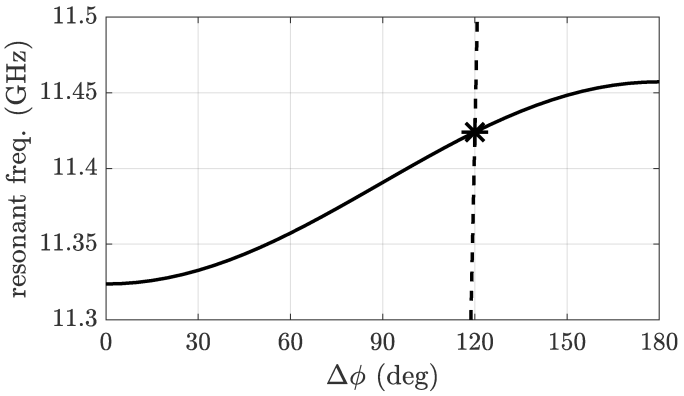

FIGURE 1.9: Dispersion diagram for an accelerating cavity. The passband for this mode is roughly from 11.32 to 11.46 GHz.

$$f_l = \frac{c\Delta\phi}{360l} \tag{1.38}$$

where the phase advance must be expressed in degree [9]. The intersection of the speed of light line with the curve identifies the synchronous mode with particles moving at speed of light. In ultra relativistic regime the speed of particles is usually approximated with c. The dispersion diagram is often obtained by numerical simulations. For a cavity with length l, the resonant frequencies are found by an eigenmode study imposing the same electric field, except for the phase shift $\Delta\phi$, on the two surfaces perpendicular to propagation axis of the wave. Typically these two surface are the cross section of two subsequent irises. The resonant frequencies are found for a finite value of $\Delta\phi$ with a fixed step (5 or 10 degree typically).

From the dispersion diagram it is possible to calculate the group velocity for the synchronous mode by differentiating the $\omega - k$ curve respect to k. For a SW accelerating section the group velocity in the most common 180 degree phase advance is close to zero. For TW sections the group velocity is in the order of magnitude of few percentage of c, generally 0.2-12%.

For lossless (or quasi-lossless) periodic structure the group velocity is equal to [10]:

$$v_g = \frac{P_{in}}{w} \tag{1.39}$$

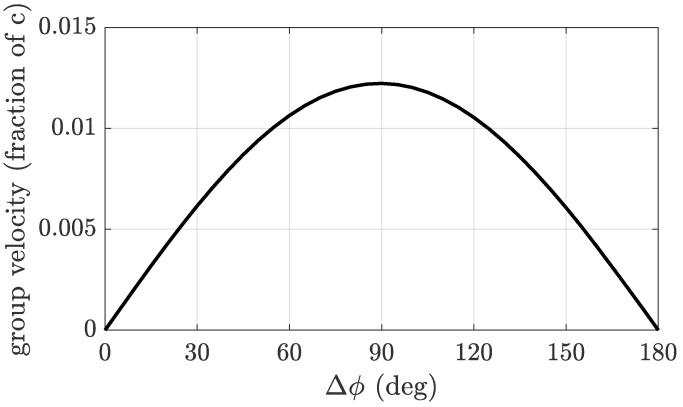

FIGURE 1.10: Group velocity as function of the phase advance.

With this formula it is possible to calculate the group velocity, v_g, as the energy velocity without the use of the dispersion diagram.

1.6.1 Constant Impedance Section

An array of identical coupled oscillators is called constant impedance section. In this kind of section the power attenuation is constant along the propagation axis and the power and the fields are exponentially damped. The shunt impedance per unit length can be in general defined as $r_s = E_a^2/(-dP_{in}/dz)$ where the denominator term is the derivative of the travelling power respect to the propagation axis, i.e. the dissipated power per unit length. Therefore the quality factor is $Q_0 = \omega_{RF} w/(-dP_{in}/dz)$. These two equations lead to:

$$\frac{dP_{in}}{dz} = -\frac{\omega_{RF} P_{in}}{Q_0 v_g} = -2\alpha_0 P_{in} \tag{1.40}$$

where the attenuation constant is defined as $\alpha_0 = \omega_{RF}/2Q_0 v_g$. The solution of this first order differential equation is well known:

$$P(z) = P_0 e^{-2\alpha_0 z} \tag{1.41}$$

The electric field and the travelling power are related by the following equation

$$E_a^2(z) = \frac{\omega_{RF} r_s P_{in}(z)}{Q_0 v_g} \tag{1.42}$$

and therefore $E_a(z) = E_0 e^{-\alpha_0 z}$. The total power attenuation is $\tau_0 = \alpha_0 L$. The energy gain inside the section is function of τ_0 and it is proportional to $(1-e^{-\tau_0})/\sqrt{\tau_0}$ [1, pp. 73]. The maximum occurs for $\tau_0 \cong 1.26$. The attenuation constant and the group velocity are related and therefore the τ_0 value can be controlled by varying the iris radius, i.e. increasing or decreasing the slowing wave effect. Indeed if the attenuation is too high, or

equivalently the group velocity is too low, the power in the last cavities is too small and the acceleration efficiency is low. If the attenuation is too small, i.e. the group velocity is too high, the field flows through the section too quickly for an efficient acceleration and initial accelerating field is too small. In this case most of the power is wasted in the loads.

1.6.2 Constant Gradient Section

It is possible to design a section with an accelerating field constant along the z-axis. This device is called constant gradient section. Introducing in equation 1.40 an attenuation constant function of z it is found:

$$\frac{dP_{in}}{dz} = -2\alpha_0(z)P_{in} \tag{1.43}$$

If the slightly dependence of the shunt impedance with the group velocity is neglected it is found that for a constant electric field dP_{in}/dz must be constant, i.e. $P_{in}(z)$ is linear in z:

$$P_{in}(z) = P_0 + \frac{P_L - P_0}{L}z \tag{1.44}$$

The attenuation constant can be found by differentiating the previous equation and it is equal to:

$$\alpha_0(z) = \frac{1}{2L}\frac{(1 - e^{-2\tau_0})}{1 - z/L(1 - e^{-\tau_0})} \tag{1.45}$$

The energy gain is proportional to $\sqrt{1 - e^{-2\tau_0}}$. For optimal energy efficiency the τ_0 should be infinite. However for $\tau_0 \to \infty$ also the filling time is infinite. Therefore, like for the constant impedance case, a tradeoff must be found. For example for the SLAC LINAC a value of $\tau_0 = 0.57$ was chosen. More details can be found in [11].

1.7 Comparison of Travelling and Standing Wave Operation for LINACs

As reported in the above paragraph in the TW operation the irises loaded structure can be assumed like a circular waveguide where the synchronous wave propagates with phase velocity equal to c and with group velocity (v_g) tipically of few percent of c. One or more load has to be placed at the end of the section in order to dump the travelling wave. In the SW operation no loads are necessary because the field is reflected in the end section of the accelerating section. Instead, even in the case of critical coupling, is necessary to avoid the reflected wave from the section to reach the klystron. This is accomplished with a circulator when it is possible or with an hybrid branch and a load when the circulator is not available [12].

SW and TW sections are equally efficient, i.e. they have the same shunt impedance, if the SW section is built in the 0 or π-mode [13]. However these two modes have one drawback. The group velocity is almost zero and therefore they deliver low energy to the beam and the field profile is very sensitive to the beam current and mechanical tolerances [13].

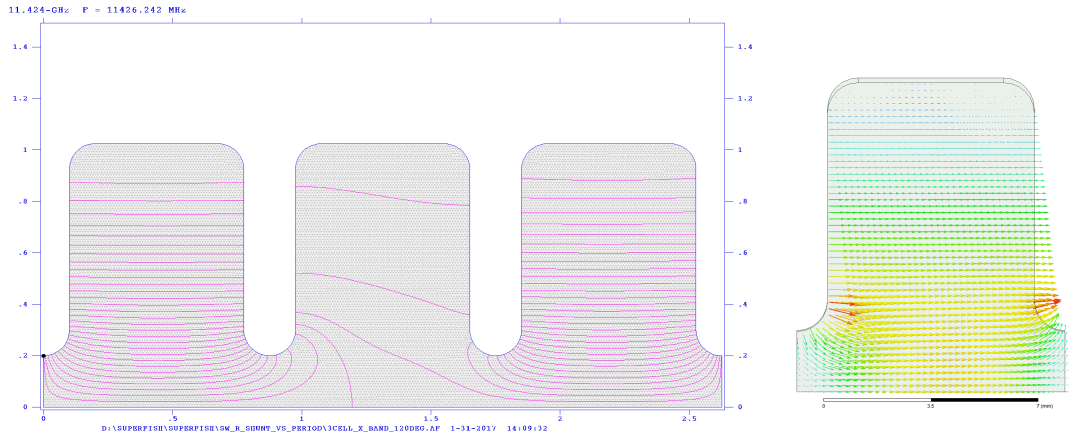

FIGURE 1.11: Electric field simulated with Superfish (left) and HFSS (right) for the evaluation of the shunt impedance in standing and travelling wave regime.

The evaluation of the shunt impedance have been conducted by means of numerical calculations. Superfish and Ansys HFSS codes has been used for evaluation of the shunt impedances in both case (SW and TW), see fig. 1.11. The Superfish code does not directly allow the calculation of the TW section because it is not possible to fix an arbitrary difference phase between two edges of the structure. However the technique described in [14] permits the estimation of the fields also in the TW case. The results are shown in fig. 1.12 and the differences between the two codes are negligible. For the π-mode the shunt impedance for both regime is the same as it has been found in [13].

The choice of a SW or TW section depends on many factors like pulse length, duty cycle, required power, cooling system, the construction tolerance, efficiency, beam loading, operational frequency and the practicality.

In a SW section more than 99% of the power of the source is delivered to the section after five time constant $\tau = 2Q/\omega_{RF}$ [13]. However if the tolerance of the energy gain is strict during the build phase no particle can be injected. For this reason SW sections are more suitable for continuous wave or long pulse operation. For TW section one filling time is sufficient to reach the steady state operation and stable energy gain. Therefore this type of sections are preferred for pulse shorter than the time constant of the structure and this is particularly true for compressed pulse [13].

The SW sections are more sensitive to error fabrication. In relative long section with a high number of cavities, for example 50, the frequency difference from the π-mode and

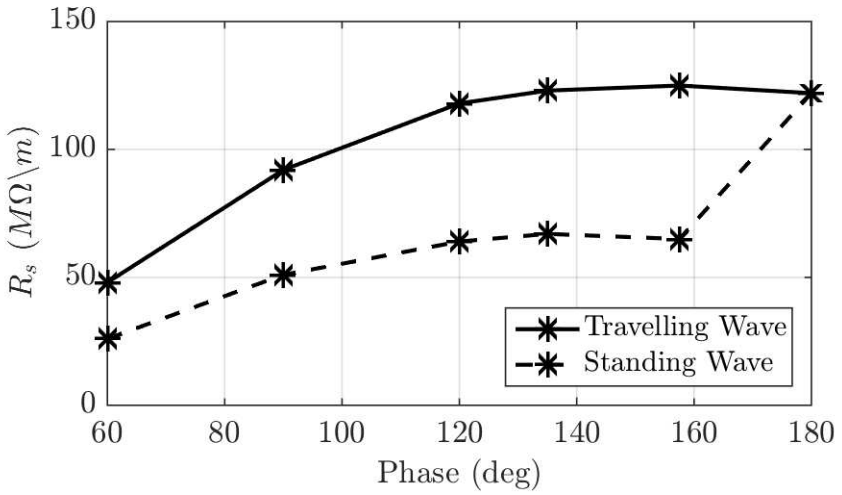

FIGURE 1.12: Comparison of the numerically computed shunt impedance for travelling and standing wave operation.

$49\pi/50$-mode is very small, because the group velocity for the endpoints of the curve is zero. So, even a small error fabrication can modify the standing wave pattern and reduces the overall efficiency of the section.

Lastly for high frequencies (X-band and above) there are not yet developed high power circulator, which are necessary in the standing wave section to protect the klystron from the reflected wave during the transient phase, see par. 1.5.

A special case of SW section is the RF gun. Even tough at least one case of TW RF gun is reported in literature [15] the most common solution for RF gun is the SW section with one (or more) full cell and an half cell. In this case the section is closed by "natural" short circuit, the photo-cathode. Therefore the SW regime is the simpler one.

For both TW and SW regime it is common to speak in term of phase advance per cell as the phase shift between two point of the LINAC section, typically from one iris to the next one. Anyway there is a small difference between the two cases. For TW section a wave is propagating inside the accelerating tube and the phase is increasing (or decreasing) meanwhile the field is propagating. For SW sections the phase advance points out the field configuration: for example for the π-mode an entire wavelength is confined inside two cells, for $\pi/2$-mode inside four cells and so on.

1.8 High Gradient Design and Constraints

The accelerating gradient of a LINAC can be increased when an higher field gradient is sustained by the cavity cell. Unfortunately the maximum sustainable gradient is mostly limited by the electric breakdown phenomena. Even in an ultra vacuum environment, like the cavity tubes, the maximum electric field cannot exceed a certain threshold. It

has been demonstrated that a surface electric field of 285 MV/m can be sustained in a cavity tube [16]. The on axis electric field is in this condition is equal to roughly 150 MV/m. In [17] even a integrated field of 200 MV is reported. However for practical purpose the probability of a breakdown event should be reasonably small. A quantity called breakdown rate probability (BDR) is defined as the number of breakdowns in the unit of time per unit length. For the CLIC linear collider project the BDR is 3×10^{-7} [count/(second*meter)] [18].

In the past the only figure of merit for high gradient design was the Kilpatrick criterion. This empirical law defines the maximum frequency for breakdown free operation given an electric field:

$$f(MHz) = 1.64E^2e^{-8.5/E} \tag{1.46}$$

however this law was found when clean vacuum system was not yet developed and for long pulse length (few μs). Nowadays the Kilpatrick criterion is considered too conservative and recent papers demonstrated that there is not a evident correlation between frequency and breakdown phenomena at least for high frequency [19] [20].

As a result of systematic experimental studies of RF breakdown at X-band and higher frequencies it is possible today a prediction of the high gradient section performance [21]. Some special figures of merit for this purpose have been defined in the recent days. The first is the maximum surface electric field. As stated before there is a correlation between the maximum gradient on axis and the electric field on the surface walls. An high surface electric field can be a trigger for breakdown due to the electrons emission ruled by the Fowler-Nordheim law [22]. The ratio of the fields E_{surf}/E_{axis} in a good high gradient design should be as low as possible. The second figure is derived from the maximum surface magnetic field and it is called pulse heating [23]. The magnetic field is responsible for local heating of the metal surface. This heating is pulsed and follows the RF cycle. The surface is, therefore, degraded and sharp tips can form where the electric field is greatly enhanced [24]. The pulse heating formula is developed from a simple one dimensional model and it takes into account the material properties:

$$\Delta T = \frac{|H_{\parallel}|^2\sqrt{t_p}}{\sigma\delta\sqrt{\pi\rho c_\epsilon k}} \tag{1.47}$$

where t_p is the pulse length, σ the conductivity, δ the skin depth, ρ the density of the material, c_ϵ the specific heat and k the thermal conductivity of the material. The scaled power is another figure of merit defined as:

$$P_s = \frac{P_{in} * t_p^{1/3}}{C} \tag{1.48}$$

where P_{in} is the input power, t_p is the RF pulse length and C is the iris circumference

[16]. The scaled power is typically used for travelling wave structures. A modified version of the Poynting vector is also used for high gradient design:

$$S_c = \Re\{|S|\} + g_c \Im\{|S|\} \tag{1.49}$$

the correction term g_c has been empirically found. More details can be found in [25]. The modified Poynting vector along the group velocity, the operating frequency, the integrated voltage and the r over Q can be assembled in a unique term:

$$\eta \equiv \frac{P_{in}}{E_a^2} \cdot \frac{S_c}{E_a^2} = \frac{v_g}{\omega} \cdot \frac{S_c}{E_a^2} \cdot \left(\frac{r_s}{Q}\right)^{-1} \tag{1.50}$$

for an accelerating section η should be minimized in order to obtain the minimum power requirement for a given accelerating voltage while the probability of breakdown is minimum [26].

Chapter 2

Wakefields and Coupling Impedances

In the previous chapter only the effect of a cavity on a beam is taken into account. In this chapter the *impact* of the beam on the cavity fields is investigated, with the aim to introduce some definitions and concept which will be useful in the rest. Especially for high charge bunch, the effect of the beam on the cavity fields cannot be neglected. The beam itself is equivalent to a source current and not as a simple resistive load. It can absorb energy from the RF field or deliver energy to the cavity. From Maxwell equations it is well known that a moving charge generates an electric and magnetic field. These ones interact with the cavity walls and induce an image charge and a current on the conductive surfaces. When the beam crosses a geometric variation, like for example the irises of the cavity, the self-generated fields are scattered back and they are called wakefields. They can influence the trailing bunches in a multi-bunch LINAC (long range interaction) or the fields generated by bunch head affects its tail (short range interaction). Because the bunch spectrum is broad band many resonant modes of the cavity are excited. Thus, with the wakefield analysis it is possible to study the effect of the bunch on the accelerating mode (beam loading), the High Order Modes (HOM) and in particular the dipole mode which are responsible of the deflecting forces. Due to the broad band nature of the bunch spectrum, HOM can propagate in the pipelines and they can interferer with the normal operation of the LINAC. On the other hand, low frequency modes can be trapped inside the vacuum or diagnostic chambers. The effect of the wakefields on the beam itself may be destructive due to resonant phenomenas. Therefore a careful analysis of the wakefield is required for a LINAC design. Time domain analysis is the natural approach for wakefield simulation. In order to study the coupling of the wakefield with the resonant modes of the accelerating structure it is more convenient to work in the frequency domain with the Fourier transforms of the wakefields which are called coupling impedance.

The chapter is concluded with a brief section on the beam emittance, which is a key parameter of the quality evaluation of the beam propagating in a LINAC.

2.1 Wakefields

The wake functions are defined as the integrals of the normalized forces due to the EM fields excited in a structure by a point charge q and evaluated on a test charge at a distance s behind it [27]. For electron LINACs the velocity of the particles can be almost always approximated with $v \cong c$. As consequences of this the wake fields cannot propagate ahead of the bunch. The Lorentz force acting on the test charge with charge q is :

$$\overrightarrow{F}(\overrightarrow{r_b}, \overrightarrow{r_E}, s) = q(\overrightarrow{E} + \overrightarrow{v} \times \overrightarrow{B}) \tag{2.1}$$

where $\overrightarrow{r_b}$ is the position of the bunch, $\overrightarrow{r_E}$ of the test charge and s the distance between them. Both longitudinal and perpendicular cases of the wake function are defined below. The wake functions are also the Green function of a particular structure because a point charge distribution can be assumed like the δ Dirac generalized function. The wake potential have the same definition but for a finite distribution of the bunch. To distinguish them the wake functions are indicated with $G(s)$ and the wake potentials with $W(s)$. The mathematical definition for the longitudinal case is [27]:

$$G_{\parallel}(\overrightarrow{r_b}, \overrightarrow{r_E}, s) = -\frac{1}{q}\int_{-\infty}^{+\infty} E_z(\overrightarrow{r_b}, \overrightarrow{r_E}, z, t = \frac{z+s}{c})dz \tag{2.2}$$

and for the transverse:

$$G_{\perp}(\overrightarrow{r_b}, \overrightarrow{r_E}, s) = -\frac{1}{q}\int_{-\infty}^{+\infty} (\overrightarrow{E} + \overrightarrow{v} \times \overrightarrow{B})dz \tag{2.3}$$

where the arguments of the fields are omitted for sake of brevity. For both bunch and test particle a propagation parallel to the axis of the structure is assumed. The wake functions $G_{\parallel}(s)$ and $G_{\perp}(s)$ have units of V/C, but often the V/pC unit is used.

For a point charge all modes are necessary to describe the spectrum of the bunch excitation. So, $G_{\parallel}(s)$ can expanded as:

$$G_{\parallel}(r_b, \theta_b, r_e, \theta_e, s) = \sum_{m=0}^{\infty} \varepsilon_m r_b^m r_e^m \cos(m(\theta_b - \theta_e)) G_{\parallel}^{(m)}(s) \tag{2.4}$$

where is $\varepsilon_m = 1$ for $m = 0$ otherwise $\varepsilon_m = 2$. In the above equation axis-symmetric structure is assumed and therefore the position vector $\overrightarrow{r}$ is replaced with the polar coordinate. The index m identifies all the modes with an azimuthal variation, for example

for $m = 0$ the monopole mode, for $m = 1$ the dipole and so on. For wake function near the axis the first mode gives dominant contribution to the sum due to the terms r_b^m.

For the transverse case, near the axis of the structure, a equation similar to 2.4 exists:

$$G_\perp(r_b, \theta_b, r_e, \theta_e, s) = \sum_{m=1}^{\infty} r_b^{m-1} r_e^m [\widehat{r}\cos(m\theta_b) - \widehat{\theta}\sin(m\theta_e)] G_\perp^{(m)}(s) \tag{2.5}$$

also for the transverse case the first mode is the dominant. To remove the dependence on the transverse displacement a wakefield per unit of displacement is defined by dividing the equation (2.3) respect to the offset of the test charge. In this case the dimension unit is V/pC/mm. The approximation with only the dipole terms is quoted with an apex mark, $G'_\perp$

For a bunch with a finite distribution the wake potentials have a definition similar to the equations 2.2 and 2.3 in terms of the Green function [27]:

$$W_\parallel(\tau) = \int_0^\tau G_\parallel \lambda(\tau - t) dt \tag{2.6}$$

and

$$W_\perp(\tau) = \frac{1}{\bar{\xi}} \int_0^\tau G'_\perp \xi(\tau - t)\lambda(\tau - t) dt \tag{2.7}$$

where a displacement ξ function of the time coordinate t is assumed and $\bar{\xi}$ is the average.

2.2 Coupling Impedance

The concept of impedance relates the voltage with the current in a resistor. More generally, the impedance of a microwave device is a function of the frequency. In a particle accelerator the current is flowing through a vacuum pipe, therefore it does not experience a direct resistance. While the particles advance inside the LINAC, a voltage is induced in the cavity. The coupling impedances relates this voltage with the beam current. Also for the impedance, longitudinal and transverse cases are identified. The definition of the first case is [27, pp. 74]:

$$Z_\parallel(\overrightarrow{r_b}, \omega) = -\frac{1}{\widetilde{I}} \int_{-\infty}^{+\infty} \widetilde{E}(\overrightarrow{r_b}, z) e^{j\omega z} dz \tag{2.8}$$

comparing with the definition of the wake functions it is clear that the coupling impedance and wake functions are related by a Fourier transforms:

$$Z_\parallel(\omega) = \int_{-\infty}^{+\infty} G_\parallel(\tau) e^{-j\omega\tau} d\tau \tag{2.9}$$

For the dipole transverse case a similar definition is provided [27, pp. 76]:

$$Z_{\perp}(\overrightarrow{r_b}) = \frac{j}{qr_b}\int_{-\infty}^{\infty}[\overrightarrow{\tilde{E}}(\overrightarrow{r_b},z) + \overrightarrow{v}\times\overrightarrow{\tilde{B}}(\overrightarrow{r_b},z)]_{\perp}e^{j\omega z/v}dz \tag{2.10}$$

which it is equal to the Fourier transform multiplied by the imaginary unit:

$$Z_{\perp}(\omega) = \int_{-\infty}^{+\infty} G_{\perp}(\tau)e^{-j\omega\tau}d\tau \tag{2.11}$$

Historically the imaginary unit was introduced to uniform the contribution of the longitudinal and transverse impedance of the beam stability [28]. The unit of dipole transverse impedance is Ω/m, which is an impedance for unit of displacement.

The magnitude of the impedance of the pillbox in fig. 2.2 is shown in the following plot. The marker indicates the fundamental TM_{010} mode.

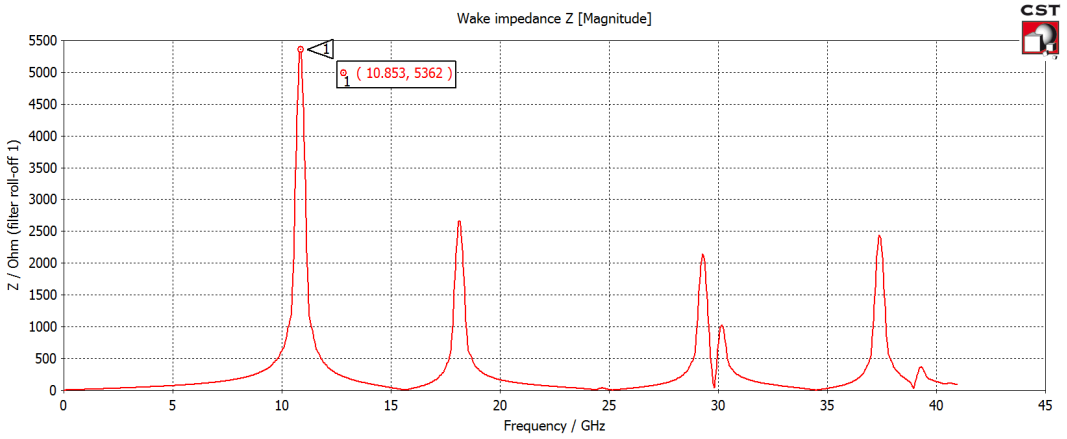

FIGURE 2.1: Coupling impedance for the pillbox cavity of fig. 2.2.

2.3 Loss and Kick Factor

To easily calculate the lost energy of bunch propagating inside a pipe the longitudinal loss factor is introduced. The energy change is the product of the bunch charge and of the induced voltage which it is equal to:

$$V(\omega) = -Z_{\parallel}(\omega)I_b(\omega) \tag{2.12}$$

and the current is also proportional to the charge q. Therefore the energy drop is:

$$\Delta E = -k_{\parallel}q^2 \tag{2.13}$$

The proportionality number $k_{\parallel}$ is called loss factor and it is expressed in V/pC unit. Under normal circumstances the bunch looses energy and therefore $k_{\parallel}$ is a positive number. The loss factor depends on the geometry of the structure but also on the bunch distribution and in particularly for the common gaussian distribution on the rms length σ:

$$k_{\parallel}(\sigma) = \frac{1}{2\pi}\int_{-\infty}^{+\infty} Z_{\parallel}(\omega)h(\omega,\sigma)d\omega \tag{2.14}$$

where $h(\omega,\sigma)$ is the power density of the bunch. In the time domain the loss factor is equal to:

$$k_{\parallel}(\sigma) = \int_{0}^{\infty} G_{\parallel}(t)S(t)dt \tag{2.15}$$

where

$$S(t) = \int_{0}^{+\infty} \lambda(\tau)\lambda(\tau - t)d\tau \tag{2.16}$$

is the autocorrelation of the bunch density.

For the transverse case, the loss factor is called kick factor. Indeed, the dipole dominant mode exerts a deflection of bunch from the axis. The definition is similar to the longitudinal case:

$$k_{\perp}(\sigma) = \frac{1}{2\pi}\int_{-\infty}^{+\infty} Z_{\perp}(\omega)h(\omega,\sigma)d\omega = \int_{0}^{\infty} G_{\perp}(t)S(t)dt \tag{2.17}$$

however, as the all other transverse quantities, the kick factor is defined for unit of displacement and therefore usually measured in V/pC/mm.

2.3.1 Numerical Calculation of Wakefields

Because of the complex geometry of an accelerating cavity the analytical solution of the wakefield problem is possible only for few cases. For the simple case of the pillbox cavity (without smoothed edges) and in the approximation of infinite radius (parallel plates) the wakefield solution for the longitudinal wake function is the derivative of:

$$W_s(s) = \frac{2Z_0}{\pi}\ln(1 + \frac{1}{s/g + [s/g]}) \tag{2.18}$$

where g is the length of the cavity and the square bracket means that the integer values of the argument should be taken [27].

In most cases, the wakefield solution can be find only by numerical methods. Time domain codes, like CST Particle Studio or ABCI, can compute the scattered field of a structure when a pencil beam, i.e. a beam with transverse dimensions zero, is propagating along a straight line, see fig. 2.2.

The wake functions, however, can be only calculated by analytical approach due to the point-like beam source. Therefore, only wake potentials for finite length bunch can

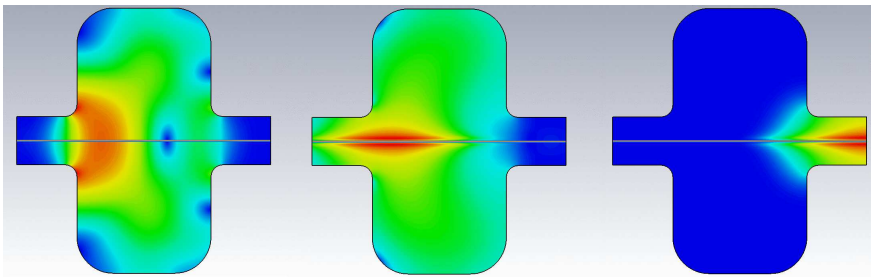

FIGURE 2.2: Simulated wakefields inside a pillbox cavity. The bunch is propagating from right to left and the electric field for three time steps is recorded.

be computed. For the most common case of bunch with gaussian distribution, ten mesh points within the standard deviation (σ_z) of the bunch should be used.

2.4 Head-Tail Instabilities

A bunch propagating inside an accelerating structure can be affected by head tail instabilities due to the short range transverse wakefields if the bunch propagates off axis [29]. Under this condition a growing oscillation of the tail bunch is possible. For an analytical estimation of this instabilities the bunch is modelled as two macro-particles each with $Q_t/2$ charge and separated by distance $\Delta z = 2\sigma_z$

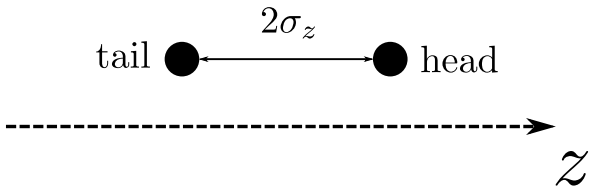

FIGURE 2.3: Two macro-particles model for head tail instabilities calculation.

For a bunch without acceleration the equations of motion are [30]:

$$\ddot{x}_1 + k_1^2 x_1 = 0 \tag{2.19}$$

$$\ddot{x}_2 + k_1^2 x_2 = \frac{Q_t e}{2E} W_\perp(2\sigma_z) x_1 \tag{2.20}$$

where k_1 and k_2 are the betatron wave numbers for head and tail macro-particles, E is the energy and $W_\perp(2\sigma_z)$ is the transverse wakefield generated from the head macro-particle and experienced by the tail macro-particle, the wakefield experienced by the

head macro-particles is zero for the causality principle. In the smooth approximation the transverse motion of the head, i.e. betatron oscillation, can be approximated with an harmonic function:

$$x_1 = x_0 \cos(k_1 z) \tag{2.21}$$

If we assume that head and tail macro-particles have the same betatron wave number $k_1 = k_2 = k$ the motion of the tail macro-particles is that of harmonic oscillator on resonance [1, pp. 385] and the displacement of the tail macro-particle respect of the head macro-particle is equal to [30, pp. 467]:

$$\Delta x = x_2 - x_1 = \frac{Q_t e}{2E} W_\perp(2\sigma_z) x_0 z \sin(kz) \tag{2.22}$$

In order to take in account the acceleration along the line it is possible to derive the previous equation respect to z obtaining:

$$\frac{d}{dz}\left|\frac{\Delta x}{x_1}\right| = \frac{Q_t e}{2E(z)} W_\perp(2\sigma_z) \tag{2.23}$$

with the energy $E(z)$ now function of the longitudinal coordinate z. The displacement of the leading particle can be evaluated integrating along z the previous equation:

$$\left|\frac{\Delta x}{x_1}\right| = \frac{Q_t e}{2E_0} W_\perp(2\sigma_z) \int_0^{z_f} \frac{\beta(z)}{\gamma(z)} dz \tag{2.24}$$

where z_f is the length of the LINAC, E_0 the rest energy of the particle and β is the average function of the betatron oscillation. With uniform acceleration $E(z) = E_0 + Gz$ (with G expressed in eV/m) the integral of the above equation is:

$$\int_0^{z_f} \frac{\beta(z)}{\gamma(z)} dz = \beta \frac{E_0}{G} \ln \frac{\gamma(z_f)}{\gamma_0} \tag{2.25}$$

It is possible to replace the smooth approximation with a more realistic focusing-defocusing (FODO) lattice with the associated betatron function, β_m, instead of using $\beta = \frac{1}{k}$. The amplitude of the relative displacement is therefore equal to:

$$\left|\frac{\Delta x}{x_1}\right| = \frac{Q_t e}{2G} W_\perp(2\sigma_z) \beta_m \ln \frac{\gamma(z_f)}{\gamma_0} \tag{2.26}$$

with whom it is possible to calculate the relative displacement known the wakefield function[1].

[1] The wakefield itself has a weak dependence because the transverse position of the bunch change during the propagation. This second order effect has been neglected.

2.5 Beam Quality and Emittance

In this paragraph a short, non rigorous, introduction of the emittance concept is provided for the reader and with the aim to recall some notation. The definition of emittance has been introduced in order to compare a real bunch with an ideal one which propagates inside the linac with a laminar regime. In this regime the particle of the bunch propagates in the highest order possible mode with the same velocity and each particle has a constant distance, in the transverse and longitudinal frame, during the propagation with any other particle. This beam is an idealization and it is not possible to obtain. For this reason the definition of emittance has been introduced as a quantifier of the beam quality.

Each particles of a bunch can be identified by six parameters: three for the position and three for the momentum. Therefore, each particle is a point in a six dimensional phase space or more suitably for work in three points in three two dimensional phase space, one for each axis. For the transverse case the normalized emittance is generally employed:

$$\varepsilon_n = \Delta x \Delta x' \beta\gamma \tag{2.27}$$

where Δx is the relative displacement of the position and $\Delta x'$ is the variation of the velocity, β the speed of the particles compared to c and γ the Lorentz factor. The emittance is typically measured in mm-mrad units or μm. For example, an emittance of 1 mm-mrad means that the average angular spread of the particles is 1 mrad after 1 mm of propagation. The emittance can be also defined without the $\beta\gamma$ factor, but in this case has a dependence on the acceleration. This is because, the transverse momentum during acceleration is unchanged while the longitudinal momentum increases. For this reason these two factors are taken into account.

For the longitudinal case the normalized emittance is defined as:

$$\varepsilon_{nl} = \frac{\Delta z \Delta p}{mc} \tag{2.28}$$

however, it is also often expressed as the percentage average difference of the particles for the bunch. In this more intuitive definition it is called energy spread and for example for a value of 1% it means that the average energy difference between the particles is the 1% of the nominal energy. A rigorous treatment of the emittance can be found in [31].

Chapter 3

Parallel Coupling Structure

The physical phenomena that limits the increase of the accelerating gradient is the RF breakdown. For high power operation the breakdown rate (BDR) probability can increase beyond the design constraint. During a breakdown event the normal operation of the accelerating structures is compromised by the reflected RF power from the cell where the arc has occurred up to the klystron. The surface damage is more probably located on high fields region, like irises. A breakdown event can alter the geometry of the irises. Cell to cell coupling coefficient, in standard serial iris coupled structure, is proportional to the third power of the iris radius, so even small change in iris aperture can affect the coupling coefficient between cell, leading to a detuning of the structure. Moreover in on axis coupling configuration leftovers of the arcs explosion have to be pumped out through many cells with a small aperture.

These problems can be solved with an innovative design called parallel-coupled accelerating structure (PCAS), which will be discussed in this chapter. In this new kind of accelerating structure every cell is coupled through a large aperture to a waveguide located parallel to the accelerating cells and the iris between two cells is very small but sufficiently large to bunch propagation, see fig. 3.1. The expected shunt impedance is higher because it can be optimized without affecting the power coupling. The breakdown event is confined in a single cavity and only a small fraction of the stored energy inner to the structure is compromised consequently, reducing the potential surface damage.

Properly designed structure with a single mode is in the pass-band. Thanks to this property PCAS design is relative easy to tune because each cell can be considered as a single resonator not coupled with the neighbours. The tuning can be performed with help of tuners which deform the cavity itself.

The gas generated by breakdowns can be easily pumped out through the large aperture of the parallel coupling hole between waveguide and cell. The feeding waveguides can be also exploited for high order mode (HOM) damping in multi-bunch operation.

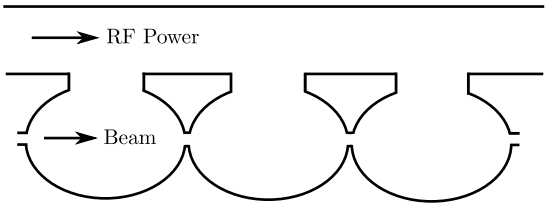

FIGURE 3.1: In PCAS the bunch propagation is placed on the axis, while the RF power propagates in parallel waveguide and it is coupled with a large hole for each cell.

3.1 PCAS literature

The idea of a parallel coupled structure has been proposed in 1965 by Schaffer in [32] for the DESY facility. The π-mode is employed for this design and a waveguide is used for feeding the accelerating cavity of the storage ring. A LINAC design was instead published by Sundelin in [33]. Both designs were proposed for an electron storage ring and in the L-band with a frequency of 500 MHz. The latter one employs a coaxial line for the feeding line which is not suitable to high gradient design. The spacing between cells is an half-wavelength. A more recent work [34] focuses on the possibility to exploit various parallel feeding scheme with one, two, three or four waveguides in order to design a LINAC which can deliver an high average current (0.1 A). For this design the relative position between the cells is free and it can be used for installation of focusing magnets. The design of a standing wave section with a parallel coupling scheme is reported in [35]. In this work the power is divided by means of a distributed directional coupler which provides equal fields in the cavity cell. A circulator is not needed because the power reflected from each cell is absorbed in a RF load and the proper combination of them can neglect the power reflected to the source. Finally, a travelling wave section has been studied in [36]. A parallel TW section can be used in compact accelerator due to the possibility of higher shunt impedance, not limited by the iris aperture. At the same time to the large S_{11} impedance bandwidth that can be achieved it is possible to avoid the use of the circulator and the cell tuning is an easy procedure.

3.2 Physics of the Parallel Coupled Cavity

For a periodic structure with period d along the z axis the electromagnetic fields must satisfy the following expression:

$$\psi(x, y, z + nd) = \psi(x, y, z)e^{-\gamma nd} \quad (n = \pm 1, 2, \cdots) \tag{3.1}$$

where γ is the complex propagation constant. EM fields with this property are called Floquet modes. The fields inside a periodic structure can be represented as linear combination of Floquet modes [37]. This general approach can be used also for the parallel coupled structure.

The single cell can be represented as a two ports device where V_1, V_2, I_1 and I_2 are the modal voltages and currents, see fig. 3.2.

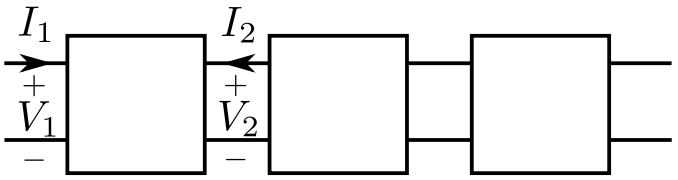

FIGURE 3.2: Periodic structure as a chain of two ports device.

For simplicity only the fundamental mode is present at the ports and the losses are supposed negligible. Because of the periodicity, the same mode is present at the input and output port. It is possible to relate the input/output voltage and current through the following transmission matrix:

$$\begin{bmatrix} V_2 \\ -I_2 \end{bmatrix} = \begin{bmatrix} a_{11} & a_{12} \\ a_{21} & a_{22} \end{bmatrix} \begin{bmatrix} V_1 \\ I_1 \end{bmatrix} \tag{3.2}$$

because the equation (3.1) is also valid for the voltage and current it is feasible to write:

$$\begin{bmatrix} V_2 \\ -I_2 \end{bmatrix} = e^{\gamma d} \begin{bmatrix} V_1 \\ I_1 \end{bmatrix} \tag{3.3}$$

and combining equations (3.2) and (3.3):

$$\begin{bmatrix} a_{11} & a_{12} \\ a_{21} & a_{22} \end{bmatrix} \begin{bmatrix} V_1 \\ I_1 \end{bmatrix} = e^{\gamma d} \begin{bmatrix} V_1 \\ I_1 \end{bmatrix} \tag{3.4}$$

from the above equation it is clear that the exponential term, $e^{\gamma d}$, is an eigenvalue for the transmission matrix. Therefore the following equation is obtained:

$$e^{2\gamma d} - (a_{11} + a_{22})e^{\gamma d} + Det[a] = 0; \tag{3.5}$$

where the determinant is unitary due the reciprocity property. Multiplying for $e^{-\gamma d}$ it is possible to relate the γd term with a_{11} and a_{22} quantities:

$$\cosh(\gamma d) = \frac{a_{11} + a_{22}}{2} \tag{3.6}$$

When $|(a_{11} + a_{22})/2| < 1$ the Floquet mode is propagating without attenuation:

$$\gamma d = \pm j \arccos\left(\frac{a_{11} + a_{22}}{2}\right) \tag{3.7}$$

For $|(a_{11} + a_{22})/2| \geq 1$ the term γd is real and the mode is evanescent. The bandwidth where the propagation is allowed depends on the geometry of the single cell. The minimum and maximum phase shift is found for:

$$\frac{a_{11} + a_{22}}{2} = \pm 1 \tag{3.8}$$

which correspond to a phase shift of $\delta = \pm\pi$.

The ratio between the voltage and the current is the characteristic impedance of the Floquet mode and it is the same value for each cell due to the structure periodicity:

$$Z_c = \frac{V_1}{I_1} = \frac{V_2}{-I_2} \tag{3.9}$$

The impedance is a function of the periodicity and of the voltage transmission matrix [37]:

$$Z_c = \frac{1}{a_{21}}\left[\frac{a_{11} - a_{22}}{2} + \sinh(\gamma d)\right] \tag{3.10}$$

The propagation of a Floquet mode is not perturbed if the periodic structure is matched to the load and the generator. Therefore it is possible to match an accelerating section to the klystron source with custom input and output coupling cells [38].

3.2.1 Parallel Coupled Single Cell and Phase Velocity Control

A parallel coupled travelling wave single cell is shown in fig. 3.3. This simple structure will be used in the next to show the properties of PCAS and how to control the main RF parameters (resonant frequency, phase and group velocity) by appropriate variation of its geometry.

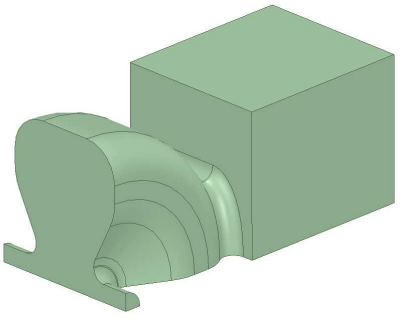

FIGURE 3.3: Periodic cell of a TW parallel coupled accelerating section.

The resonant frequency of the synchronous mode is graphically found from the intersection of the speed of light line and the accelerating dispersion curve, see par. 1.6. This intersection is sometimes called working point of the structure. It is possible to tune the resonant frequency to the desired value by changing the whole dimension of the cavity. This is true for this PCAS and in general for all cavity-type accelerating section and typically the radius of the cell is varied.

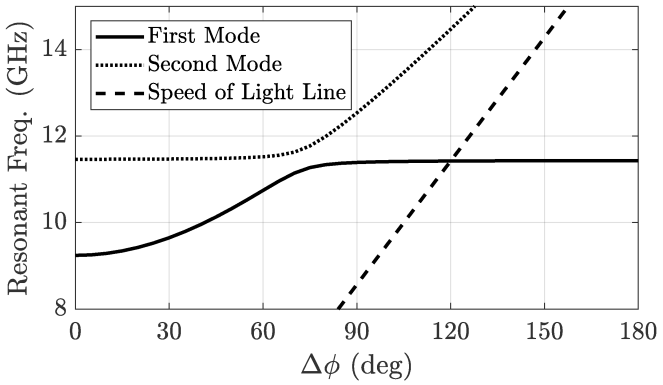

FIGURE 3.4: Dispersion diagram for the structure of fig. 3.3.

Thus the phase condition matching between the particles and the RF pulse is fulfilled when the abscissa of working point is the desired phase advance per cell and the ordinate is the frequency of the RF source. The length of the cell in order to satisfy this condition is found with equation (1.37) and the resonant frequency is tuned by changing the radius of the cell. Usually, for the frequency tuning, Finite Element Method (FEM) simulations are required. For the structure of fig. 3.3 the phase advance is set to 120 deg and the frequency to 11.424 GHz.

3.2.2 Mode Separation

The working point found in fig. 3.4 is located in an almost flat region of the accelerating mode curve. Due to the finite rise time of the RF pulse the bandwidth of the pulse is usually in the order of magnitude of tens of MHz. By considering a rise time of 50 ns the bandwidth of pulse is approximately found with the following equation [39, pp. 14]:

$$BW \simeq \frac{0.35}{TR} = 7 \ \text{[MHz]} \tag{3.11}$$

where BW is the bandwidth and TR is the rise time. Thus, at least a separation of 7 MHz is needed between the desired mode and the two adjacent ones. In order to avoid the excitation of the neighbour modes it is desirable to locate the working point in a section of the curve with a sufficient slope. It is possible to move the knee of the curve, i.e. the phase advance $\Delta\phi$ which is related to the phase velocity in the waveguide,

by tuning of the waveguide broadwall dimension. An analytical expression between the waveguide dimension and the phase velocity is given in the next paragraph.

The dispersion diagram obtained when the broadwall waveguide dimension is increased from 16 mm (see fig. 3.3) to 21 mm is shown in fig. 3.5. A zoom around the

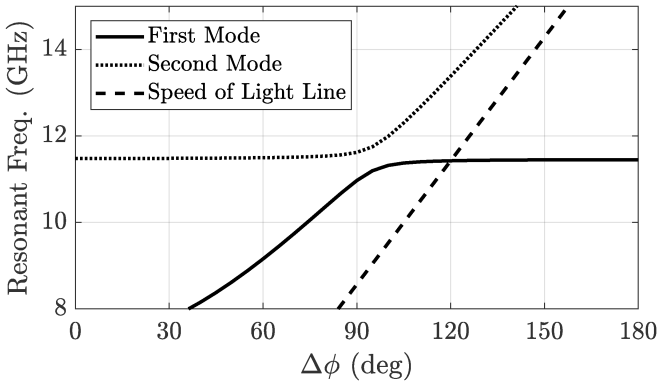

FIGURE 3.5: Dispersion diagram for the structure of fig. 3.3. The broadwall waveguide has been increased in order the mode separation.

working point is plotted in fig. 3.6. Considering an accelerating section of 36 cells, for a total length of roughly 30 cm, the previous and the next modes have a phase advance of 115 and 125 deg. The required bandwidth of ±7 MHz around the operation frequency is shown with two red lines and the modes with circle markers.

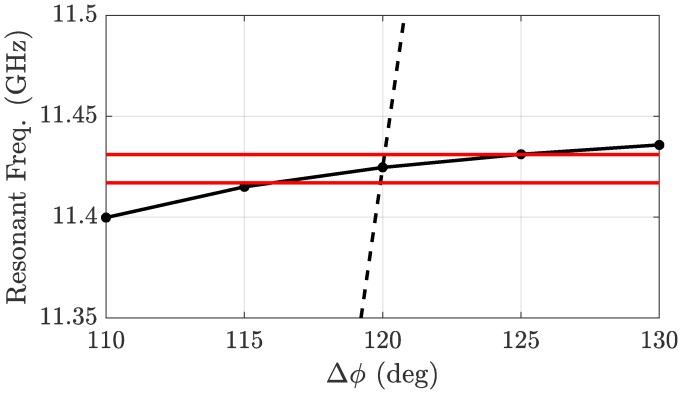

FIGURE 3.6: Working point zoom of the dispersion diagram in fig. 3.5. The red lines show the ±7 MHz bandwidth.

3.2.3 Relation between the Broad-Wall Waveguide Dimension and the Phase Velocity

If only forward waves are considered the simple structure shown in fig. 3.1 cannot directly implemented as it is. The phase advance cannot be compatible with speed of

light particles since the phase velocity in a waveguide is under normal condition (i.e. when Floquet modes are not present) always greater than c, so it is impossible match the phase of the RF power with the beam. It is possible to reduce the phase velocity with insertion of tuning pins like in [40] but in this case the waveguide feeder is treated like a iris loaded cavities transferring the disadvantages of this structure from cavities to the waveguide. A dielectric material can be added in order to slow the wave but the waveguide should be empty in order to efficiently pump out and in any case this solution can be used only for low power system because the losses in the dielectric material can be too high for multi-MW system.

A simple idea to match the RF phase in the waveguide with the velocity of the electrons every n cells is here developed. A phase matching system is presented for the π-mode line. In this approach the waveguide and the cell are considered as two different parts and not as a single periodic structure where a Floquet mode is present. Aim of this paragraph is to find a way to control the phase advance by varying the waveguide broadwall dimension and consequently the phase velocity.

Here we consider ultra-relativistic beam, with a phase advance in cavity equals to $\phi_c = \pi$ the synchronous condition for cavity length is $l = \frac{\lambda_0}{2}$ [1, eq. (3.51)]. Unfortunately, the phase velocity in a uniform waveguide is always greater than the speed of light so a proper phase matching between the waveguide and cells has to be found.

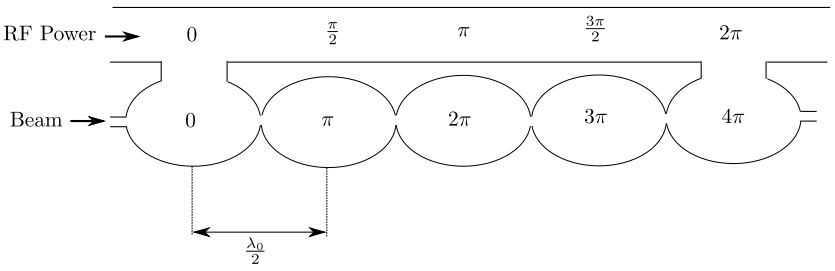

FIGURE 3.7: In the phase matching interpolation scheme for $\pi-$mode a coupling hole is placed every four cells. The minimum ratio between phase advance in waveguide and phase advance in cells is 0.5 for proper matching.

It is possible to define a ratio factor of the phase advance in the feeding waveguide, $\phi_w(z)$, divided by the desired phase advance on the axis of the accelerating structure at the mid point of the cavity, $\phi_c(z)$:

$$r = \frac{\phi_w(z)}{\phi_c(z)} \tag{3.12}$$

since both phase advances depend linearly with z the ratio does not. This ratio r must satisfy two condition: r^{-1} must be an integer number greater than one for the phase matching condition between waveguide and cavity (taking into account a phase advance in the waveguide lower than the phase advance in cavities) and r can be equal only to

a single value, see fig. 3.7. These statements can be demonstrated with few equations. The phase in cavity is equal to:

$$\phi_c(z,t) = \beta_z z - \omega t = \omega\left(\frac{\beta_z}{\omega}z - t\right) = \omega\left(\frac{z}{v_{ph}} - t\right) \tag{3.13}$$

where β_z is the phase constant along the z-axis. Because $v_{ph} = \frac{\omega}{\beta_z}$, for simplicity we can set $t = 0$ in order to find only the spatial variation of the phase:

$$\phi_c(z) = \omega\frac{z}{v_{ph}} = 2\pi f\frac{z}{v_{ph}} = \frac{2\pi c \cdot z}{\lambda \cdot v_{ph}} \tag{3.14}$$

from above equation it is clear that the phase advance ϕ_c is inversely proportional to the phase velocity v_{ph}. For synchronous matching condition the phase in the cavity ϕ_c has to be:

$$\phi_c = 0, \pi, 2\pi, \cdots = n\pi \tag{3.15}$$

from equation 3.12 it is possible to write the phase advance in the waveguide as:

$$\phi_w = r\phi_c \tag{3.16}$$

for the phase matching between waveguide and cell the difference should be equal to[1]:

$$n\phi_c - n\phi_w = 2\pi \tag{3.17}$$

where n is a arbitrary number of cells. Within few simple passages it is found:

$$n\pi - rn\pi = 2\pi \Leftrightarrow r = \frac{n-2}{n} \tag{3.18}$$

if one coupling hole is done every $n = 4$ cells the ratio is $r = 1/2$. This notation means that the phase advance versus z in the waveguide is two times slower than the phase advance in the cavity. However, due to the placement of the coupling hole every four cells, the phase matching is guaranteed. The equation 3.17 is still valid even if the right term is equal to zero or a multiple of 2π. However the zero term is not possible because the phase advance is always slower in a waveguide and the multiple term of 2π leads to a waveguide with operation too close (or even below) the cut-off frequency as it will be demonstrated in the following.

The phase velocity in a rectangular waveguide for the TE_{10} mode is [41, pp. 117]:

$$v_{ph} = \frac{\omega}{\beta} = \frac{\omega}{\sqrt{k^2 - k_c^2}} = \frac{\omega}{\sqrt{\omega\mu_0\epsilon_0 - \left(\frac{\pi}{a}\right)^2}} = \frac{c}{\sqrt{1 - \left(\frac{c}{2af}\right)^2}} \tag{3.19}$$

[1] In this case the matching is after an even number of cell (even matching). For odd matching the RHS of the equation should be π.

The standard waveguide for X-band is the WR90 dimension with $a = 22.86$ mm and the phase velocity is $v_{ph} = 1.2216\,c$ or in the notation defined above for the phase advance $\phi_w = \frac{1}{1.2216}\pi$. This value can be decreased to required value of $\pi/2$ by tuning the value of a. Inverting eq. 3.19 it is possible to derive the dependence of a versus the desired ratio of the phase advance:

$$a(r) = \frac{1}{2f}\frac{c}{\sqrt{1-r^2}} \tag{3.20}$$

where the equation $r = c/v_{ph}$ has been used to express the ratio factor. For $r = 1/2$, $f = 11.424$ GHz (X-band U.S. frequency) and $\pi-$mode case it is found that the broadwall length of the waveguide should be $a = 15.16151$ mm.

The reduction of the dimension of the waveguide leads to an increased attenuation for the propagating field. The attenuation constant in a waveguide is given by [42, pp. 383]:

$$\alpha = \frac{R_s}{\eta_{TE} b}\frac{1+\frac{2b}{a}\frac{\omega_c^2}{\omega^2}}{\sqrt{1-\frac{\omega_c^2}{\omega}}} \tag{3.21}$$

where $R_s = \sqrt{\frac{\omega\mu}{2\sigma}}$ is the surface resistance and $\eta_{TE} = \frac{\omega\mu}{\beta}$ is the transverse impedance for TE mode.

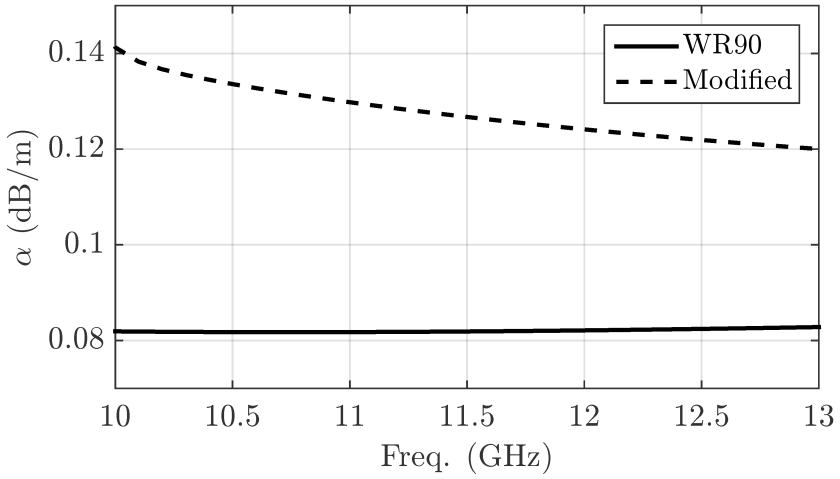

FIGURE 3.8: Attenuation versus the frequency for standard WR90 waveguide (0.0819 dB/m, solid line) and modified waveguide for matching scheme (0.1272 dB/m, dashed line).

The attenuation is increased from 0.0819 dB/m to 0.1272 dB/m, corresponding to a 2.9% power loss for 1 meter section, see fig. 3.8. This value can be tolerated because the attenuation in the cells walls is much greater than the attenuation in the waveguides, as will be proved below.

The above method allows to control the phase along the feeding waveguide and is exact for an isolated waveguide with a forward only wave. For a periodic loaded waveguide the above equations could be used as a guidance. However, as it will be shown in the following, the larger waveguide side a still controls the phase advance in the periodically loaded waveguide.

For this type of structure it is also possible an on-line control of the phase advance for each cell, assuming the availability of three phase shifter and a klystron or four different klystrons for each waveguide. Therefore in this scenario it is possible to accelerate also particles with a velocity lower than c. For example if different particle sources are connected to the LINAC with a single machine it is possible to accelerate electrons and protons [43].

3.2.4 Group Velocity Control

In paragraph 1.6 the space harmonics have been defined. Due to the π periodicity of the dispersion curves all the space harmonics propagates with the same group velocity for a given ω value [1, pp. 58]. Therefore an high frequency signal with a small relative bandwidth, like the LINAC RF power one, propagates undistorted.

The group velocity is a key parameter of an accelerating section. It is related with the filling time and the stored energy. For PCAS structure the group velocity of the propagating Floquet mode can be controlled by variation of the coupling hole area. A parametric study of the coupling hole dimension has been carried out in order to find the dependence of the group velocity versus the hole dimension. In the table 3.1 the group velocities, obtained with numerical simulations, versus the area of the coupling hole are reported. Because the shape of the hole is not a regular polygon it has been approximated with the circumscribed rectangle.

TABLE 3.1: Group velocity *vs.* area of the coupling hole.

Area (mm^2)	vg/c
6.76	0.035
11.62	0.014
30.06	0.009
31.12	0.012
32.13	0.014
33.08	0.017
34.14	0.020
34.99	0.023

The group velocity has a parabolic dependence on the coupling hole area. A monotone relation is not possible because when the cavity and waveguide are completely separated, i.e. coupling hole area is zero, the power propagates with the group velocity

of the simple rectangular waveguide ($\sim 0.8 \cdot c$). On the other hand, when the cavity is completely inserted inside the waveguide, the group velocity is the rectangular waveguide case again. Therefore the group velocity of PCAS decreases from the rectangular waveguide value to a minimum value, close to zero, and then it increases again to the initial value, see fig. 3.9.

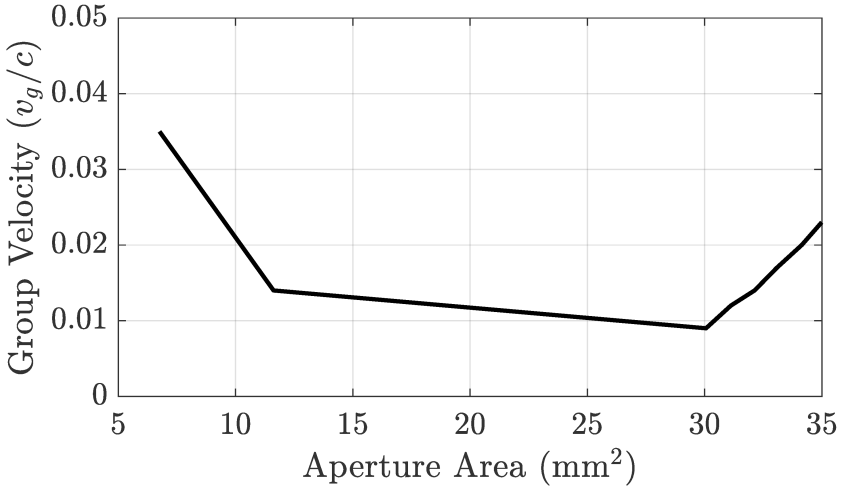

FIGURE 3.9: Group velocity *vs.* area of the coupling hole. Data taken from table 3.1.

Chapter 4

Structure Design and Optimization

In this chapter the design and the optimization process of the PCAS is addressed. In the beginning the 2D profile of the single cell is optimized. In order to increase the shunt impedance a couple of nose cone have been added and the shape of them is optimized for high gradient operation. Afterwards the single cell has been completed with the parallel feeding waveguide and the coupling hole. An extensive study of the chain of the single cell has been done and the S-parameters have been reported. For the two meters section they have been found by means of the cascading technique. The design has been completed with the project of the power branching network from the klystron to the four accelerating waveguide. This network should delivery the RF power with a precise power and phase in order to have efficient acceleration. Finally, a thermal analysis of the structure has been done to find the steady temperature under operation.

4.1 Design Constraints

For single isolated cell of a PCAS the phase advance condition for efficient acceleration can be evaluated with equation (3.20). Here, a π-mode has been chosen for the phase advance per cell. For this value it is possible to match the accelerating structure with the side waveguide by placing a coupling hole every four cells, see fig. 3.7. The value of the group velocity has been found in order to meet a trade-off between RF efficiency and high gradient performance. The main parameters limiting the sustained gradient in accelerating structures is ultra-high vacuum rf breakdown which depend form many perimeters including: the surface peak electric and magnetic field and the power flowing inside the cavity, i.e. the Poynting vector. Accelerating gradient of 125 MV/m and 285 MV/m on surface have been obtained at SLAC in thx X-band [44]. The surface magnetic field is a source of local heating of copper surface. A fast heating with the repetition rate of 1-100 Hz can be a source of high fatigue stress for the copper surface, leading to formation of micro-tips where the electric field can be enhanced by several times and

and may increase the rf breakdown probability. A simple estimation of the temperature rise can be found with equation (1.47) A safe limit for routinely operation should be under 60 °C [45]. This value is found with a very simplified model and the real value of the temperature rise can be different. However the temperature rise can be used as an indication of the RF performance of the structure. In [25] a modified Poynting vector of 5 MW/mm^2 is considered a safe value for routine operation. The minimum desired unloaded gradient is 80 MV/m and the high gradient constraint have been fixed to 285 MV/m for peak surface electric field (E_{max}), 60 °C for the pulse heating and 4 MW/mm^2 for the modified Poynting vector (S_c).

4.2 Optimization of the 2D Profile

The first step of the design of the accelerating structure is the optimization of the 2D cell profile. The 2D layout of the proposed cell is shown in fig. 4.1. It has been chosen with high radius edges in order to reduce the pulse heating and to simplify the machining of the cells when realized as a longitudinal half part. A nose cone has been also added to increase the shunt impedance. The initial dimensions are listed in the following table:

TABLE 4.1: Initial dimensions for the proposed cell.

Name	Value (mm)	Description
C_r	10.0	Cell Radius
C_l	13.13	Cell Length
P_r	1.0	Pipe Radius
N_{ur}	4.0	Nose Cone Upper Radius
N_{lr}	2.0	Nose Cone Lower Radius
N_ul	1.0	Nose Cone Length
C_f	1.0	Cell Fillet
N_{ul}	0.5	Nose Cone Upper Fillet
N_{ll}	0.5	Nose Cone Lower Fillet
P_l	0.5	Pipe Fillet

This bi-dimensional single cell layout of the parallel coupled structure has been extensively studied in order to maximize the shunt impedance. During the optimization of the geometry the ratio of the modified Poynting Vector over the accelerating voltage divided by *r over Q* quantity, $\frac{S_c}{E_{acc}^2}/\frac{r}{Q}$, has been minimized when this minimization is not against the design constraints. This global figure of merit is useful in optimization of the design when high gradient performance are required. For each step the optimum value is highlighted with bold characters.

The dimension which should be optimized at this stage are the length of the nose cone, table 4.2, the upper and the lower radius, tables 4.3 and 4.4 and of the nose cone and the fillet radius. The length of the cell is fixed by the synchronous condition and

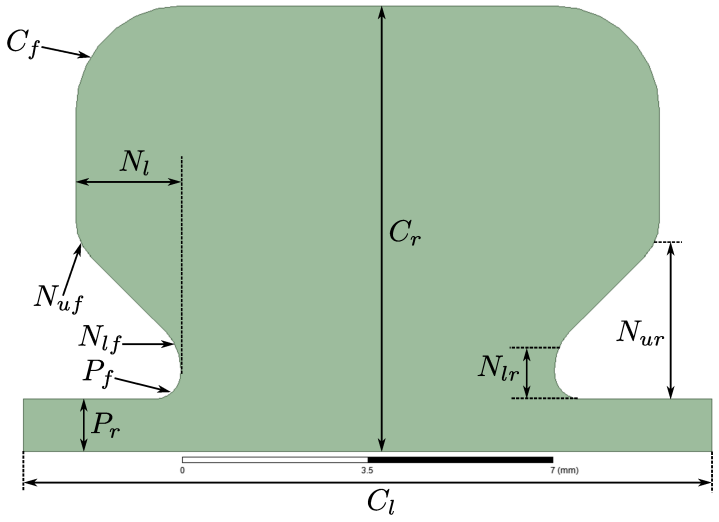

FIGURE 4.1: 2D layout of the accelerating cell.

TABLE 4.2: Optimization of the length of the nose cone.

N_l Value (mm)	R_{sh} (MΩ/m)	Q	En (J)	E_{max} (MV/m)	H_{max} (kA/m)	S_c (MW/mm^2)	E_a (MV/m)
1.0	166	8656	0.0617	215	200	1.65	78.6
1.5	**159**	**8232**	**0.0625**	**251**	**220**	**2.30**	**81.4**
2.0	155	7712	0.0655	298	248	3.23	85.0
2.5	145	7110	0.0710	333	284	4.61	88.9

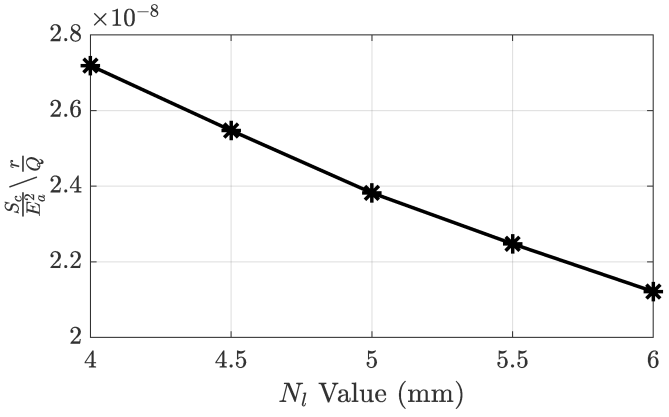

FIGURE 4.2: Plot of $\frac{S_c}{E_a^2} \backslash \frac{r}{Q}$ versus the dimension of the length of the nose cone (N_l).

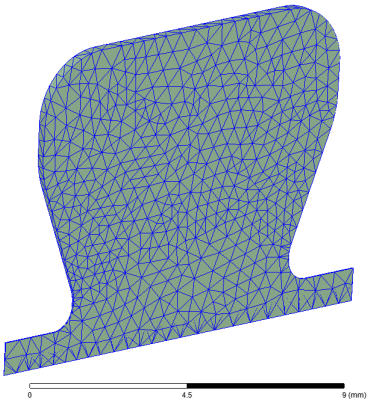

FIGURE 4.3: Mesh of the quasi 2D simulation.

the radius of the cell has been tuned for every value of the sweep in order to make a comparison only for cells tuned to the operational frequency. This tuning is a very long process and has been done with an automatized procedure exploiting the OLE language of Ansys HFSS and MATLAB, see Appendix A for details. A quasi 2D simulation can be carried out in HFSS when a small slice of the structure is simulated (5 degrees or fewer) and closing the newly created radial walls with a perfect-H boundary condition. This technique exploits the automatized procedure and the possibilities of a commercial code and the speed of a quasi-2D simulation by allowing a fast and precise optimization of the cell layout.

TABLE 4.3: Optimization of the upper radius of the nose cone.

N_{ur} Value (mm)	r_s (MΩ/m)	Q	En (J)	E_{max} (MV/m)	H_{max} (kA/m)	S_c (MW/mm^2)	E_a (MV/m)
4.0	175	7994	0.0598	342	250	4.12	84.8
4.5	170	7938	0.0611	300	247	3.86	84.8
5.0	166	7870	0.0634	292	248	3.67	85.5
5.5	161	7791	0.0635	292	246	3.39	84.6
6.0	**156**	**7712**	**0.0655**	**298**	**248**	**3.23**	**85.0**

TABLE 4.4: Optimization of the lower radius of the nose cone.

N_{lr} Value (mm)	r_s (MΩ/m)	Q	En (J)	E_{max} (MV/m)	H_{max} (kA/m)	S_c (MW/mm^2)	E_a (MV/m)
2.0	**159**	**8232**	**0.0598**	**251**	**220**	**2.30**	**81.4**
2.5	155	8088	0.0611	245	231	2.74	82.6
3.0	150	7939	0.0634	218	240	3.03	82.9
3.5	144	7771	0.0635	221	249	3.27	82.8
4.0	138	7581	0.0687	219	260	3.39	82.6

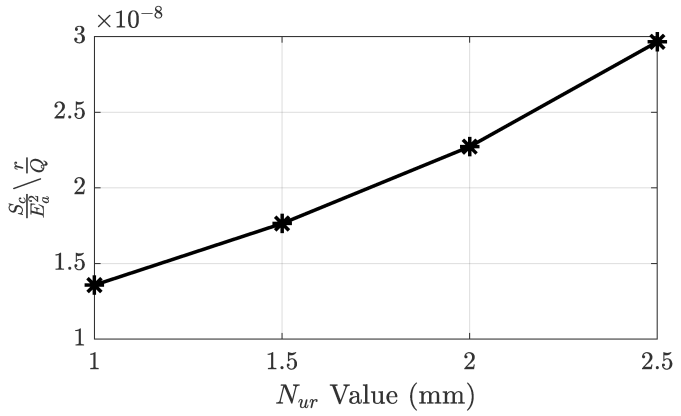

FIGURE 4.4: Plot of $\frac{S_c}{E_a^2} \backslash \frac{r}{Q}$ versus the dimension of the upper radius of the nose cone (N_{ur}).

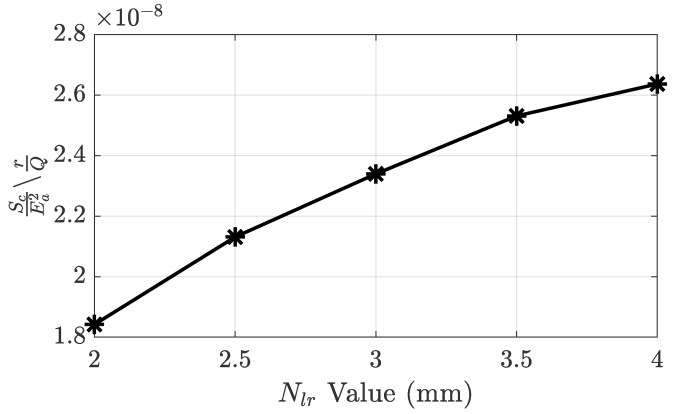

FIGURE 4.5: Plot of $\frac{S_c}{E_a^2} \backslash \frac{r}{Q}$ versus the dimension of the lower radius of the nose cone (N_{lr}).

The fillet radius variation can affect only one figure of merit: the maximum surface electric field. In the 4.5, 4.6 and 4.7 tables the dependence of the maximum surface electric field versus the fillet radius are summarized.

TABLE 4.5: Optimization of the fillet external radius of the nose cone (N_{uf}).

N_{uf} Value (mm)	E_{max} (MV/m)	H_{max} (kA/m)	S_c (MW/mm^2)
1.0	251	220	2.30
2.0	271	220	2.31
3.0	**233**	**221**	**2.33**

The electric, magnetic and the modified Poynting vector for the bi-dimensional case are plotted in the following figures. The maximum electric field is located in inner radius of the nose cone as expected. It reached the maximum value of 238 MV/m when the mean accelerating gradient is 81.4 MV/m. The maximum surface magnetic field is equal

TABLE 4.6: Optimization of the fillet radius of the pipe (P_f).

P_f Value (mm)	E_{max} (MV/m)	H_{max} (kA/m)	S_c (MW/mm^2)
0.4	269	220	2.33
0.5	251	220	2.30
0.6	245	221	2.33
0.7	**238**	**220**	**2.30**

TABLE 4.7: Optimization of the fillet internal radius of the nose cone (N_{lf}).

N_{lf} Value (mm)	E_{max} (MV/m)	H_{max} (kA/m)	S_c (MW/mm^2)
0.5	256	221	2.41
1.0	**238**	**220**	**2.30**
1.5	246	221	2.27

to 220 kA/m and it is located in the top part of the nose cone. The maximum value of the modified Poynting vector is 2.30 MW/mm^2 and it is in the middle part of the nose cone.

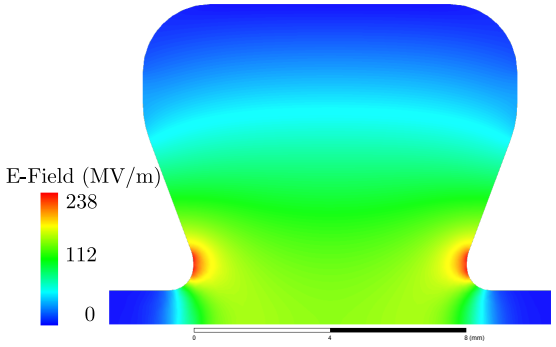

FIGURE 4.6: Plot of the electric field for the 2D layout of the cell. Fields neutralized to accelerating gradient of 100 MV/m.

The RF parameters of the final 2D layout are summarized in table 4.8. The PCAS is compared to the CLIC-G T24 design. The peak input power in this table is computed with the rule of equation (1.12), so in this case the peak input power is doubled respect to the original table. The unloaded gradient for this project is 81.4 MV/m. This conservative value has been chosen because, as it will be seen below, is the maximum gradient achievable with a single klystron for the whole structure. The group velocity will be calculated later for using the 3D geometry. The high gradient figures of merit have comparable values with the CLIC-G T24 design. The maximum electric field is slightly higher due the presence of the nose cone, but the modified Poynting vector is an almost 50% lower. The maximum pulse heating temperature is roughly 15 K for a pulse length of 200 ns.

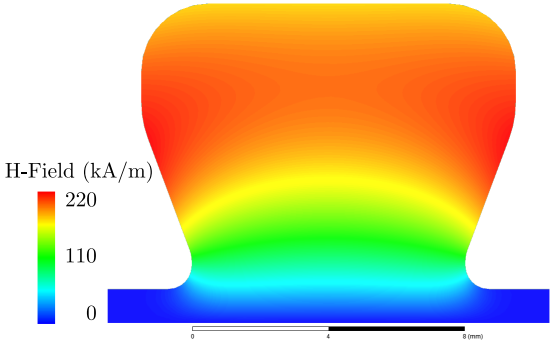

FIGURE 4.7: Plot of the magnetic field for the 2D layout of the cell. Fields neutralized to accelerating gradient of 100 MV/m.

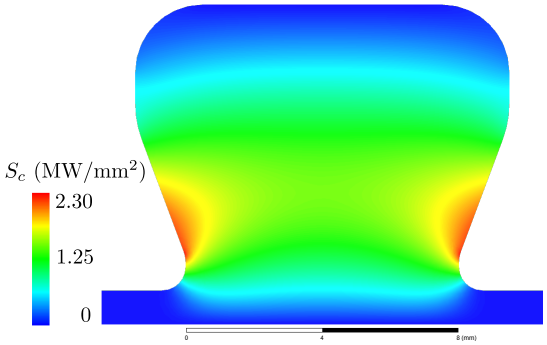

FIGURE 4.8: Plot of the modified Poynting vector for the 2D layout of the cell. Fields neutralized to accelerating gradient of 100 MV/m.

TABLE 4.8: RF parameters of the 2D cell. Maximum temperature rise is calculated for pulse length of 200 ns.

Parameters	Clic-G T24	Parallel Coupling
Input/Output radii (mm)	3.15/2.35	1.00
Shunt impedance (MΩ/m)	116/150	159
Quality factor	∼5600	∼8200
Maximum E-Field (MV/m)	222	272
Maximum modified Poynting vector (MW/mm^2)	3.51	2.30
Maximum pulse heating temperature rise (K)	14	15

4.3 Optimization of the 3D Layout

The 3D layout is derived from the 2D one with the addition of the parallel waveguide and the coupling hole between the waveguide and the cell. The major dimension a of the waveguide is already fixed by phase matching and the minor dimension b is equal to the standard WR90 waveguide.

In the 3D layout the fillet of the coupling hole is the point with the maximum magnetic field and maximum modified Poynting vector. Therefore for the 3D layout an optimization step for the fillet radius has been carried out. As it is possible to see in the

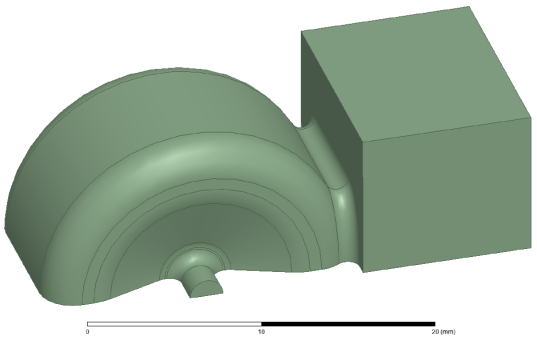

FIGURE 4.9: 3D model of the cell cavity with the waveguide feeding.

table 4.9 only H_{max} and S_c values have a significant difference respect to the final values of the 2D layout, see table 4.4.

TABLE 4.9: Optimization of the fillet radius of the pipe.

Value (mm)	r_s $(M\Omega/m)$	Q	En (J)	E_{max} (MV/m)	H_{max} (kA/m)	S_c (MW/mm^2)	E_a (MV/m)
0.6	161	8714	0.0658	274	495	4.41	81.5
0.7	**161**	**8892**	**0.0669**	**272**	**484**	**3.99**	**81.7**
0.8	160	8894	0.0685	262	476	4.22	81.5
0.9	159	9194	0.0696	255	477	4.30	81.2
1.0	161	9295	0.0724	254	473	4.85	81.6

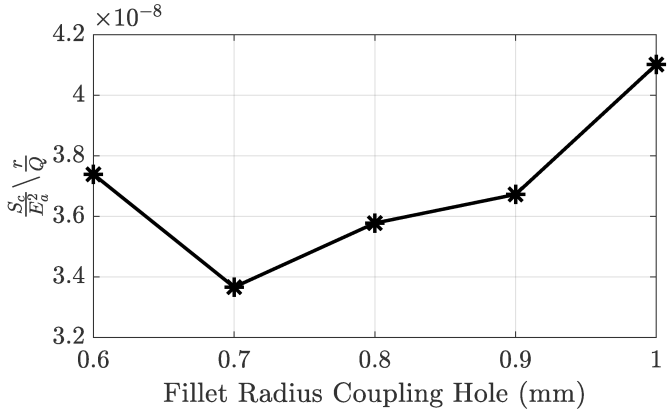

FIGURE 4.10: Plot of $\frac{S_c}{E_a^2} \backslash \frac{r}{Q}$ versus the fillet radius of the coupling hole.

A fillet radius of 0.7 mm minimizes the $\frac{S_c}{E_a^2} \backslash \frac{r}{Q}$ quantity and therefore this value has been chosen for the final design, see fig 4.10. The plot of the electric, magnetic and modified Poynting vector for the 3D layout of the cell are shown in fig. 4.11-4.13. The maximum values for the electric, magnetic and modified Poynting vector are respectively, 272 MV/m, 484 kA/m and 3.99 MW/mm^2. The corresponding maximum pulse heating is 42 degree °C for a pulse of 200 ns.

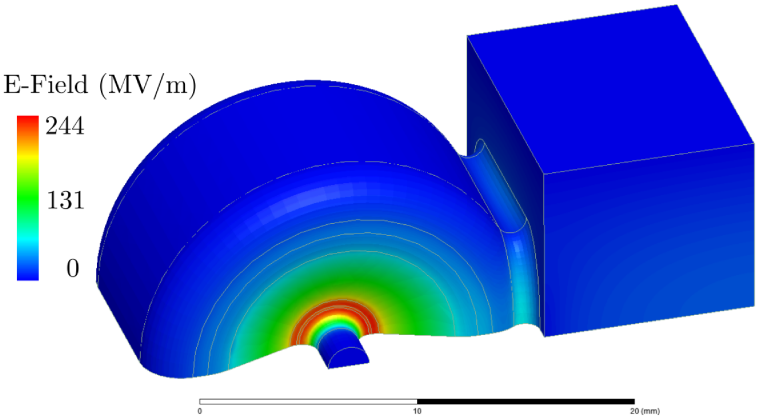

FIGURE 4.11: Plot of the electric field for the 3D layout of the cell. Fields neutralized to accelerating gradient of 100 MV/m.

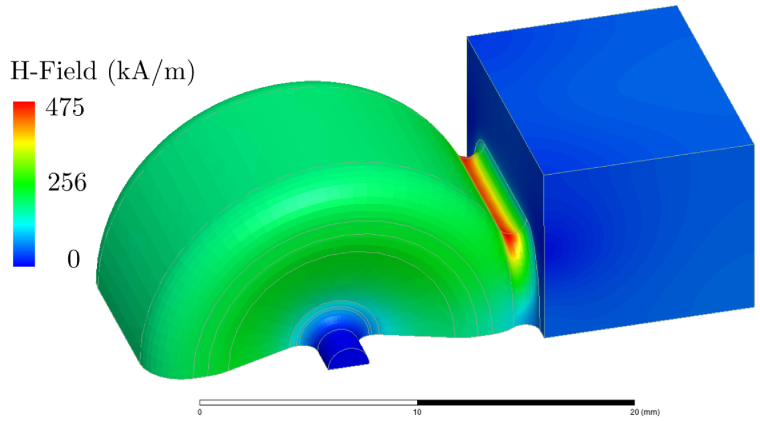

FIGURE 4.12: Plot of the magnetic field for the 3D layout of the cell. Fields neutralized to accelerating gradient of 100 MV/m.

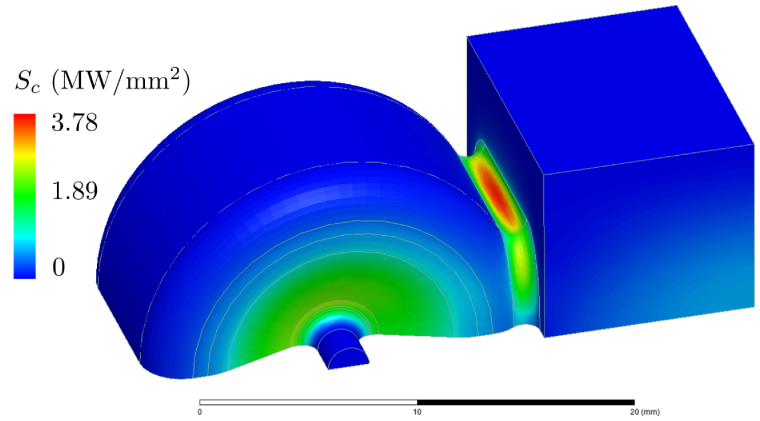

FIGURE 4.13: Plot of the modified Poynting vector for the 3D layout of the cell. Fields neutralized to accelerating gradient of 100 MV/m.

4.4 Elementary Cell and Power Matching

The elementary cell of the PCAS is shown in fig. 4.14. This cell consist of the cell with the coupling hole and the waveguide. This latter has been extended by two and half periods in the z negative direction and half period in the z positive direction for a total length of four periods.

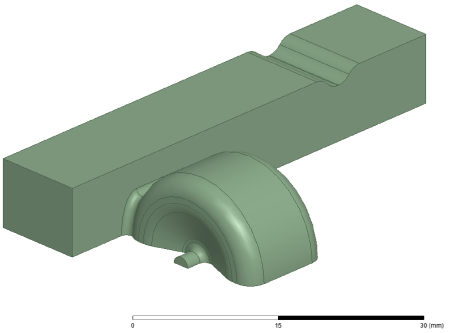

FIGURE 4.14: 3D model of the matched elementary cell by means of inductive bumps.

The elementary cell with the cavity cell and the matching bumps has a phase advance greater of 2π. As it can be seen in the fig. 4.15, after a length equal to four periods the phase is not exactly 2π but it is slightly greater. This difference respect to the simple analytical case is due to the presence of the bumps and the cavity matching hole non contemplated in the analytical model. Therefore, it is necessary to slightly tune the waveguide in order to re-obtain the nominal case of 2π as phase advance after four periods.

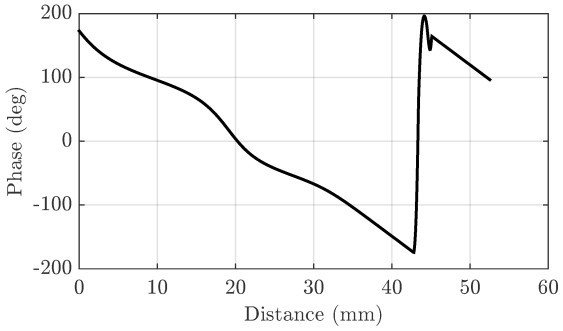

FIGURE 4.15: Phase of the electric field in the waveguide. After a four periods length the phase advance is greater than 2π.

In order to match the input impedance of the waveguide with the output one it is necessary to add a couple of inductive irises before the cavity cell. In this way the capacitive load of the cavity cell is compensated. The final matched elementary cell $|S_{11}|$ parameter is shown in fig. 4.16 (top left) with a value roughly equal to -50 dB at the operation frequency. An inconvenient of this resonant matching of the two port device is

the narrow band typical of resonant matching. The S_{21} parameter has been plotted for both amplitude and phase in fig. 4.16 (top right and bottom left). For the 11.424 GHz frequency the magnitude is 0.9911 (-0.0775 dB) and the phase advance, after the tuning of the waveguide, is nearly zero as it should be. Finally, the magnitude in dB of the S_{22} is shown in fig. 4.16 (bottom right) and the elementary cell is also matched in the inverse direction.

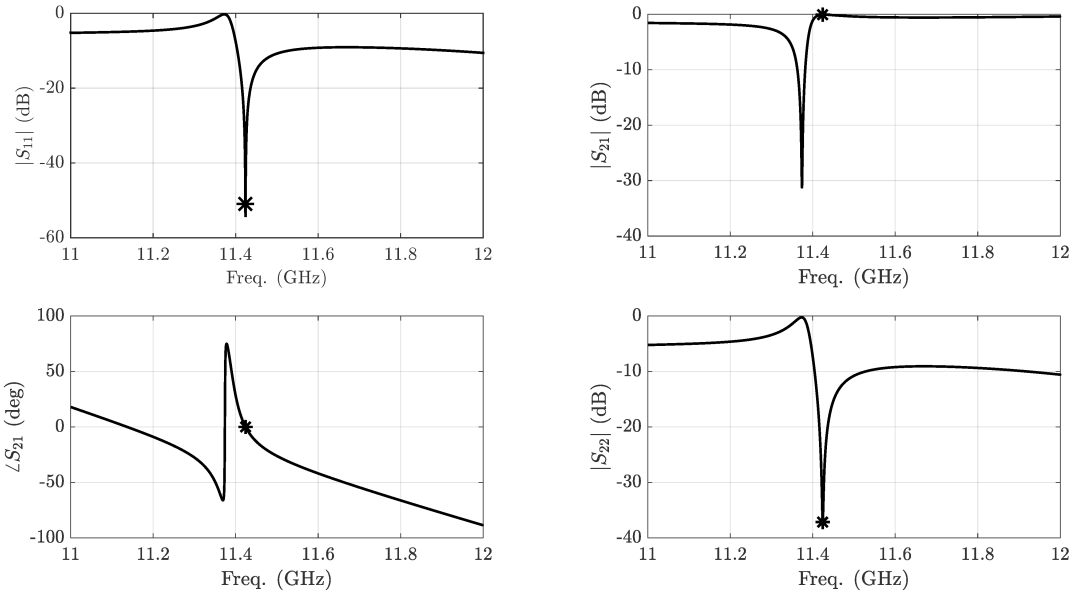

FIGURE 4.16: Plot of the $|S_{11}|$ (top left), $|S_{21}|$ (top right), $\angle S_{21}$ (bottom left) and $|S_{22}|$ (bottom left) versus frequency for the matched unit cell by means of the inductive bumps.

4.5 Group Velocity and Dispersion Curve

One of the most important RF parameter for an accelerating structure is the group velocity. If the group velocity is too low the filling time will be too high, on the contrary if the group velocity is too high the efficiency of the section is too low and to store the required energy an higher input power is needed (see par. 1.6.1). The group velocity for periodic structure can be calculated with the following formula [10]:

$$v_g = \frac{P_{in}}{w} \tag{4.1}$$

where P_{in} is the average input power and w the stored energy per meter, see table 1.1. For the elementary cell in figure 4.14 the stored energy per unit length is equal to 0.71688 Joule for an input power of 19 MW. Then, the group velocity is equal to $0.088 \cdot c$.

The dispersion curve is a plot of the resonant frequency versus the phase advance per cell of the periodic structure. The phase advance is imposed between the two faces of the

rectangular waveguide with a condition of master and slave in HFSS. The fields on these faces are imposed as identical but with a phase offset defined in the pre-processing phase of the simulation. The eigen-mode solver computes all the natural resonant frequencies with these boundary conditions. The master and slave condition for the elementary cell is set on the waveguide ports. The field for both modes in the middle of the iris is zero so a second condition of phase advance between the two iris does not affect the results. The resonant frequencies versus the phase offset imposed is the dispersion diagram, fig 4.17. The cavity mode is crossed by the speed of light line for a phase advance of 360 degree. Because in the waveguide the phase advance should match a $2 \cdot c$ phase velocity the equation (1.38) has been multiplied by a factor two. For ease of reading the dispersion diagram is extended up to the 450 degree phase shift.

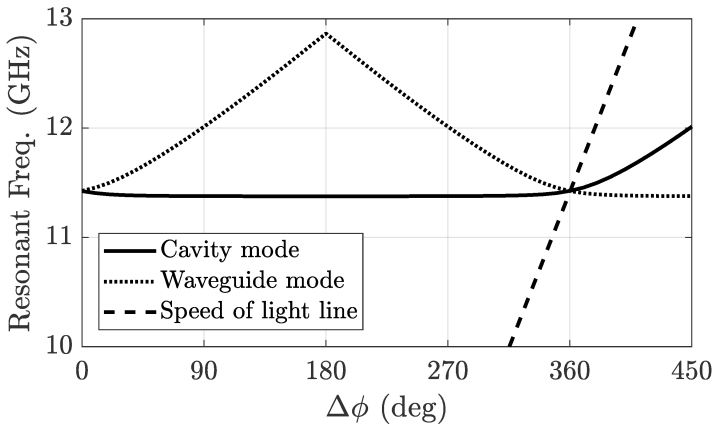

FIGURE 4.17: Plot of dispersion curve for the cavity mode and waveguide propagating mode. The resonant frequency of the cavity mode at 360 phase advance is 11.424 GHz.

The structure has single operating mode at the working point of 2π. The modes have a confluence point in the operational frequency of 11.424 GHz. The group velocity has been also calculated as the derivative of the $\omega - k$ curve, see fig. 4.18, and the results ($0.08 \cdot c$) is very close to the value obtained with the equation (4.1).

A better result can be obtained by a 4th order polynomial fit of the $\omega - k$ numerical data which is shown in fig. 4.19. In this case the value of the group velocity calculated as the derivative of the $\omega - k$ curve is $0.085 \cdot c$.

The general approach of using resonant oscillator to tune the structure is called resonant coupling [1, pp. 117]. In a resonant coupled accelerating section the highest frequency of the fundamental mode and the lowest of first HOM are coincident and the stopband is closed. The union of the two passband is called confluence. As a result the separation between adjacent modes and the power flow is optimized [1, pp. 118]. This technique is generally employed in Drift Tube LINAC (DTL) for protons [29].

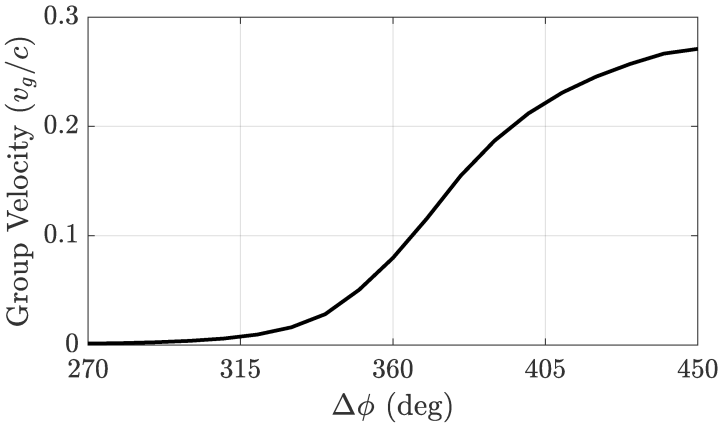

FIGURE 4.18: Group velocity from the derivative of the $\omega - k$ curve.

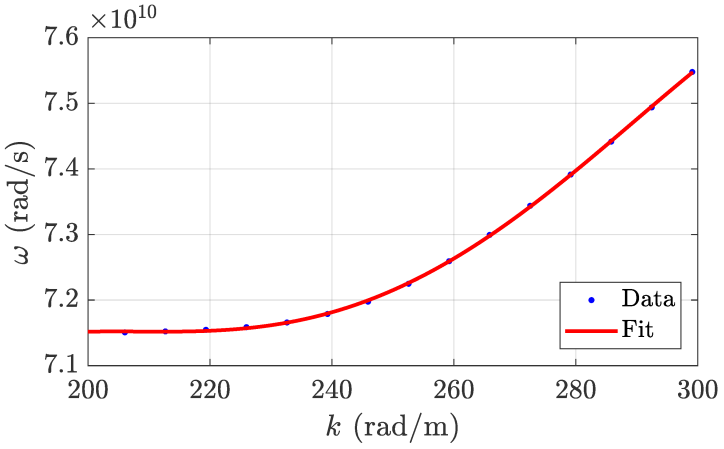

FIGURE 4.19: Polynomial fit of the $\omega - k$ curve.

4.5.1 Group Velocity Tuning

The group velocity of the PCAS can be tuned by a variation of the coupling hole between the waveguide and cell. When the waveguide and the cell are not coupled, i.e. area of the hole is zero, the group velocity is the same of the lateral waveguide. While the area of the hole increases the group velocity changes[1]. This variation is shown in the left panel of the fig. 4.20. A parabolic variation of the group velocity with the growing of the hole aperture area is found, see also par. 3.2.4. The minimum value is within 45 and 55 mm^2 and a group velocity lower than $0.1 \cdot c$ is found in this range. Otherwise, the modified Poynting vector has a maximum in the rounding of the coupling hole, see fig. 4.13.

Also for S_c a parabolic behaviour is found. Indeed for larger coupling hole a rounding with a larger radius is possible which allows for a lower value of modified Poynting vector. But, for wider aperture hole the group velocity is higher, i.e. the structure

[1]The area value is approximated with the circumscribed rectangle.

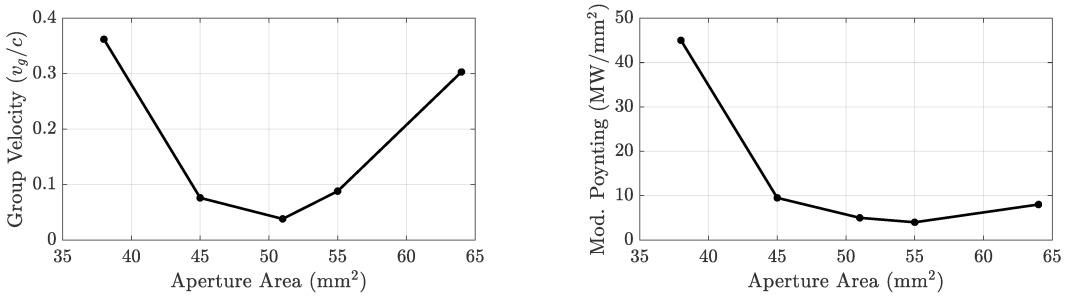

FIGURE 4.20: Group velocity (left) and modified Poynting vector (right) as function of the aperture hole area. The modified Poynting vector is neutralized for a 80 MV/m average accelerating gradient.

is lesser efficient and more power is necessary for the desired average gradient. The dependence of S_c versus the coupling hole area is plotted in the right panel of the fig. 4.20. Therefore, a compromise between the minimum value of the modified Poynting vector and the desired value of the group velocity should be find. For this design a group velocity of $0.085 \cdot c$ and the minimum value of the modified Poynting vector has been chosen.

4.6 RF Parameters

In the previous paragraph we found the value of the group velocity for the PCAS. The attenuation constant τ is, therefore, equal to:

$$\tau_0 = \alpha_0 L = \frac{\omega_{RF}}{2 Q v_g} L \tag{4.2}$$

where L is the total length, see par. 1.6.1. For L=2 meters and Q ≅8200, τ_0 is equal to 0.33. The filling time for a 2 meters section with a pulse group velocity of $0.088 \cdot c$ is equal to 75 ns. For the calculation of the maximum pulse heating due to the magnetic field a pulse length of three filling time has been taken into account.

In table 4.10, a comparison of the RF parameters with two other designs is summarized. The PCAS has been compared with the CLIC-G T24 and RDDS1 accelerating section [46], [47], [48], [49].

Both CLIC-G T24 and RDDS1 are $2\pi/3$ mode TW constant gradient structure, thus for group velocity and iris radius is reported the maximum and minimum value. All three designs have a large value of shunt impedance and can operate in the high gradient regime. For RDDS1 structure the maximum electric field, the modified Poynting vector and the pulse heating values are not available in literature. A simplified model of the single cell has been drawn and simulated with HFSS for a roughly estimation of them.

TABLE 4.10: RF parameters of the 3D cell. Maximum temperature rise for PCAS is calculated for pulse length of 200 ns.

Parameters	Clic-G T24	RDDS1	Parallel Coupling
Structure type	Const. gradient	Const. gradient	Const. impedance
Length (m)	0.3	1.8	2
Phase Adv.	$2\pi/3$	$2\pi/3$	π
Unloaded gradient (MV/m)	100	50	80
Input/Output radii (mm)	3.15/2.35	5.605/3.885	1.00
a/λ	0.12	0.18	0.038
Group velocity (v_g/c)	0.018/0.009	0.11/0.03	0.09
Attenuation, τ_0	1.88	0.48	0.33
Quality factor	∼5600	∼7800	∼8200
Shunt impedance (MΩ/m)	116/150	77/100	161
R over Q (Ω)	26700	12800	19600
Peak Input Power (MW)	75	82	152
Filling time (ns)	57	104	75
Maximum E-Field (MV/m)	222	∼350	272
Max. mod. Poynting vector	3.51	∼20	3.99
Pulse heating rise	14	∼90	42

4.7 Chain of the Single Cell

The single period of the accelerating section can extended in a periodic structure. Three cases have been taken into account: a four cells chain of a single arm of the complete section, four single arms, each of them with four cells for a total number of cells of sixteen, with the appropriate interpolation distance, each with and a single arm chain of forty cells which has an approximate length of two meters.

4.7.1 Four Cell Structure

Before simulating the whole accelerating structure an intermediate step has been taken into account: four unit cell studied in the previous paragraph has been joined in order to study performances of a single arm, see Fig 4.21.

The matching, as expected, is the same for the operation frequency, fig. 4.22, with a value slightly greater of −50 dB. The S_{21} parameter is shown for both amplitude and phase in fig. 4.22 (top right and bottom left). For the 11.424 GHz frequency the magnitude is −0.316 dB and the phase difference $\angle S_{21}$ is −0.16 deg. The magnitude in dB of the S_{22} is shown in fig. 4.22 (bottom right).

A finite conductivity of 5.8×10^7 S/m (nominal value for copper alloy) for cavity walls has been added in order to simulate the RF losses and to numerically quantify the attenuation in the waveguide/accelerating section. As it is possible to see in fig. 4.23 the difference between the first and fourth cell is around the 3% for the maximum electric field: the attenuation is then equal to 0.26 dB for this section with a 21 cm length.

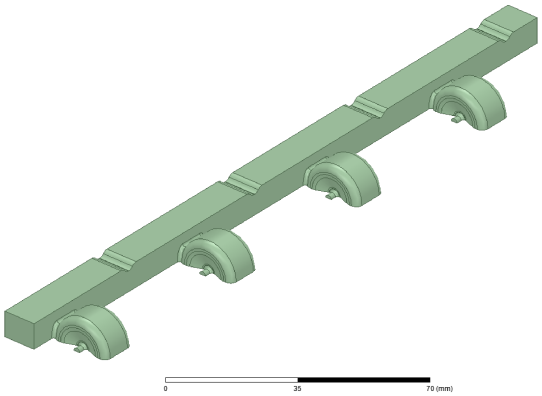

FIGURE 4.21: The 3D model of a single arm with four cells and a symmetry plane.

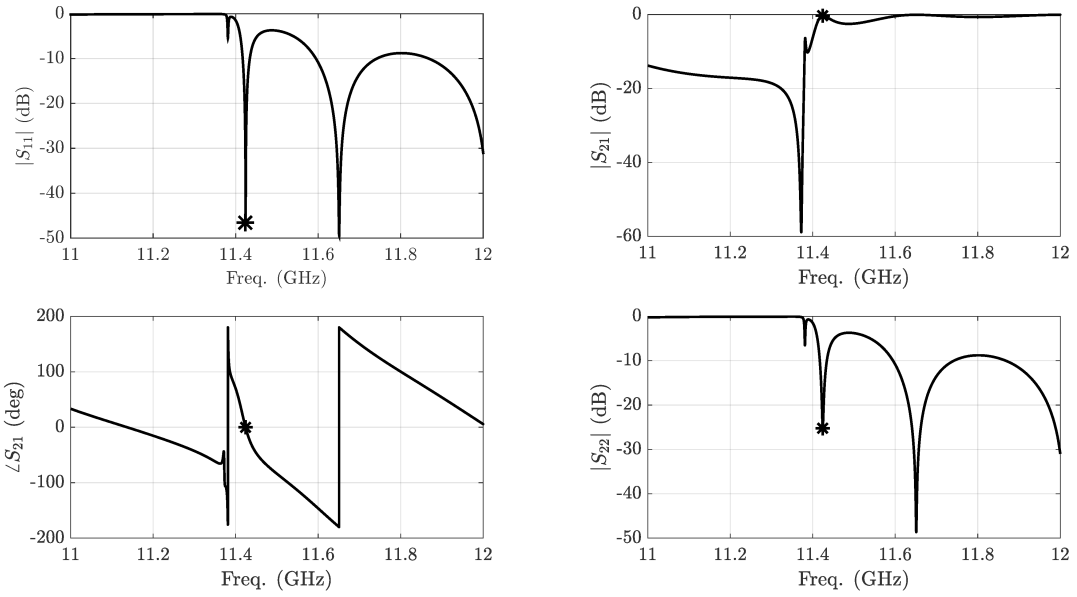

FIGURE 4.22: Plot of the $|S_{11}|$ (top left), $|S_{21}|$ (top right), $\angle S_{21}$ (bottom left) and $|S_{22}|$ (bottom left) versus frequency for the 3D model with four cells.

Therefore the attenuation constant per meter is 1.26 dB/m. For this kind of structure a large fraction of the power is available after the end of a section with a length of one meter (a quite large value for X-band accelerating section). This power can be refilled of the missing fraction with a directional coupler and injected in the next section[2]. In the case of a two meter long section the residual power to the RF load is equal to roughly $0.7 \cdot P_{in}$.

[2]In order to do this it is also necessary to include a phase shifter in order to match the bunch and RF phase at the beginning of the section

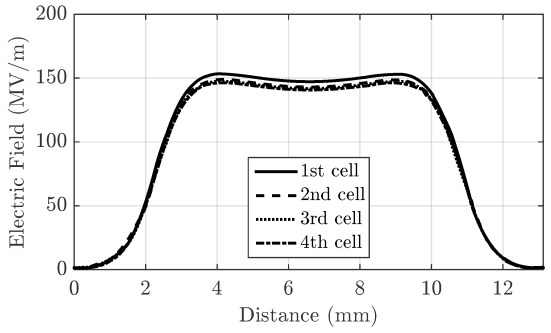

FIGURE 4.23: Field of the four cell device.

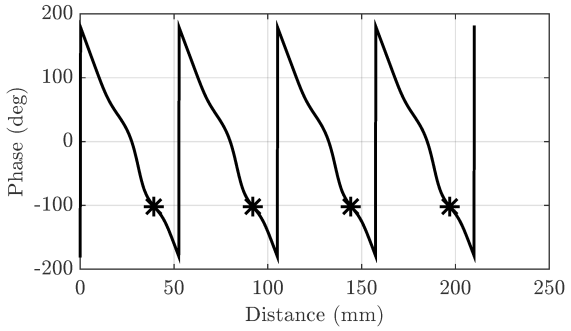

FIGURE 4.24: Phase of the four cell device.

4.7.2 Sixteen Cells Structure

A section with four waveguides and 16 cells has been simulated in ANSYS HFSS with a composite excitation simulation. For this type of simulation the S-parameter are not available because each port is excited together with the others. For each waveguide an input power of 38 MW should be provided. Therefore the total RF power is roughly equal to 150 MW. This value is challenging but feasible with a 50 MW klystron output compressed with SLED with a factor three [50]. The phase of the electric field has to be shifted of 180 deg from port n to port $n+1$ because of the phase matching scheme used.

The phase of the electric field inside the first arm is plotted in fig. 4.26. From left to right the values of the phase are: 78.21, 77.86, 77.58, 77.27 deg all the phases are required to be equal and the maximum excursion is under ± 0.5 deg around the mean value of these values. The amplitude and the phase on the axis of the PCAS are shown in the fig. 4.27 and 4.28. The amplitude of the electric field on axis is equal for every four consecutive cells. The difference between the first and the last group amplitude is about of 3% for this section with a length of 21 cm. As it has been stated before, the losses in the waveguide are only a small fraction of the total RF losses. The percentage decrease of the power for unit length is around the 15%/m (1.32 dB/m) with a 4/5 fraction from the cavity walls and 1/5 from waveguides. The phase shift of every cell on the axis of the

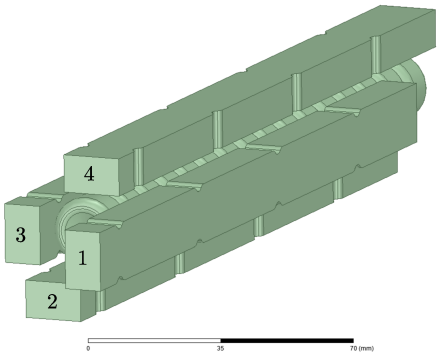

FIGURE 4.25: Isometric view of the 3D CAD model of the full structure. Ports number are shown.

PCAS, as expected, is 180 deg. Some numerical errors are present near the iris where the field is zero and it is difficult to compute the phase.

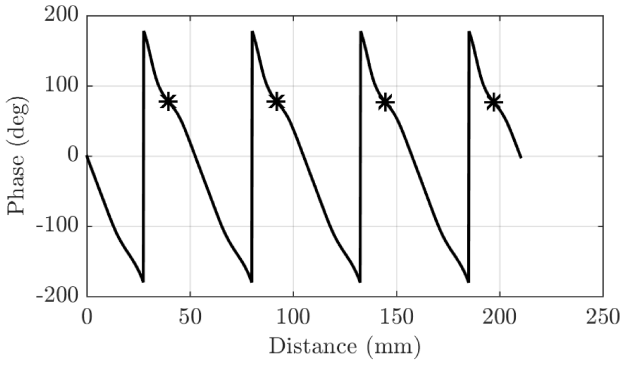

FIGURE 4.26: Plot of the phase in the middle of the coupling hole for the first waveguide (axis of the waveguide). The phase coupling value are within ±0.5 deg.

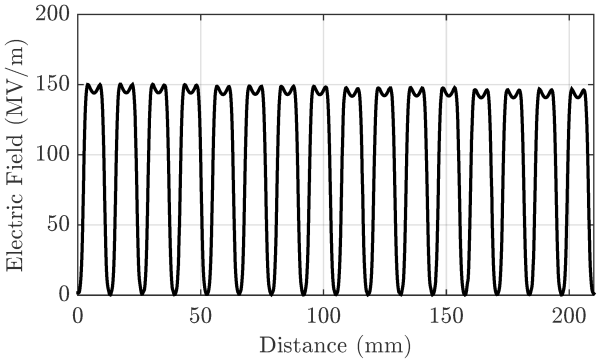

FIGURE 4.27: Plot of the complex magnitude electric field on axis. The electric field is decreasing due to the losses in waveguide and cells.

The PCAS with a fixed coupling hole can be considered the equivalent version of constant impedance section. Since the attenuation per unit length for this kind of

structure is very low the electric field is quasi-constant and for most application this implementation should be sufficient. If a truly constant electric field is required the coupling holes should be tuned in order to vary the delivered power to each cell along the z-axis. But unlike the constant gradient structure the holes have to be smaller in the beginning, less power coupled when more total power is available, and bigger for the last cells.

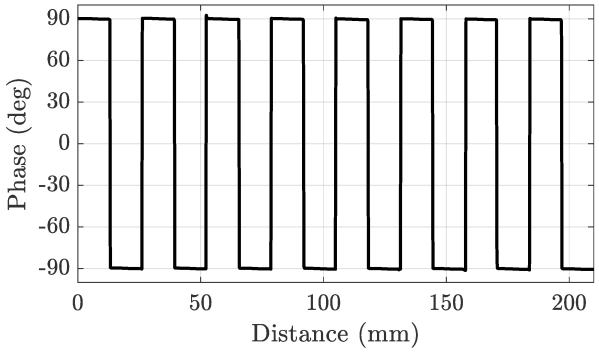

FIGURE 4.28: Plot of the phase on axis of the accelerating structure. Every cell there is a phase shift of 180 deg. For ease of reading the mean value of phase has been imposed as zero.

4.7.3 Two Meters Section

For the evaluation of the S-parameter for the two meter section it is possible to employ an analytical approach with the results of the single cell. By this way the S-parameters are estimated without the need of a time consuming simulation of the whole section. It is well know from the literature that the S-parameters of chained microwaved devices can be obtained with the *cascading* technique. In the simplified case of a two ports microwave device in order to do that the $ABCD$, or transmission, matrix should be used [41, pp. 188]. The relation between the S-parameters and the ABCD terms are listed below:

$$A = \frac{(1+S_{11})(1-S_{22})+S_{12}S_{21}}{2S_{21}} \tag{4.3}$$

$$B = Z_0\frac{(1+S_{11})(1+S_{22})-S_{12}S_{21}}{2S_{21}} \tag{4.4}$$

$$C = \frac{1}{Z_0}\frac{(1-S_{11})(1-S_{22})-S_{12}S_{21}}{2S_{21}} \tag{4.5}$$

$$D = \frac{(1-S_{11})(1+S_{22})+S_{12}S_{21}}{2S_{21}} \tag{4.6}$$

where Z_0 is the characteristic impedance of the line. The $ABCD$ matrix of a device can be simply chained by multiplying it with the matrix of the subsequent device. For the

simplified case of n identical devices the $ABCD$ final matrix is therefore:

$$\begin{bmatrix} A & B \\ C & D \end{bmatrix}_n = \begin{bmatrix} A & B \\ C & D \end{bmatrix}^n \tag{4.7}$$

It is possible to re-obtain the S-parameters with the inverse relations:

$$S_{11} = \frac{A + B/Z_0 - CZ_0 - D}{A + B/Z_0 + CZ_0 + D} \tag{4.8}$$

$$S_{12} = \frac{2(AD - BC)}{A + B/Z_0 + CZ_0 + D} \tag{4.9}$$

$$S_{21} = \frac{2}{A + B/Z_0 + CZ_0 + D} \tag{4.10}$$

$$S_{22} = \frac{-A + B/Z_0 - CZ_0 + D}{A + B/Z_0 + CZ_0 + D} \tag{4.11}$$

The $|S_{11}|$ parameter for a 2 meter long section is shown in the figure 4.29. The -10 and -20 dB bandwidth are 3 MHz and 700 kHz. The $|S_{21}|$ is shown in the top right panel of the figure 4.29 and a numerical value of -2.43 dB is found, which is in according with the value found in the paragraph 4.7.1. After two meters section the accumulated phase shift is nearly zero (0.5 deg), see fig. 4.29, bottom left panel.

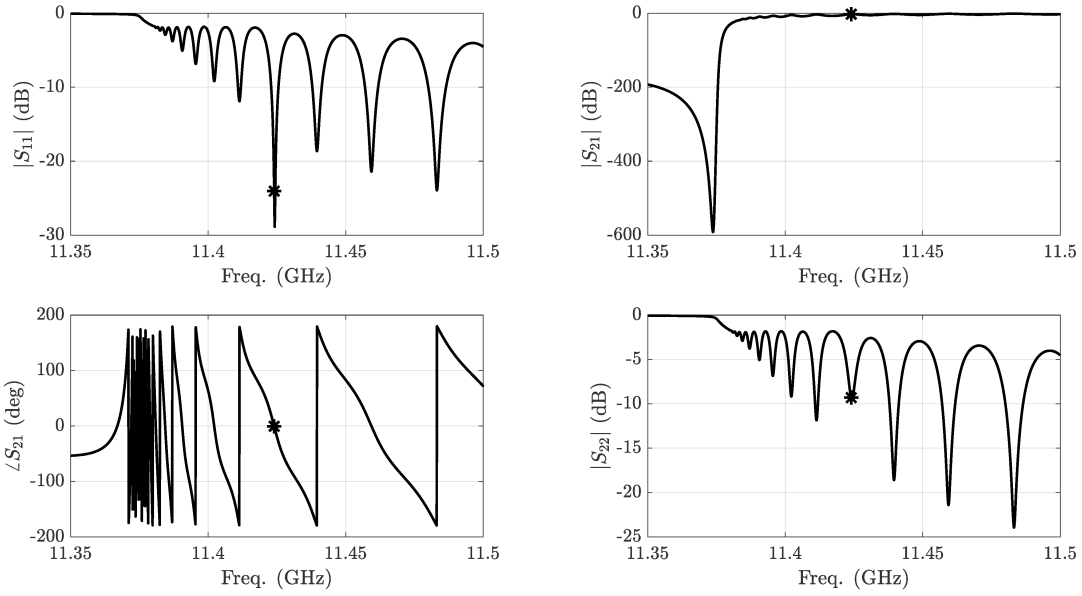

FIGURE 4.29: Plot of the $|S_{11}|$ (top left), $|S_{21}|$ (top right), $\angle S_{21}$ (bottom left) and $|S_{22}|$ (bottom left) versus frequency for the two meters section.

The $|S_{22}|$ value at the nominal frequency is roughly -10 dB, see fig. 4.29, bottom right panel.

The curves have been calculated within a circuit design of ANSYS Electronic Desktop where the single cell element S-parameters are stored inside a standard *.s2p* file.

For the nominal frequency the $|S_{11}|$ parameter has been cross-checked with an analytical script which implements the equations from (4.3) to (4.11).

4.8 Splitter and Taper

The accelerating section designed so far has no direct connection to the RF power source. Therefore, it is necessary to design a custom splitter which can divide the power and deliver the correct phase for each waveguide arm. The power for each arm must be the same but the phase at the input ports is not equal because the second port must have a 180 deg shift compared to the first, the third from the second and the last from the third. Also each waveguide input is physically shifted by one *period* compared to the previous one. The optimization of these splitters has three objectives:

- amplitude balancing $||S_{31}|-|S_{21}||< 0.01$ dB
- correct phase delivering $\angle S_{31} - \angle S_{21} = 180 \pm 0.05$ deg
- impedance matching $|S_{11}|< -50$ dB

this constraint values are compatible with a high precision milling manufacturing with a tolerance of few microns.

The initial design has been created in Ansys HFSS with a full parametrized model. In order to reduce the space parameters which affect these requirements a simple geometry has been adopted, see fig. 4.30. The arm directly connected to the waveguide of the accelerating structures should be considered with fixed dimension and position. In order to avoid the design of a taper from the standard WR90 waveguide to the waveguide designed for the PCAS the straight arm has standard WR90 dimensions. Four parameters have been optimized in order to achieve the proposed goals:

- Position of the Splitting Bump (PSB)
- Position of the WR90 Arm (PWA)
- Dimension of the Matching Bump (DMB)
- Position of the Matching Bump (PMB)

in the parenthesis the acronym used in the next. The PSB parameter is necessary in order to match the amplitude at the input port of the PCAS. The PWA value must be tuned in order to match the phase difference. With the modification of position of the WR90 arm it is possible increase or reduce the electrical path of the waves from the splitting point to the output ports. The two parameters of the matching bumps are used to match the structure.

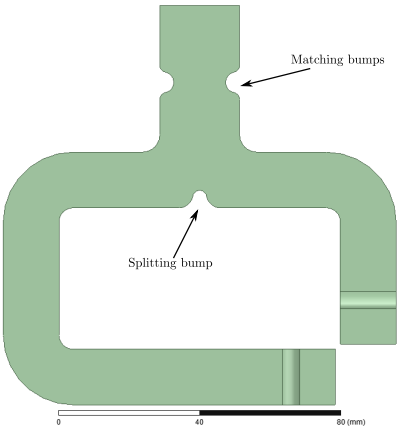

FIGURE 4.30: Frontal view of the proposed design for the splitter between port 1 and 2.

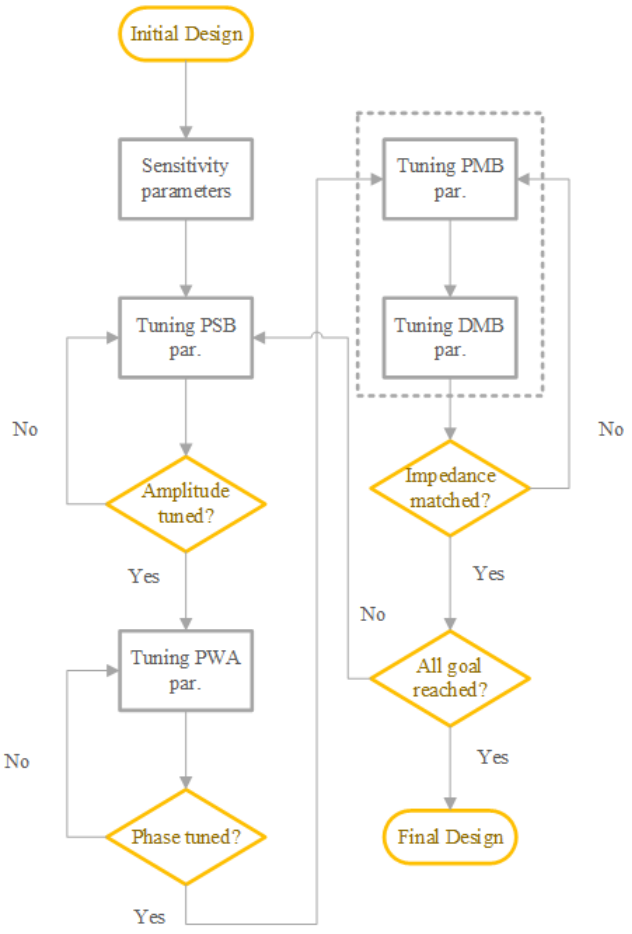

FIGURE 4.31: Flow chart of the tuning process for the proposed splitter.

The optimization of such device is not an easy task because it is an optimization with four variables and three goals. The first step of the design process is to sample the sensitivity of the parameters. After this preliminary step it is convenient to proceed with the tuning of the amplitude, afterwards the tuning of the phase and the last step is the impedance matching. This order arise from the consideration that the splitting bumps has a low impact on the phase tuning and impedance matching and the position of the WR90 arm has a low impact on the impedance matching. This procedure is shown on the flow chart, see fig. 4.31.

The sensitivity study is summarized in the figure from 4.32 to 4.34. These plots are in three groups of four figures with the variation of the three goals versus the four parameters defined. The device has been roughly tuned with the aid of some parametric sweep and then some more focused simulations have been done around these initial tuned values with a length span of ± 0.1 mm. The results have been fitted with linear or parabolic curves. The sensitivity of the PSB parameter for the amplitude difference is one order of magnitude greater of the other three parameters. Because of this it is convenient to fix this parameter at the beginning. For the phase difference the PSB and PWA values have a similar sensitivity (1.5 deg for 100 um). However the PSB value has been fixed from the previous step. The last figures show the sensitivity for the matching condition. In this case it is possible to tune the matching bumps dimension and position to achieve the required S_{11}.

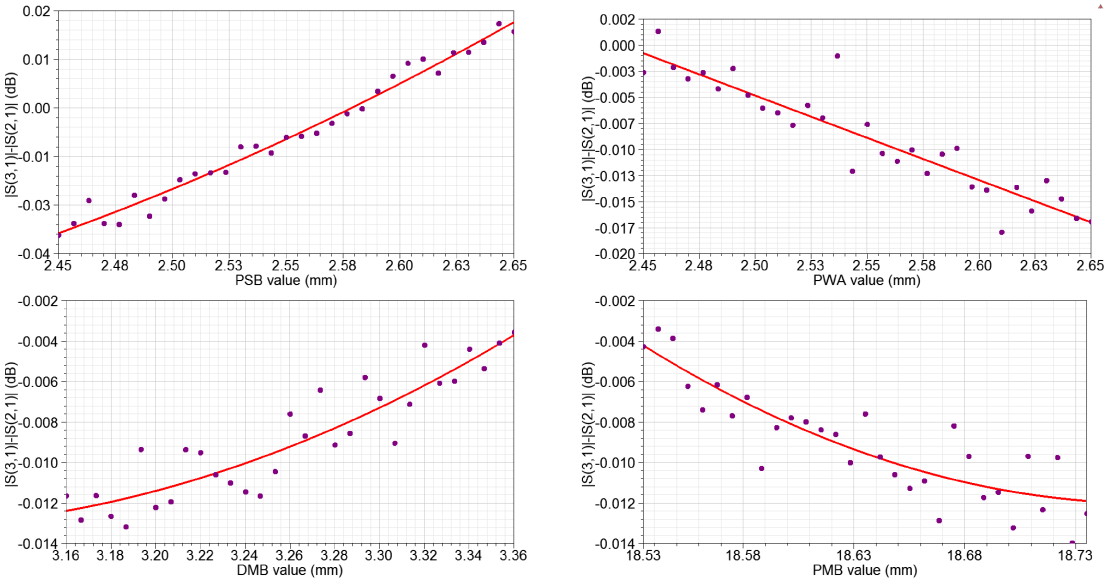

FIGURE 4.32: Sensitivity of the amplitude difference versus the PSB (top-left), PWA (top-right), DMB (bottom-left) and PMB (bottom-right) value.

The tuning of the splitter can be done iteratively until the desired value for phase and amplitude at the two port is reached. Usually two or three iterations are sufficient to reach the required design constraint. The optimized design has the following performance

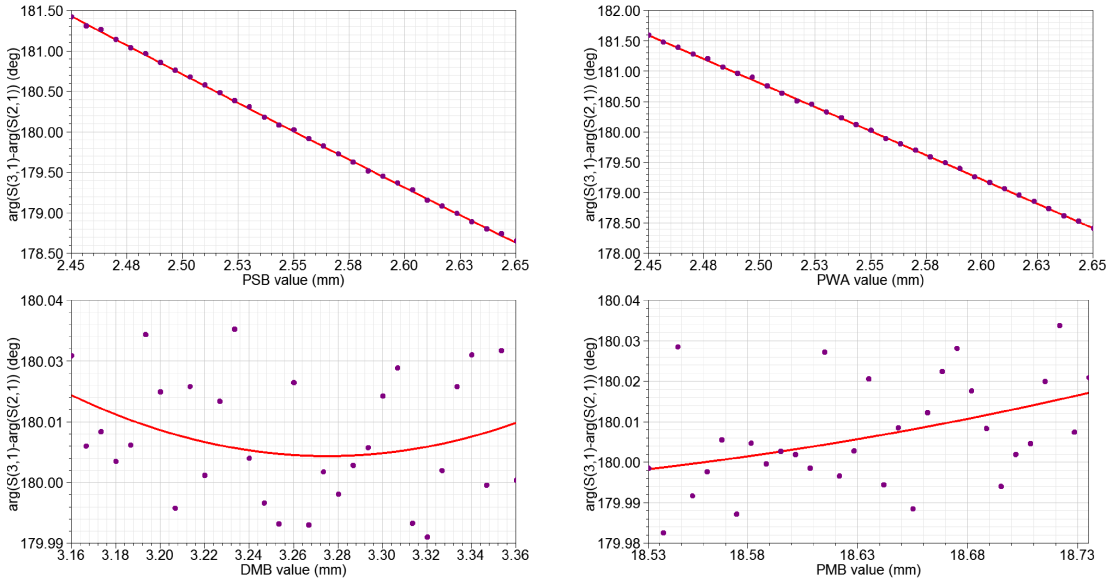

FIGURE 4.33: Sensitivity of the phase difference versus the PSB (top-left), PWA (top-right), DMB (bottom-left) and PMB (bottom-right) value.

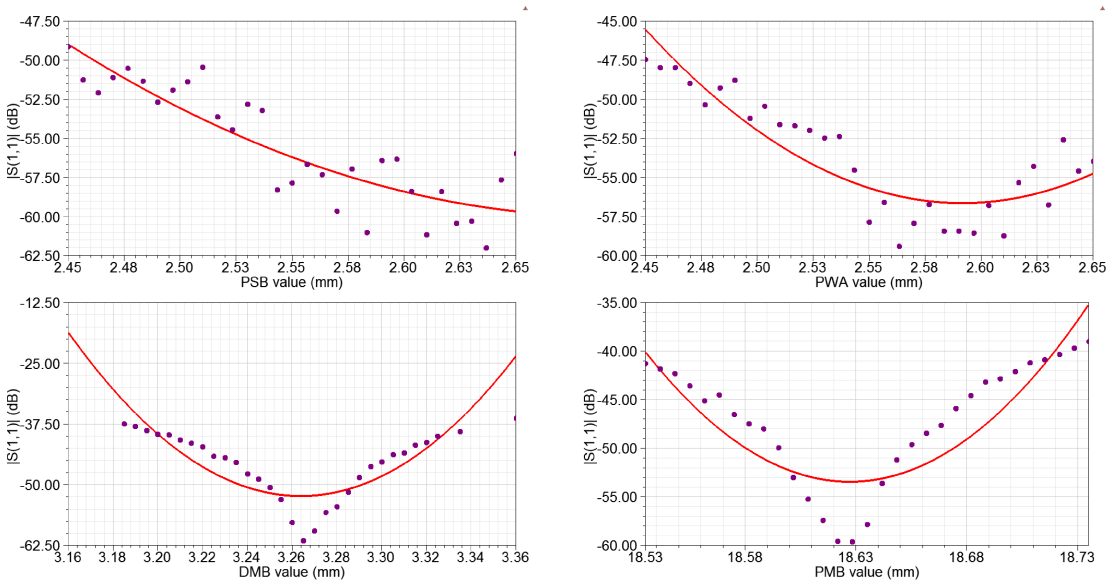

FIGURE 4.34: Sensitivity of the S_{11} versus the PSB (top-left), PWA (top-right), DMB (bottom-left) and PMB (bottom-right) value.

values $||S_{31}|-|S_{21}||=$ 0.0085 dB, $\angle S_{31} - \angle S_{21} = 180.017$ deg and $|S_{11}|= -57.98$ dB. The optimized parameters are PSB=2.55 mm, PWA=2.55 mm, DMB=3.26 mm and PMB=18.63 mm.

The whole splitter device has two devices like in fig. 4.30 and one like in fig. 4.35. The second device of the first type is added in order to feed the third and the fourth port of the PCAS but because the length needed to reach this two port is longer than the previous case this device is slightly different from the first. However the design process is the same of the first one. The last part of the splitter is a common 3dB splitter without

phase difference in order to feed the two splitters directly joined to the PCAS. However this splitter has to take into account the different design of the two splitters. In order to do this the position of the vertical section is not exactly in the middle and also the splitting bump has a little offset.

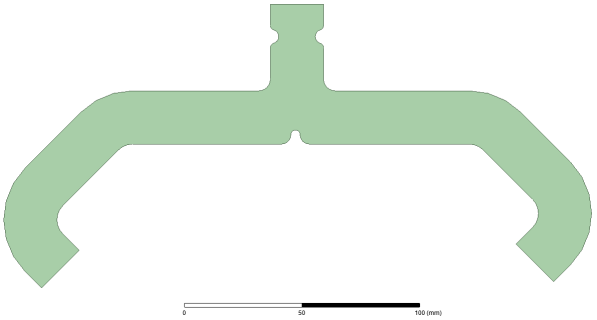

FIGURE 4.35: Frontal view of the top splitter.

The PCAS structure with the complete designed splitter and tapers has been simulated in order to evaluate the S_{11} parameter. The absolute value of S_{11} is -50 dB at the working frequency of 11.424 GHz, see fig. 4.37.

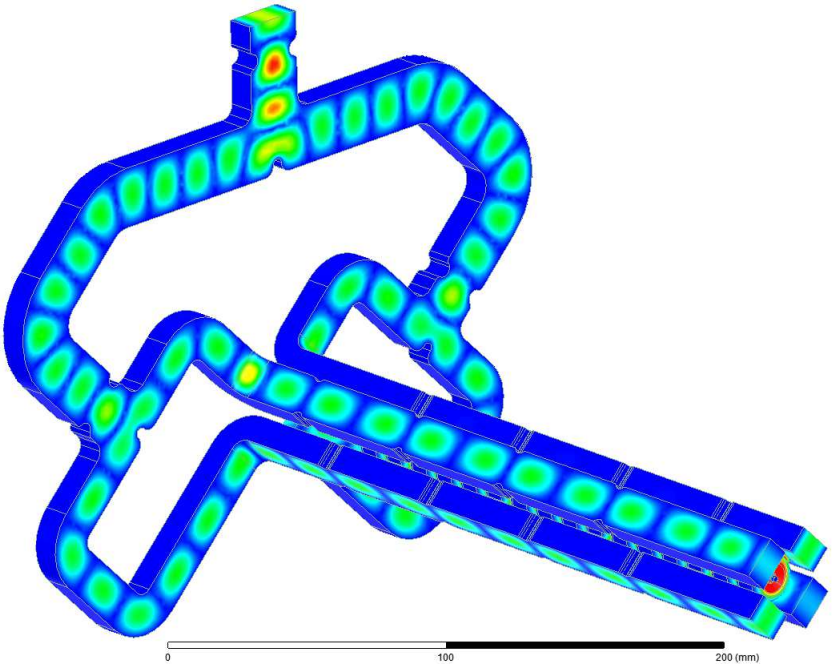

FIGURE 4.36: Plot of the electric field inside the structure with the complete design of the splitter and tapers.

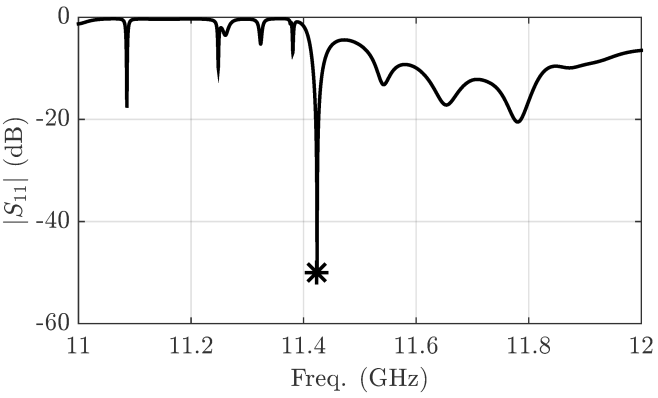

FIGURE 4.37: S_{11} versus frequency for the structure drawn in fig. 4.36.

4.9 Thermal Analysis

A thermal analysis has been conducted with Ansys Mechanical and Workbench in order to link the electrical project with the mechanical one. The surface magnetic field computed in the electrical project is imported as heat source for the thermal simulation. The heat dissipation is provided by four water pipes. The convective heat coefficient is and 1000 W/m^2 for heat transfer with the water pipes. The initial temperature of the copper is fixed to 22 °C.

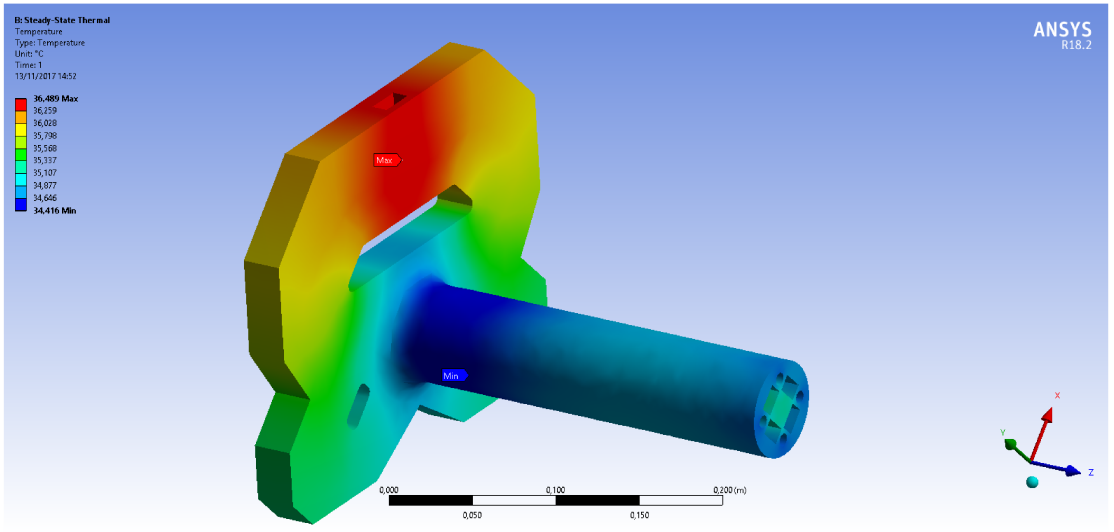

FIGURE 4.38: The thermal simulation with air heat transfer and water pipe gives a steady state temperature of roughly 35 °C. For the power branch network only the air convective dissipation has been used.

Taking into account a peak power of 150 MW, a pulse length of 200 ns and a repetition rate of 60 Hz, the deliver power in one second is equal to 1.8 kW. The steady

state temperature with the above conditions is equal to roughly 35 °C for the PCAS, see fig 4.38.

Chapter 5

Wakefield Analysis and Beam Alignment

5.1 Introduction

In this chapter wakefields and coupling impedances of the PCAS structure are investigated through time domain simulations. The long and short range wakefield can negatively affect the performance of the accelerator. In particular the longitudinal wakefield due to the beam loading effect can reduce the accelerating gradient [1, pp. 341]. As consequence of this for multi-bunch operation the energy gain is modulated along the z-axis. On the other hand the dipole modes may cause bunch instability due to the Beam Break-Up (BBU) effect [30]. The longitudinal wakefield and impedance analysis is of particular interest for multi bunch operation while for the single bunch operation the beam loading estimation is generally sufficient. In turn, the transverse wakefield calculations provide a quantitative analysis of the BBU-effect. The main sources of excitation of the dipole mode are beam deviation from the central orbit or a cavity design without a two fold symmetry, as for the PCAS proposed in the previous chapter. For PCAS the transverse wakefield can be severe because the radius of the iris is very small compared to the wavelength. Therefore the beam alignment to the structure should be carefully addressed. With the transverse wakefield results it is possible to provide an alignment tolerance for the beam.

Furthermore, an electromagnetic device for the position measurement of the particle bunch will be presented. These devices are called Beam Position Monitor (BPM). A simple analytical discussion for position measurement is developed. Time domain simulations have been used in order to design the BPM. Most common type of BPM are cavity, button and stripline. A stripline BPM has been chosen due to the simplicity of this type of BPM. Additionally, the BPM has been also characterized as charge measurement for the bunch. The simulations for this case have been compared with analytical

formulas and experimental results.

5.2 Time Domain Simulation of PCAS

An extensive analysis of the PCAS in the time domain has been carried out with CST Microwave Studio[1] software. For wakefield simulations, it is possible to use only a subset of the total number of cells. Indeed, from the definition and linearity of Maxwell equations, it is clear that for cells joined together by small radius irises, like the PCAS case, the wakefield results and the coupling impedance scale linearly with the number of cavities. In the general case the crosstalk between the cavities reduces the wakefield intensity and the linear scaling can be regarded as the upper limit [51], [52]. For PCAS the elementary unit is composed by four cells in order to consider at least one cell for each coupling direction, see fig 5.1.

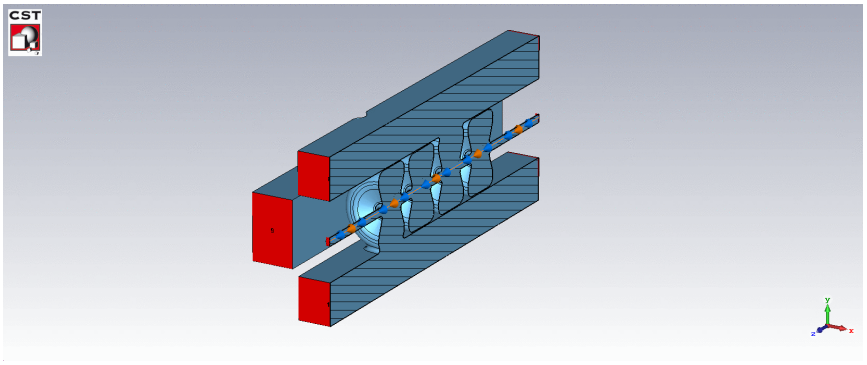

FIGURE 5.1: Model of the PCAS for wakefield simulations.

To avoid numerical instabilities the waveguides and the beam tube have been extended in the z-axis. Matched ports have been added to simulate an infinite waveguide length. The beam is modelled as a one dimensional line with no transverse dimension and a longitudinal length of σ_z=2 mm. The charge is 1 nC and the peak current is 60 A. However wakefield and coupling impedance results are generally normalized to 1 pC.

5.3 Longitudinal Wakefield and Impedance

If the beam propagates along the axis of a symmetric accelerating structure only the longitudinal wakefield component is excited. Although the PCAS is not exactly axis-symmetric the transverse wakefield are negligible when the beam propagate on axis. The longitudinal long range wake potential is shown in fig. 5.2. For a full period of the PCAS the maximum value of the longitudinal wakefield is 40 V/pC. Thus for a meter long structure in the linear scaling approximation the wakefield is roughly 750

[1] https://www.cst.com/

V/pC. The wakefields have been calculated for a wake-length of 10 meters (the bunch after propagates for 10 meters after exiting the simulated structure) in order to verify the exponential decaying. The conductivity of the copper has been used to include the resistive wall effect.

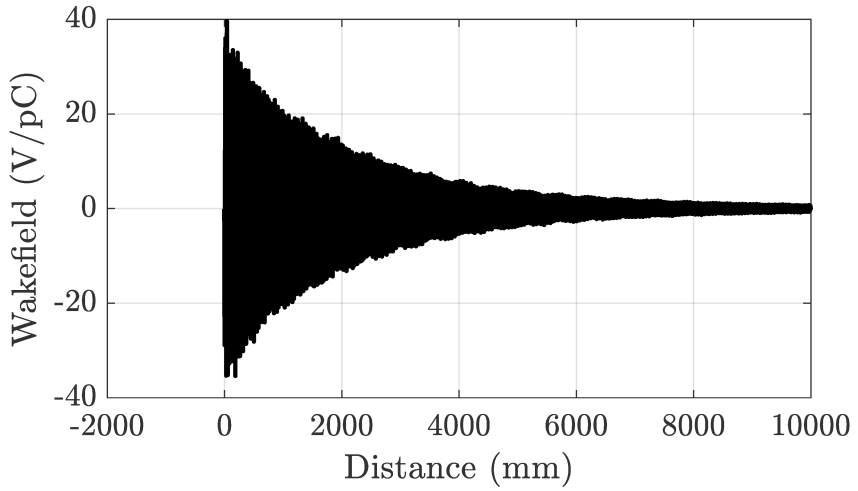

FIGURE 5.2: Longitudinal long range wakefield for the PCAS.

The Fourier transform of the wakefields gives the the coupling impedances of the PCAS, shown in fig. 5.3. The fundamental accelerating mode has a coupling impedance of roughly 90 kΩ. The resonant frequency is slightly different (tens of MHz) because for wakefield simulation hexaedral mesh is used. In this type of meshing the profile of the curved surfaces is badly discretized respect to the finite element method. For this effect (known in literature as staircase effect) the frequency simulation with tetrahedral mesh is more accurate.

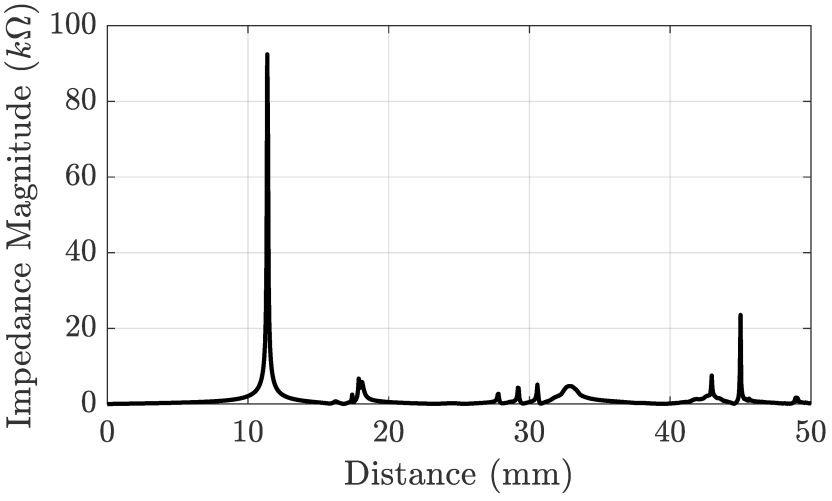

FIGURE 5.3: Coupling impedance for the PCAS.

The first other longitudinal mode coupled has a resonant frequency of roughly 18 GHz. The coupling impedance is ∼5700 Ω.

5.3.1 Loss Factor

The lost energy of a bunch passing inside a structure is the product of the loss factor and the squared value of the charge with negative sign. For PCAS the loss factor is roughly 20 V/pC for a gaussian beam with σ_z=2 mm. Thus the average energy lost for a 100 pC and 1 nC bunch is 200 nJ and 20 mJ, respectively. In eV it is equal to 2 KeV for the 100 pC bunch and 20 KeV for 1 nC. Because the energy gain in four cell is roughly 4 MeV the single bunch beam loading effect is negligible even for 1 nC bunch.

The z component of the electric field, i.e. the accelerating (or decelerating) mode, generated by the transit of 1 nC inside the four cell PCAS is shown in figure 5.4. In the blue region the electric field is decelerating and the position of the bunch is roughly at the beginning of the fourth cell from the right to left.

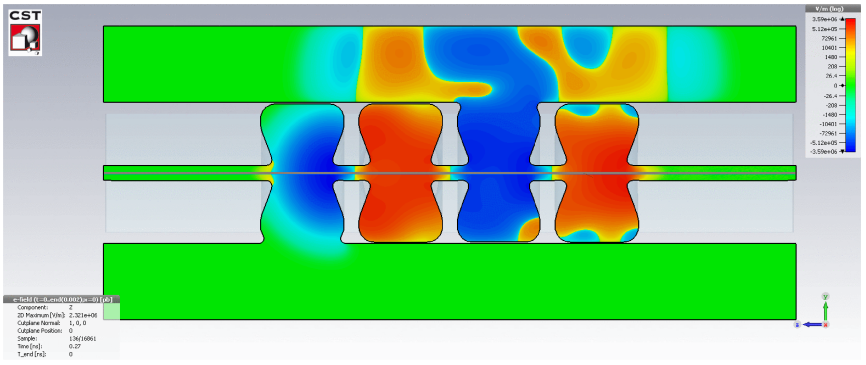

FIGURE 5.4: Electric field, z component, in PCAS for a 1 nC with σ_z=2 mm.

The on axis field and the position of the bunch are shown in fig. 5.5. For a charge of 1 nC the accelerating gradient is reduced by 2 MV/m.

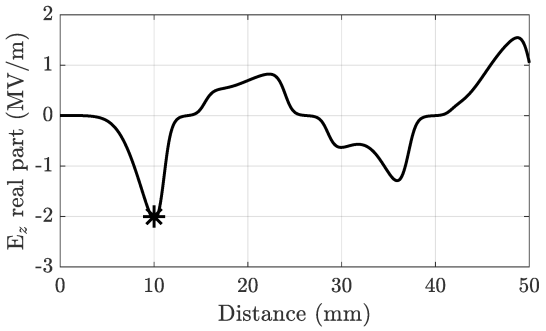

FIGURE 5.5: On axis field of the figure 5.4. The mass centre of the beam is indicated with an asterisk.

5.4 Transverse Wakefield and Impedance

The value of the transverse wakefield should be kept as low as possible. A large value of it can lead to destructive instability phenomena like the BBU effect. For a linear collider a recommended value is of 1 V/pC/mm/m for short range transverse wakefield [46]. However for a shorter LINAC a larger value can be tolerated. For the four cell PCAS of figure 5.1 a value of 5 and 2.5 V/pC/mm has been found and because this small section is roughly 50 mm the wakefield per unit length is respectively 100 and 50 V/pC/mm/m. This value, as it can be seen in the next paragraph, can limit the maximum number of accelerating sections before reaching a critical displacement.

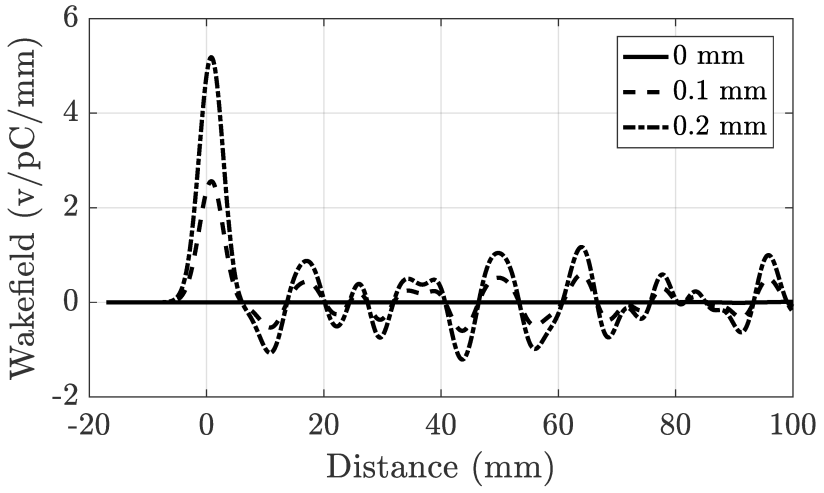

FIGURE 5.6: Short range transverse wakefield for beam with 100 and 200 μm displacement from axis.

The magnitude of the transverse coupling impedance are presented in figure 5.7 for an offset of 200 μm. The beam has a displacement from the axis only in the Y plane and thus in the X axis there is a negligible transverse coupling. The coupling impedance is roughly 4 kΩ. The ratio of the longitudinal impedance and the transverse one is $\sim$22. Due to the linearity of Fourier transform also the coupling impedance has a linear scaling respect to the number of cells.

The lowest dipole mode has a resonant frequency (f_r) of 19.864 GHz and the half-height bandwidth (Δf) of 68 MHz. It is well known that the quality factor is:

$$Q_0 = \frac{f_r}{\Delta f} \tag{5.1}$$

which for the elementary cell of fig. 5.1 leads to a quality factor of 280.

The kick factor for a displacement of 200 μm is 0.43 mV/pC/mm for the section with four cells.

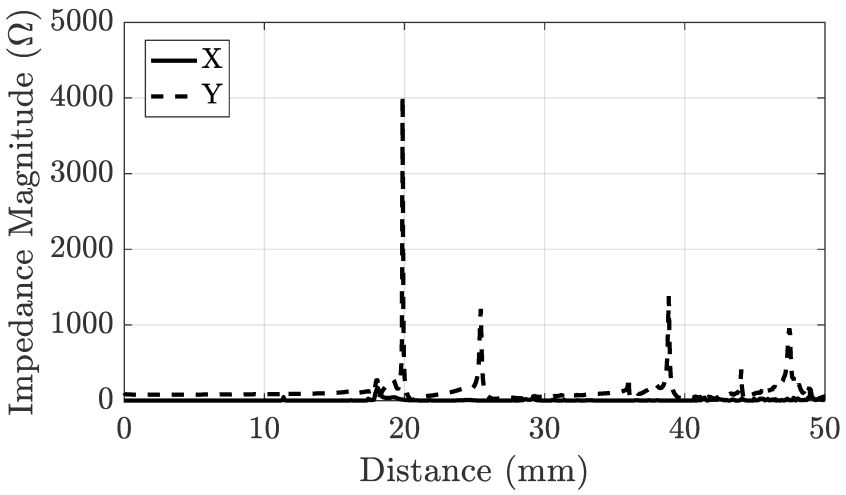

FIGURE 5.7: Transverse coupling impedance (in both X and Y axis) for the 200 μm off axis displacement.

5.4.1 BBU Instability

The single bunch beam break-up instabilities can be evaluated with equation 2.4:

$$\left|\frac{\Delta x}{x_1}\right| = \frac{Q_t e}{2G} W_\perp(2\sigma_z)\beta_m \ln\frac{\gamma(z_f)}{\gamma_0} \tag{5.2}$$

where the wakefield must be in V/C/m^2 unit and the accelerating gradient in MeV [29, sect. 2.4]. Two cases for bunch charge have been considered, 100 pC and 1 nC. The average gradient is equal to 80 MeV/m. The betatron function β_m can be roughly evaluated[2] as 10 mm. The initial energy can assumed equal to 100 MeV. With these values and for a short-range transverse wakefield of 5 V/pC/mm the displacement is in the order of magnitude of the nano-meters, see fig. 5.8.

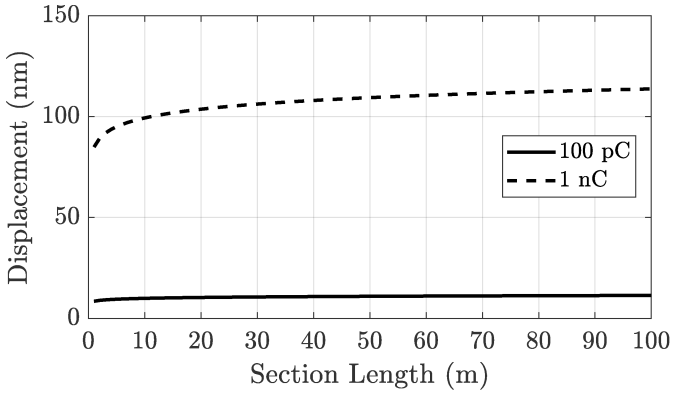

FIGURE 5.8: Displacement due to the BBU effect vs. the length of LINAC.

[2]The β_m function is approximatively equal to $\beta_m = \sigma^2/\epsilon$.

For the worst case of 1 nC of charge after 100 meters of propagation the displacement is 120 nm. Therefore, for the PCAS, the dipole field components have a greater effect on the misalignment of the bunch (see B for beam dynamics analysis).

5.5 Beam Alignment and Position Measurement

From the results of the previous chapter it is clear that the bunch should propagate in the axis of the accelerating sections in order to avoid deflection from the dipole mode and the BBU effect. An off axis position of the beam may arise from several causes. The most common are [30]:

- beam injected off axis
- misalignment of the accelerating sections
- misalignment of the magnetic lens

The second and the third points are avoided by a careful positioning of the LINAC elements along the beam line. To avoid instead the an off axis injection it is possible to measure the position of the bunch and correct it with dedicated electrostatic or magnetic correctors [53]. The employed device for the measurement of the bunch coordinates is called beam position monitor (BPM). They are non-destructive beam diagnostic tools used in accelerators operating with bunched beams. They are based on the possibility of measuring the charge induced by the beam passage on insulated metal plates or the intensity of the dipole modes excited by an off-axis beam. In the formalism of the BPMs a transfer impedance Z_t function of ω is defined.

Various designs are possible, the most common for short electron bunch are cavity, button and stripline BPMs [54] [55]. In the cavity BPM dipole modes are excited by a misaligned beam. A simple cavity without external excitation is designed and a probe for measurement of the intensity of the dipole mode is inserted, which is typically a coaxial cable with a small portion of the inner conductor inside the cavity [56]. The excitation of the dipole mode is proportional to beam misalignment for small value near the axis, see equation (2.5). In the button type BPM a metal ring is inserted in the pipe and it is capacitively coupled to the beam current. Instead, in the stripline BPM a straight metal plate is used and it is normally longer than the bunch longitudinal dimension. The main advantage of the stripline BPM against the other types is the possibility of measuring time signals with high resolution and in the case of a circular collider it is also possible to identify the propagation direction of the bunch. However stripline BPMs are harder to manufacture and they have a lesser position resolution respect to the cavity type. In any case a position resolution of 1 μm is achievable [57]. These performance are sufficient for the PCAS design requirements.

5.6 Theory for Strip-Line BPM

A schematic view of a BPM stripline monitor is shown in fig. 5.9. Four striplines azimuthally spaced of 90 degree are placed inside a pipe. They have length l and the space between them and the pipe is g. The width of the strip and the spacing g are designed to obtain a characteristic impedance of 50 Ω. By this way the coaxial cable is matched and signal reflections between stripline and cable are avoided. The port 1 is connected to the read-out electronics. The other termination is shorted (port2).

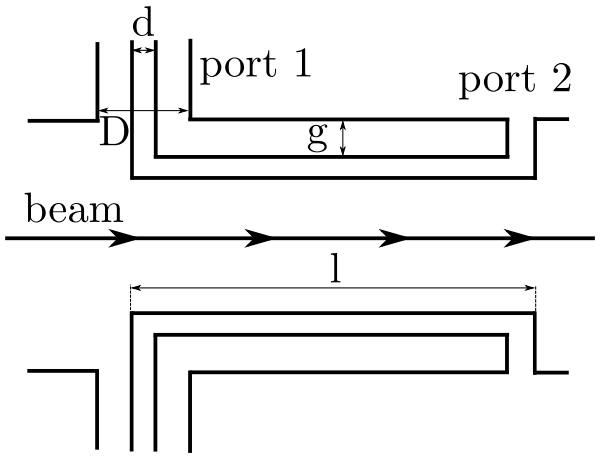

FIGURE 5.9: Schematic view of the stripline BPM.

The beam while propagating from left to right induces an image charge on the stripline. Half of this signal is delivered to the port one and the remaining part travel towards the shorted port. After a time $t = l/v$ the signal is reflected from the shorted end with changed sign and it is added to signal of the leaving bunch, which has a double amplitude of the co-propagating one. The result is a counter-propagating signal with the original signal strength. In an ideal behaviour this counter-propagating signal should add to the signal of the following bunch of the macro-pulse train. If the bunch spacing and the velocity of the particles are known it is possible to find the optimal length to obtain this response from the device. In a BPM the voltage signal is proportional to the beam current and characterized by the transfer impedance $Z_t(\omega)$, giving in the frequency domain:

$$V_s(\omega) = Z_t(\omega) I_{beam}(\omega) \tag{5.3}$$

The $V_s(t)$ voltage signal is generated by the direct image current combined with the current reflected from the shorted port:

$$V(t) = \frac{Z_{strip}}{2}\frac{\alpha_c}{2\pi}[(I_{beam}(t) - I_{beam}(t - l\zeta))] \tag{5.4}$$

where Z_{strip} is the characteristic impedance of the stripline, α_c is the angular coverage of the single stripline and $\zeta = 1/c + 1/v_0$ where c is the speed of light and v_0 is the beam velocity. The temporal gaussian profile in the time domain is equal to [58]:

$$I_{beam}(t) = I_0 e^{-\frac{t^2}{2\sigma_t^2}} \tag{5.5}$$

substituting the above equation in 5.4 it is found the signal voltage:

$$V_s(t) = \frac{Z_{strip}}{2}\frac{\alpha_c}{2\pi} I_0 \left(e^{-\frac{t^2}{2\sigma_t^2}} - e^{-\frac{(t-l\zeta)^2}{2\sigma_t^2}} \right) \tag{5.6}$$

the Fourier transform of this function can be analytically found [59]:

$$|Z_t(\omega)| = \frac{Z_{strip}}{2}\frac{\alpha}{2\pi} e^{-\frac{\omega^2\sigma_t^2}{2}} \sin\left[\frac{\omega l}{2}\left(\frac{1}{c} + \frac{1}{v_{beam}}\right)\right] \tag{5.7}$$

where $\omega = 2\pi f$ with f is the bunch frequency. The transfer impedance is maximized when:

$$l_{opt} = \frac{\lambda}{2}\frac{\beta}{1+\beta} \tag{5.8}$$

with $\beta = \frac{v_0}{c}$. For electron linac it is reasonable to approximate $\beta \approx 1$ for every practical case, leading to $l_{opt} = \frac{\lambda}{4}$. The magnitude of transfer impedance, $|Z_t(\omega)|$, has a series of maxima for:

$$f_{max} = \frac{c}{4l}(2n-1) \text{ for } n = 1, 2, ... \tag{5.9}$$

if the choice $n = 1$ is used the BPM is working in the first harmonic mode, for $n = 2$ in the second and so on.

5.7 Simulation of the Device

As an example of a stripline BPMs the devices of the ELI_NP project [5] have been considered. Stripline BPMs will be installed along the beam path in order to measure the position of bunches. Each BPM has an approximate length of 235 mm and is composed by four steel electrodes with an angular width of 26 deg. The distance from the beam pipe is 2 mm and they have a width of 7.7 mm, see fig. 5.10. The impedance of the transmission line created by the the electrode and the pipe chamber is roughly 50 Ω. The acceptance of the BPM is 34 mm. A further BPM with an acceptance diameter of 100 mm will be installed on the dump line after the low energy interaction point [60].

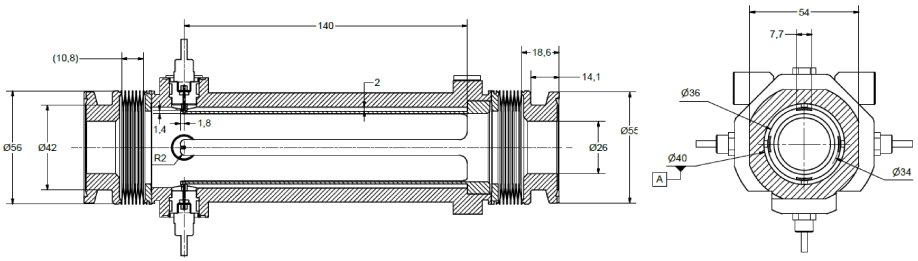

FIGURE 5.10: Mechanical drawing of the ELI_NP BPM.

The device has been simulated with CST Microwave Suite with the wakefield solver, see fig. 5.11. A bunch with a charge of 250 pC and σ_z of 2.5 mm is considered. The beam passing inside the device induces an image current which propagates in the four coaxial cables. At the end of them a waveport is added to allow the power to flow outside. Four voltage monitors record the signals at the output cables. These signals will be used in the post processing stage to find the performance of the simulated device.

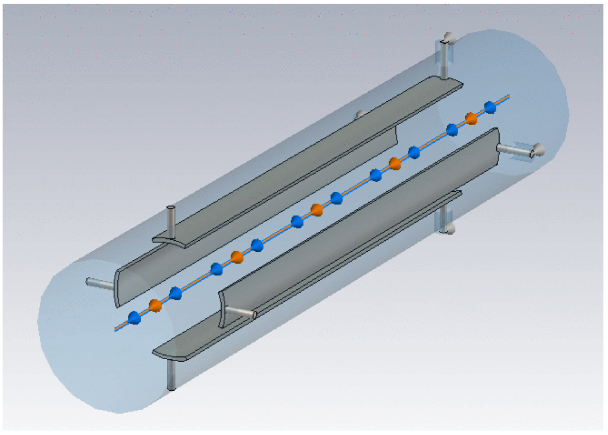

FIGURE 5.11: CAD design of the stripline BPM used for the simulation.

Four voltage monitors record the signals at the output cables, see fig.5.12. These signals will be used in the post processing stage to find the performance of the simulated device. The position of the beam is parametrically changed to obtain the voltages for all ports for each position. Due to the symmetry of the device only one eight of the position are necessary to fully calibrate the BPM. The simulation was performed with the beam in different position over an area of 7 mm $\times$ 7 mm with 0.5 mm step, for a total of 841 points. Thanks to the geometrical symmetry[3] of the device only an eight of these points should be simulated, i.e the points inside the region bounded by the curves $y = 0$, $y = x$ and $x = 7$ mm. The remaining points can be found with a simple post processing operation.

[3]In general, symmetry planes cannot be used in the simulations but for the points over the $y = 0$ line.

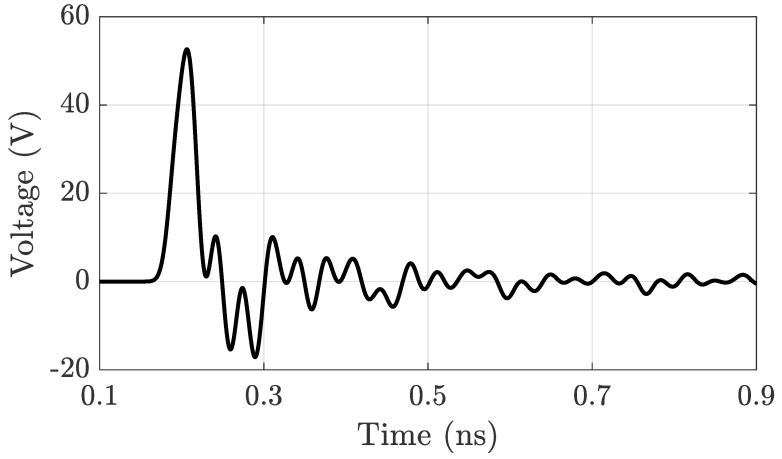

FIGURE 5.12: Voltage signal obtained at the output port.

5.8 Position Measurement

The position measurement on the x axis can be obtained, after a calibration of the device, with the difference over sum method. The position is proportional to this ratio:

$$x_{pos} = \frac{1}{S_x}\frac{V_1 - V_3}{V_1 + V_3} + \delta_x \tag{5.10}$$

where V_1 and V_3 are the voltages at the horizontal pick-up (left and right), δ_x an offset correction, and S_x is the position sensitivity. It is the proportional constant between the beam displacement and the signal strength [58]:

$$S_x = \frac{d}{dx}\left(\frac{V_1 - V_3}{V_1 + V_3}\right) = \frac{d}{dx}\left(\frac{\Delta V_x}{\sum V_x}\right) \tag{5.11}$$

where $\Delta V_x = V_1 - V_3$ and $\sum V_x = V_1 + V_3$. The position sensitivity is measured in mm^{-1}. For small value of the displacement a constant value is expected due to the linearity of the device. In general sensitivity is a function of the vertical and horizontal position. Equivalent definitions for the y axis are:

$$y_{pos} = \frac{1}{S_y}\frac{V_2 - V_4}{V_2 + V_4} + \delta_y \tag{5.12}$$

and

$$S_y = \frac{d}{dy}\left(\frac{V_2 - V_4}{V_2 + V_4}\right) = \frac{d}{dy}\left(\frac{\Delta V_y}{\sum V_y}\right) \tag{5.13}$$

where V_2 and V_4 are instead the voltages at the vertical pick-up (up and down).

The absolute value of the ΔV_x and ΔV_y are meaningless in the simplified scenario of a simulation because the absolute value of the single voltage signals are function of the beam but also of the read-out electronics, attenuation on cables and others factors which

are not accounted in these simulations. Thus, in the following the normalized quantities of ΔV_x and ΔV_y are considered.

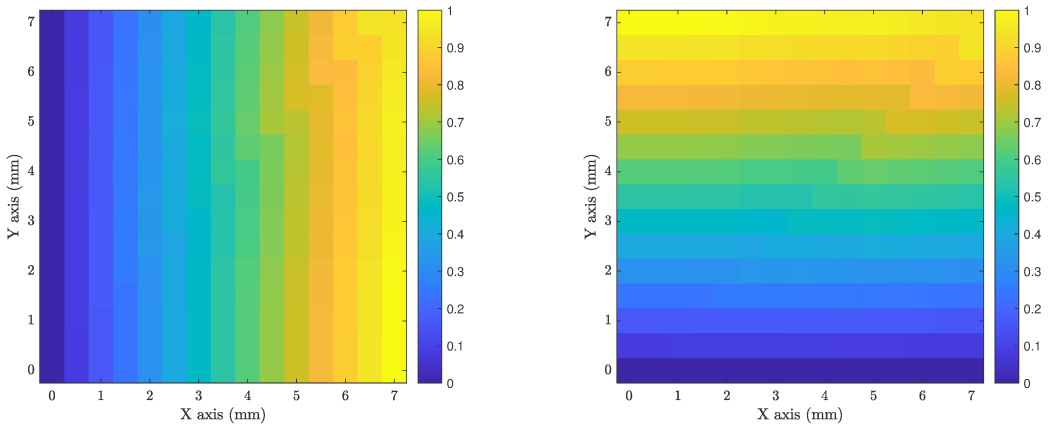

FIGURE 5.13: Map of the normalized values of ΔV_x (left) and ΔV_y (right).

The maps of the normalized values of ΔV_x and ΔV_y are shown in fig. 5.13. As expected the minimum value is in the origin of the map, i.e. when the beam is on axis, and the maximum for the most displaced position, $x_{pos} = y_{pos} = 7$ mm. The normalized value of ΔV_x for the x axis is plotted in fig. 5.14. A linear fit has been found for ΔV_x in order to find the position sensitivity for the x-axis, see fig. 5.15.

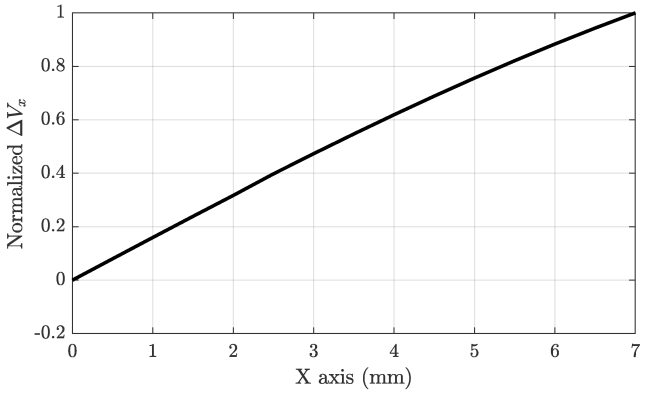

FIGURE 5.14: Normalized ΔV_x vs. the x axis.

The linear equation of the fit is:

$$f(x) = p_1 \cdot x + p_0 \tag{5.14}$$

and for this case it is found $p_1 = 0.1441$ and $p_0 = 0.024$. From the comparison of equations (5.10) and (5.14) it is clear that the normalized value of position sensitivity is:

$$S_x = \frac{1}{p_1} = 6.939 \tag{5.15}$$

and the position offset is:

$$\delta_x = p_0 = 0.024 \tag{5.16}$$

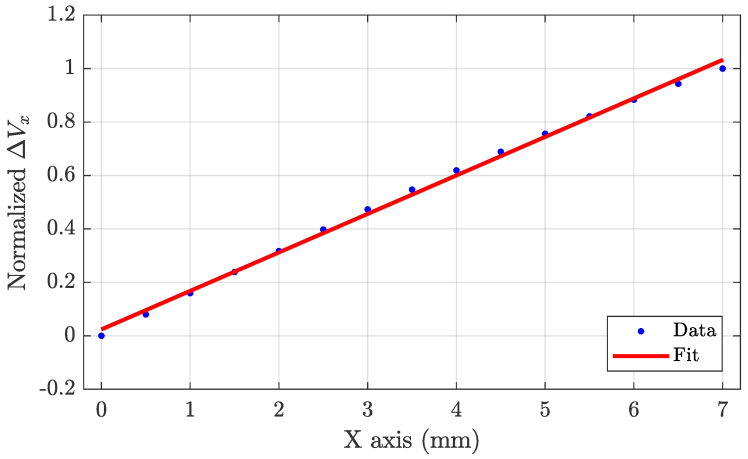

FIGURE 5.15: Linear fit of the normalized ΔV_x vs. the x axis.

The normalized value of S_x is constant in the y-axis, see fig. 5.16. The curve variation is in the order of tens of μm. This noise value for ΔV_x is introduced by the numerical error of the simulator.

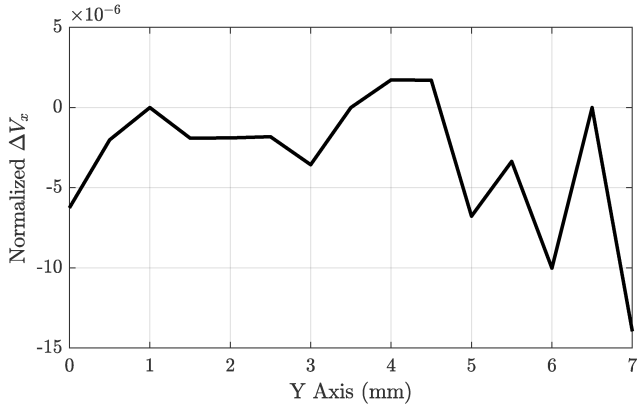

FIGURE 5.16: Normalized ΔV_x vs. the y axis.

For sake of completeness also the plots of ΔV_y are shown, see fig. 5.17. However due to the symmetry of the device they are the dual case of ΔV_x with the role of the x and y axes swapped.

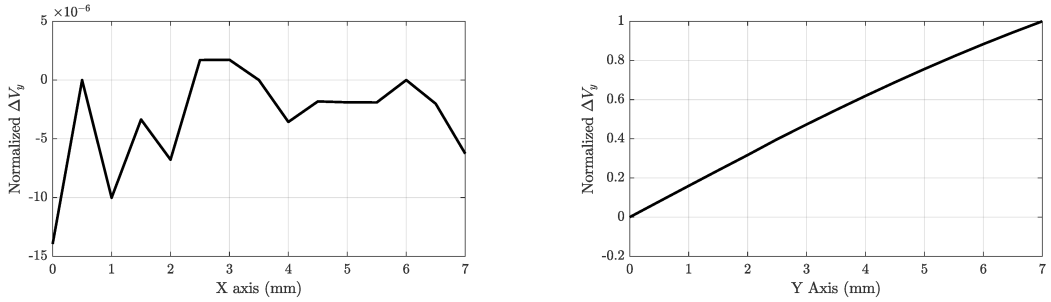

FIGURE 5.17: Normalized ΔV_y vs. the x axis (left) and y axis (right).

5.9 Charge Measurement

The BPMs already studied can be also used for charge measurement in addition to the specific devices [61]. The measurement of the bunch charge is proportional to the sum of the four voltage signals from the output ports of the BPM. However, due to the non linear behaviour of the pick-up devices, a calibration curve should be applied to the readings. A full characterization of the voltage signals picked from the output port of the BPMs has been done by means of an analytical model and with full 3D simulations. A simple analytical model has been developed in order to compare the simulation results. The wall density current induced in the stripline is equal to [58]:

$$j_{im}(\phi) = \frac{I_{beam}}{2\pi a} \cdot \frac{a^2 - r^2}{a^2 + r^2 - 2ar\cos(\phi - \alpha_c)} \tag{5.17}$$

where I_{beam} is the current of the beam, a is the distance of the stripline from the centre of beam line, α_c is the angular coverage and r, ϕ are the polar coordinates. The current delivered to the coaxial cable can be found with an integration over the coverage angle of the stripline:

$$I_{im} = \int_{-\alpha_c \backslash 2}^{\alpha_c \backslash 2} a \cdot j_{im}(\phi) d\phi \tag{5.18}$$

The voltage signal at the output port is proportional to the current therefore the calculation of the impedance of the coaxial cable is not necessary for the comparison of the normalized curves.

The measurements have been carried out at ALBA with the wire stretching method [62]. The test bench setup is shown in fig. 5.18.

The results are summarized and compared with the measurements in fig. 5.19. The curves in the three analysed cases (analytical model, simulations and measurements) have been evaluated over a grid of 841 points with 29 points for both horizontal and vertical axis, as for the position measurement. The points are in the span length of ± 7

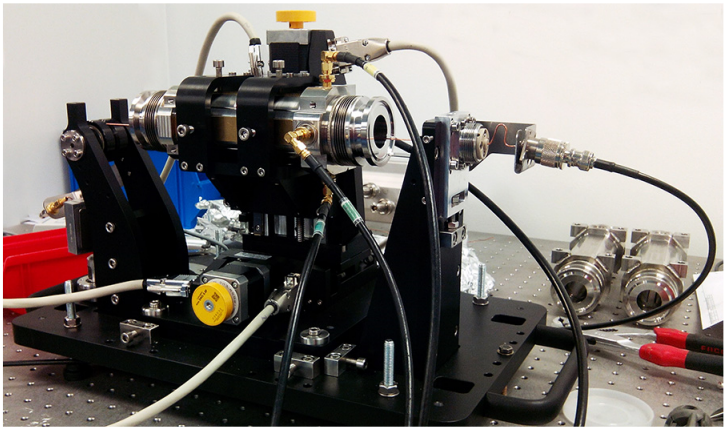

FIGURE 5.18: Test bench for the measurement of the charge. Courtesy of ALBA-CELLS.

mm around the centre with a fixed step of 0.5 mm. The traces have been normalized to the central value of the grid, which is the reference value.

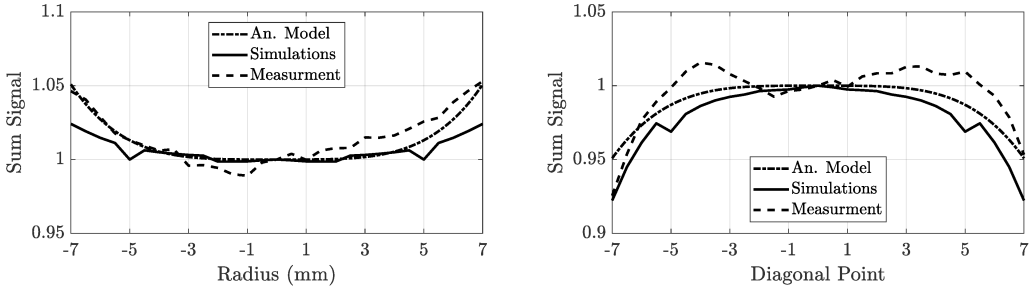

FIGURE 5.19: Sum of the voltage signals from the four ports versus the x axis (top plot) and the diagonal line, $y = x$ (bottom plot).

In order to use the full BPM acceptance of ± 7 mm area a correction algorithm based on a polynomial fit of the curve is here developed. The correction algorithm for the charge reading will be implemented as a high-level application within the control system. This algorithm has been enforced only for the simulation results (validated by the analytical model) and measurement readings.

A polynomial function of the x and y position of the fourth grade is adopted:

$$\begin{aligned} f(x,y) = {} & a_{00} + a_{10}x + a_{01}y + a_{20}x^2 + a_{11}xy + a_{02}xy^2 + a_{30}x^3 + a_{21}x^2y \\ & + a_{12}xy^2 + a_{03}y^3 + a_{40}x^4 + a_{31}x^3y + a_{22}x^2y^2 + a_{13}xy^3 + a_{04}y^4 \end{aligned} \tag{5.19}$$

therefore a total number of 15 coefficients, for both simulation and experimental case, are necessary in order to full characterize the fit equations. The obtained coefficients are listed in the table 5.1.

TABLE 5.1: Polynomial fit coefficients.

Index	Coeff.	Sim.	Meas.
1	a_{00}	+1.00709	+9.88728e-01
2	a_{10}	+1.85821e-17	+1.52370e-03
3	a_{01}	+3.34763e-19	+1.29374e-03
4	a_{20}	-2.34095e-04	+5.84219e-04
5	a_{11}	-4.13974e-18	-5.49711e-04
6	a_{02}	-2.34095e-04	+7.27711e-04
7	a_{30}	-9.08888e-19	-3.05091e-05
8	a_{21}	-4.04803e-20	-1.23042e-05
9	a_{12}	+6.13145e-20	+5.54398e-05
10	a_{03}	-1.57277e-19	+1.20780e-05
11	a_{40}	+1.43842e-05	+1.03114e-05
12	a_{31}	+5.56406e-20	+2.17884e-06
13	a_{22}	-5.04218e-05	-7.80406e-05
14	a_{13}	+7.96769e-20	+4.19682e-06
15	a_{04}	+1.43842e-05	+1.18798e-05

Because of the parabolic behaviour of the non-linearities the most important coefficients are a_{20} and a_{02} which are in great agreement between simulations and experimental results. The linear terms, a_{10} and a_{01}, are not zero in the measurement fit because of the geometrical imperfection of the realized BPM and/or for the different gain level of the four channel of the electronic read-out. This dependency from the linear terms is not captured by the simulation already done. The mixed terms (a_{ij} for $i, j \neq 0$), with the exception of a_{22} coefficient, are nearly zero in the simulation results. Nevertheless, in the measurement fit, they are one or two order of magnitude lower of the a_{20} and a_{02} terms due to the linear dependence from x and y.

The polynomial surface and the points for the fit are shown in fig. 5.20. The R-squared coefficient for the simulation fit is 96.95% and for the experimental data is 98.10%.

The difference between the two fitted surface equations is shown in the fig. 5.21. A very good agreement between the two fit equations is found. In the full acceptance area of 196 mm^2 the maximum error is equal to 5.4%. The main sources of errors are the different values of the channel gain of the read-out electronics and the mechanical fabrications errors.

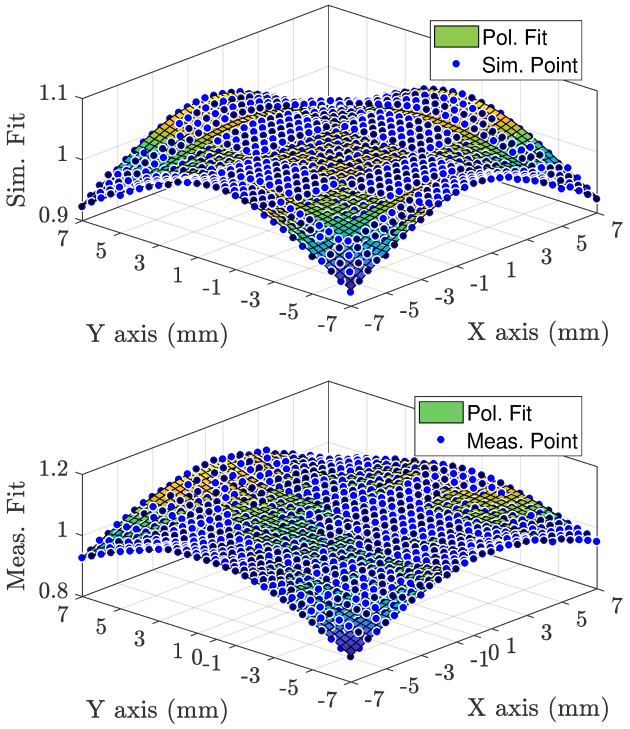

FIGURE 5.20: Polynomial fitting for the simulation results (top plot) and measurement data points (bottom plot).

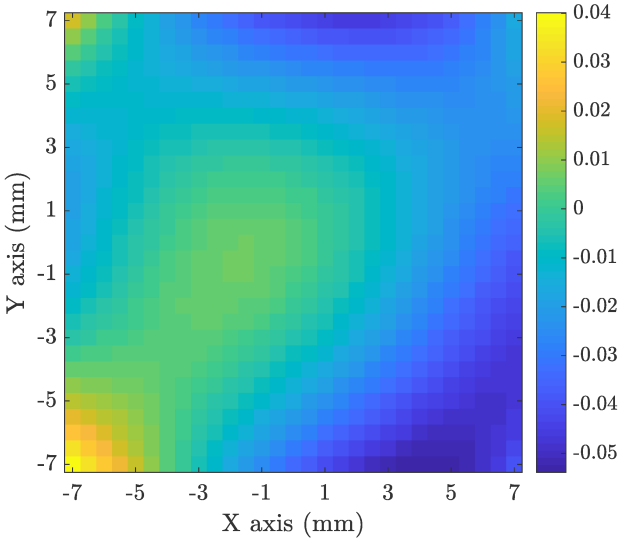

FIGURE 5.21: Difference between the two fitted surface equations.

Conclusions

The design of a Parallel Coupled Accelerating Structure (PCAS) is reported in this thesis. The newly proposed configuration has been compared with previous PCAS solutions and the main differences have been discussed. The phase velocity and the speed of the particles are matched with an innovative and simple scheme for efficient acceleration. The shape, both for the 2D and 3D profile, of the cells has been optimised for high gradient operation according to the most recent advancement on this field. The main RF parameters of the proposed PCAS are summarized in table 4.10, which is also reported here for ease of readiness:

RF parameters of the 3D cell. Maximum temperature rise for PCAS is calculated for pulse length of 200 ns.

Parameters	Clic-G T24	RDDS1	Parallel Coupling
Structure type	Const. gradient	Const. gradient	Const. impedance
Length (m)	0.3	1.8	2
Phase Adv.	$2\pi/3$	$2\pi/3$	π
Unloaded gradient (MV/m)	100	50	80
Input/Output radii (mm)	3.15/2.35	5.605/3.885	1.00
a/λ	0.12	0.18	0.038
Group velocity (v_g/c)	0.018/0.009	0.11/0.03	0.09
Attenuation, τ_0	1.88	0.48	0.33
Quality factor	∼5600	∼7800	∼8200
Shunt impedance (MΩ/m)	116/150	77/100	161
R over Q (Ω)	26700	12800	19600
Peak Input Power (MW)	75	82	152
Filling time (ns)	57	104	75
Maximum E-Field (MV/m)	222	∼350	272
Max. mod. Poynting vector	3.51	∼20	3.99
Pulse heating rise	14	∼90	42

The section proposed is an equivalent constant impedance for axis coupling with a π phase advancement. Due to the small aperture the shunt impedance is very high and constant all along the section. The high gradient figures of merit, maximum sustained surface electric field, modified Poynting vector and pulse heating rise, are in the safe limits for an accelerating gradient of 80 MV/m and a pulse length of 200 ns. The main parameter that allow to control the phase and group velocity in the proposed structure

are indicated both on a physical ground and by full wave parametric simulations on a single period of the structure. An innovative resonant coupling scheme has been employed for structure stabilization. In the proposed structure a large group velocity (9% of c) is obtained in the confluence point. This value is appropriate for the development of an accelerating section few meters long, operating in the X-band.

Due to the single coupling hole a dipole kick is expected. In order to quantify the kick a beam dynamics analysis has been conducted. The position of the cooling tubes has been investigated by numerical results with the aid of the multi-physics suite of ANSYS. The steady state temperature is 35 °C for a 150 MW RF pulse with repetition rate of 60 Hz and duration of 200 ns and an environment temperature of 22 °C.

The presence of a such small iris can be source of strong wakefield for misaligned bunch. Therefore, the PCAS has been also studied in the time domain in order to evaluate this effect. For an offset of 200 μm the transverse wakefield is 100 V/pC/mm/m. Thus, the maximum sustainable current and length of the accelerating section is found to avoid instabilities. For a bunch charge of 1 nC and *rms* length of 2 mm the cumulated offset after 100 meters of accelerating sections is 0.1 μm due to the BBU instability, which is three order of magnitude fewer of the dipole kick. Because of these critical points the offset measurement of the beam has been studied through a stripline BPM. This device is used in the ELI_NP facility. The position sensitivity has been found by numerical means. The possibility of a charge measurement of the bunch through a stripline BPM has been investigated. The calibration curve obtained through numerical analysis is in good agreement with the experimental results.

Appendix A

EM Software Design Automation

The design and tuning of accelerating structure, and in general of RF devices, requires EM commercial software like Ansys HFSS[1] or CST Microwave Studio[2]. These tools have a lot of capabilities for CAD design parametrization, optimization and post-processing. However, for very complex structures, some design steps can be very repetitive and tedious to accomplish. For example a constant gradient structure needs the design of a large number of cells with same dimensions but different irises and cell radius. This task can be very time consuming and source of errors. Fortunately, the design of these cells can be automatized with a *for-like* iteration because it is a simple operation with minor differences at every step. In order to define this *for-like* iteration the EM software should be used together with a programmable language, like MatLab[3]. The integration of HFSS and MatLab in an unique framework trough the Object Linking and Embedding (OLE) automation is briefly explained in this appendix.

A.1 OLE Automation

OLE Automation is an inter-process communication mechanism which makes it possible for one application to manipulate objects implemented in another application, or to expose objects so they can be manipulated. It is based on a subset of Component Object Model (COM) that was intended for use by scripting languages, originally Visual Basic for Application, but now is used by several languages on Windows (C, C++, Python, Java, ...). An Automation server is an application (a type of COM server) that exposes its functionality through COM interfaces to other applications, called Automation clients. The exposure enables Automation clients to automate certain functions by directly accessing objects and using the services they provide. Automation servers and

[1] http://www.ansys.com/it-IT/products/electronics/ansys-hfss
[2] https://www.cst.com/products/cstmws
[3] https://mathworks.com/products/matlab.html

clients use COM interfaces that are always derived from IDispatch and take and return a specific set of data types called Automation types [4].

In the next the application client is MatLab and the application server is HFSS. Thanks to the OLE automation it is possible to write a script which draw a certain number of cavities and for each of them the radius, for example, is slightly different from the previous one.

A.2 Basic Commands and MatLab Wrapper

The function exposed from the server application should be documented in reference manual in order to develop an automation script. For HFSS they are listed in the scripting manual found inside the installation folder and they are written in Visual Basic for Application (VBA). The built-in functions cover all the possible action offered from the User Interface (UI). For example it is possible to draw the geometric primitive (like box, cylinder, sphere, ...), define an analysis, start the simulation and so on. The following function creates a cylinder when all the arguments are provided:

```
Syntax: CreateCylinder <CylinderParametersArray>,
<AttributesArray>
Return Value: The name of the newly created object.
Parameters: <CylinderParametersArray>
Array("NAME:CylinderParameters",
"XCenter:=", <value>,
"YCenter:=", <value>,
"ZCenter:=", <value>,
"Radius:=", <value>,
"Height:=", <value>,
"WhichAxis:=", <string>
"NumSides:=", "<integer>")
```

the function name is *CreateCylinder* and the argument that must be provided are: the center of the cylinder for the three axes, the radius, the height, the axis orientation and how many side it should have. But, before it is possible to start the design of the model some preliminary lines of codes have to be written. The first step is the setup of the client-server link:

```
oAnsoftApp = actxserver('AnsoftHfss.HfssScriptInterface');
```

the MatLab function *actxserver* creates a local OLE Automation server of the Programmatic Identifier (ProgId) which is the argument. The ProgId is specified in the software

[4] Online Resource https://msdn.microsoft.com/en-us/library/dt80be78.aspx

reference manual and for HFSS is *AnsoftHfss.HfssScriptInterface*. From this point it is possible to send (and receive) data to HFSS through MatLab. For example, it is possible to create a new project with the following lines of code:

```
oDesktop = oAnsoftApp.GetAppDesktop();
invoke(oDesktop,'NewProject');
oProject = oDesktop.GetActiveProject ( ) ;
oProject.InsertDesign('HFSS', 'HFSSDesign1', 'DrivenModal', '' ) ;
oDesign = oProject.SetActiveDesign('HFSSDesign1') ;
oEditor = oDesign.SetActiveEditor('3D Modeler') ;
```

the first line open the UI of the server application, then a new project is created and set as active. An HFSS project can store more design and at least one must be present: the fourth line create a driven modal design and it set as the active one. The last line of the above portion of the code declares the 3D modeler editor. This modeler can call the draw functions. The following object are already used in this code: the *oDesktop*, *oProject*, *oDesign* and the *oEditor*. The first behaves on the top of the others, while the second is in the middle and the last is the one with the lowest scope. The understanding of this hierarchy is crucial to develop an OLE script:

1. *oDesktop* first level object. It behaves on the application itself. It can create or open project and show the UI of the software

2. *oProject* second level object. It acts on the project variable, like the project type (driven modal, eigenmode, ...). It is called by the *oDesktop* editor

3. *oDesign* third level object. It operates on the designs of the project and therefore it is defined by the *oProject* editor.

4. *oEditor* fourth level object. It works on modelling parts of the design, For example it sets the active modeler for the drawing of the geometric primitives.

The VBA script can be directly written with a text editor. However, an interesting and more simple option is available. It is possible to record a VBA script while the user deals with the simulation set-up. The produced code can be converted to a MATLAB code. The following rules should be adopted to translate the code from the VBA language to the MATLAB one:

- replace all *Array(* with *}*
- replace all " with ‘
- replace all _ with ...

- replace all *)* with *}*
- replace *oEditor.Command Array(“* with *invoke(Editor,'Command',*
- add at the end a round parenthesis *)* for closing of the invoke argument

because all the rules are simple find and replace operations the wrapped code production is straightforward. For example, a cylinder can be designed in HFSS with the following VBA code:

```
oEditor.CreateCylinder Array("NAME:CylinderParameters", "XCenter:=", "0mm", "YCenter:=", _
"0mm", "ZCenter:=", "0mm", "Radius:=", "2mm", "Height:=", "1mm", "WhichAxis:=", _
"Z", "NumSides:=", "0"), Array("NAME:Attributes", "Name:=", "Cylinder1", "Flags:=", _
"", "Color:=", "(143 175 143)", "Transparency:=", 0, "PartCoordinateSystem:=", _
"Global", "UDMId:=", "", "MaterialValue:=", "" & Chr(34) & "vacuum" & Chr(34) & "", _
"SolveInside:=", true)
```

which can be wrapped to MATLAB code by following the above rules:

```
invoke (oEditor, 'CreateCylinder', {'NAME:CylinderParameters', 'XCenter:=', '0mm', 'YCenter:=', ...
'0mm', 'ZCenter:=', '0mm', 'Radius:=', '2mm', 'Height:=', '1mm', 'WhichAxis:=', ...
'Z', 'NumSides:=', '0'}, {'NAME:Attributes', 'Name:=', 'Cylinder1', 'Flags:=', ...
'', 'Color:=', '(143 175 143}', 'Transparency:=', 0, 'PartCoordinateSystem:=', ...
'Global', 'UDMId:=', '', 'MaterialValue:=', '' & Chr(34} & 'vacuum' & Chr(34} & '', ...
'SolveInside:=', true})
```

A.3 Output Variables

To take full advantage of the two-way communication between HFSS and MATLAB the user should define some output variables in the HFSS simulation. Output variables can be defined from the computed results. For example, for a dispersion diagram calculation the frequency of the computed eigenmode is an useful output variable. They can be defined within the MATLAB script. For example the following portion of the code defines two output variables for the first two evaluated eigenmodes:

```
oDesign = oProject.SetActiveDesign('HFSSDesign1');
oModule = oDesign.GetModule('OutputVariable');
invoke(oModule, 'CreateOutputVariable', 'mode_1', 're(Mode(1))', ...
'Setup1 : LastAdaptive',...
'Eigenmode Parameters', {})
mode_1=invoke(oModule, 'GetOutputVariableValue', 'mode_1','',...
    'Setup1 : LastAdaptive', 'Eigenmode Parameters',{});
invoke(oModule, 'CreateOutputVariable', 'mode_2', 're(Mode(2))', ...
'Setup1 : LastAdaptive',...
'Eigenmode Parameters', {})
```

```
mode_2=invoke(oModule, 'GetOutputVariableValue', 'mode_2','',...
     'Setup1 : LastAdaptive', 'Eigenmode Parameters',{});
```

the resonant frequency of the two modes are now inside the MATLAB variables *mode_1* and *mode_2*. With this method it is possible to export the results from HFSS to the MATLAB code.

Appendix B

General Particle Tracer Scripts

In this appendix the beam dynamics results are presented. They have been obtained by a numerical code: General Particle Tracer (GPT)[1]. A brief explanation of the code and of the scripts used for the simulations will follow. Afterwards the simulation results are presented.

B.1 The GPT Code

A simple beam dynamics analysis has been carried out with the General Particle Tracer software and an in-house MATLAB code for post-processing of the data. This software allows a tracking simulation of a charged particle moving inside a time varying electromagnetic field.

A particle tracer code is able to estimate the position and the velocity of a certain number of particles in electromagnetic fields. At the moment, it is not possible to simulate in a reasonable amount of time with a common desktop PC a *real* bunch where each particle has an elementary charge. Therefore to reduce the computational effort equivalent macro-particles with a value of the charge higher of the elementary one are used. Typically tens or hundreds of macro-particles are simulated with desktop PC at the time of writing. The position and the velocity of these are updated for each time step by using these equations:

$$\frac{d\overrightarrow{p_i}}{dt} = \overrightarrow{F_i} \tag{B.1}$$

and

$$\frac{d\overrightarrow{x_i}}{dt} = \frac{\overrightarrow{p_i}c}{\sqrt{\overrightarrow{p_i^2} + m_i^2 c^2}} \tag{B.2}$$

[1] http://www.pulsar.nl/gpt/

where $\overrightarrow{x_i}$ and $\overrightarrow{p_i}$ are the position and the momentum of the i-particle and $\overrightarrow{F_i}$ is the combination of the electrostatic and Lorentz force:

$$\overrightarrow{F_i} = q(\overrightarrow{E_i} + \overrightarrow{v_i} \times \overrightarrow{B_i}) \tag{B.3}$$

In order to solve the equations initial and boundary condition should be provided, which are the initial velocity and position of each particle and the electromagnetic fields. A Runge-Kutta fifth order scheme is used to solve the differential equations. A variable time-step is used to increase the numerical stability without affecting the performances [63].

GPT is a tracking code, therefore the fields self generated by the particles are not calculated with one exception: the space charge effect. Due to the Coulomb interaction the particles are mutually rejected and move away from each neighbours. The space charge effect is simulated by the code and for low energy and high *density* charge beam should be taken into account.

B.2 Scripts Description

A schematic description of the GPT executable is shown in fig. B.1. The input file is an ASCII file with the most important instructions for the simulation process. Other files which are usually provided by the user are the multiple run (MR) file and the external field maps.

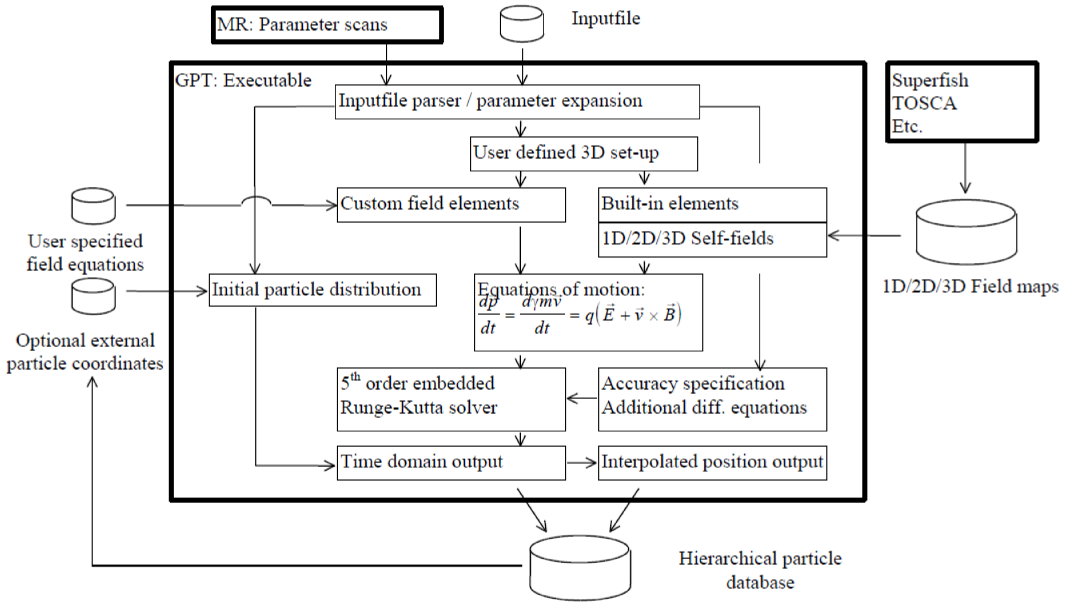

FIGURE B.1: Schematic of the GPT executable (from the reference manual).

The MR file allows to simulate the same structure for different value of a parameters in an automated fashion. It also possible to run an optimization routine which will use the space parameters defined in this file. The external fields are generated with an EM solver and imported within GPT after a conversion from ASCII format (with a specified syntax) to a binary internal one with a built-in routine. It is also possible to use pre-built elements like magnetic lens or simple configuration of TW accelerating fields. The syntax for these elements can be found in the reference manual.

Most of the informations for the simulations are stored in the input file. A brief description of a script used in this thesis will follow. As first step the beam parameters (energy, bunch radius and length and the total) are provided:

```
# Basic beam parameters
Eo  = energy;  # Energy [MeV]
G = Eo/0.511; # Corresponding Lorentz factor G
Beta  = sqrt(1-G^-2);  # Corrsponding normalized velocity
rxy  = 0.1e-3;  # Bunch radius [m]
zlen  = 1e-3;  # Bunch length [m]
Qtot  = charge;  # Total charge in tlen [C]
```

Energy and charge are specified by a variable and the value of them is provided in the multiple run file. Which is a simple ASCII file with a row for each parameters with the following syntax:

```
Variable Initial_Value Final_Value Step_Size
```

for example to specify an energy value from 10 MeV to 100 MeV with a step increasing size of 5 MeV, for a total number of 21 simulation, the entry line is:

```
energy 10 100 5
```

Then the total number of macro-particles is defined

```
# Simulation parameters
nps = 10000 ; # Number of particles
```

and the initial condition of the bunch is defined with the following lines. The first row defines the bunch with the value provided in the basic beam parameters. Then the transverse dimension, the azimuthal distribution and total length is defined. The last two entries allow to define the energy spread and the initial emittance of the beam.

```
# Start bunch
setparticles("beam",nps,me,qe,Qtot) ;
```

```
setrxydist("beam","g",0,rxy,0,3.0) ;
setphidist("beam","u", 0, 2*pi) ;
setzdist("beam","g", 0, 300e-6, 3.0, 3.0 ) ;
setGdist("beam","u", G, 0 ) ;
setGBxemittance("beam",1e-6);
```

In the case of a single particle simulation (which can be useful in some context, for example to clearly see particle trace in the structure) the above section should be substituted with the following instruction:

```
# Single Particle
#setstartpar("beam",0,0.1e-3,0, 0,0,100) ;
```

The use of the space charge routine can be enabled with the following line:

```
# Space-charge
if( Qtot!=0 ) spacecharge3Dmesh() ;
```

The space charge evaluation is time consuming for tens of thousand of particles. Therefore it should be enabled only when necessary.

A simple drift tube with a radius equal (or smaller for more robust evaluation) the small aperture passed by the beam is added. It allows a *safe* removal of the particles which go beyond the its radius. The longitudinal length of the structure is specified with the *zend* variable.

```
# Remove Particles
zend = 0.21;
drift("wcs", "z", zend/2, zend,0.7e-3);
```

The external field maps are imported and the angular frequency are specified with these entries:

```
#Import Field
fx=11.424e9; #X-band
w=2*pi*fx; #Angular frequency
phi=phx;
ffac=1;
map3D_Ecomplex("wcs","z",0.0065,"E_complex_vec_complete_structure.gdf",...
"x","y","z","ExRe","EyRe","EzRe","ExIm","EyIm","EzIm",ffac,phi/deg,w) ;
map3D_Hcomplex("wcs","z",0.0065,"H_complex_vec_complete_structure.gdf",...
"x","y","z","HxRe","HyRe","HzRe","HxIm","HyIm","HzIm",ffac,phi/deg,w) ;
```

A scaling factor *ffac* is added. By this way it is possible to simulate a field enhancement due to more RF power provided.

The accuracy of the solution is specified with these instruction:

```
########
#OUTPUT#
########
acc=4;
accuracy(acc);
zstart = 0;
```

Its value defines the maximum time step and therefore a trade-off between simulation time and accuracy must be find.

At the end a sufficient number of screens is specified. For each of these location the solver stores position and velocity of the particles.

```
#########
#SCREENS#
#########
nscreens=201;
dz_step = (zend-zstart)/nscreens;
if(nscreens>1)   snapshot(zstart/c,zend/c,dz_step/c);
if(nscreens==1)  snapshot(zend/c);
```

B.3 Beam Dynamics Analysis

In a tracking code the simulation is not self-consistent with the electromagnetic field produced by the moving charge. In the following simulations only the electrostatic field of the electrons has been computed in order to evaluate the so called space-charge effect. This approximation is valid when the bunch charge is relatively small, i.e. the scattered electromagnetic fields of the moving electrons are order of magnitude lower of the RF fields. For this reason a low charge of 50 pC has been used in the following.

The first step of the beam dynamics analysis is the calculation of the accelerating phase, i. e. the phase which maximize the acceleration of the bunch. This value depends on the reference phase taken as zero-phase in the simulations. For this case the maximum of the accelerating gradient is found for 85 deg, i.e. the zero phase is 5 degree. The E_{acc} has been calculated before (see table 4.4) and it is equal to 80.4 MV/m. Therefore in the case of a 16 cells structure with approximate length of 21 cm the energy gain is equal to 16.9 MeV. From the numerical simulations the energy gain is equal to 16.5 MeV. This minor difference with the analytical case will be clarified in the next.

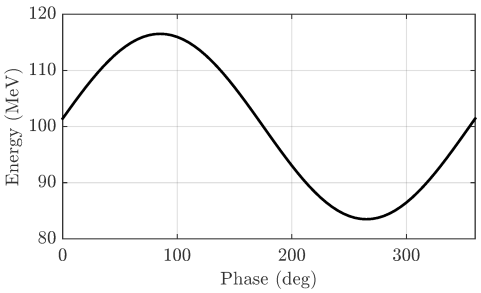

FIGURE B.2: Energy as function of the injection phase. Maximum energy gain is found for 85 deg of the injection phase.

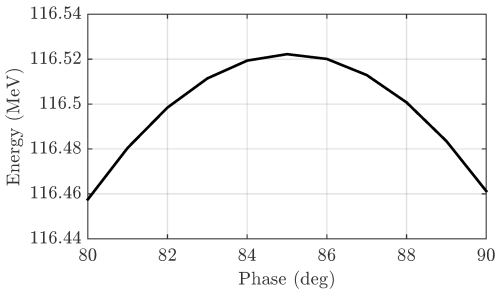

FIGURE B.3: The energy gain computed is equal to 16.5 MeV. A value very close to the analytical calculation.

The propagation of the electron bunch inside the PCAS is affected by the presence of the coupling holes. Due to the interpolation scheme, for each cell, the coupling hole is only one-sided. This leads to a dipolar and high order mode field components. The dipolar component is typically the most dangerous because it is responsible for a transverse kick of the whole bunch. However, for the PCAS here presented, the transverse kick is not so much intense, at least for high energy bunch (>100 MeV). The offset angles have been calculated for three energy cases 100, 20 and 5 MeV, see fig. B.4 and B.5. They are 9.5, 38 and 95 μrad in the x-plane and 9.5, 47 and 120 μrad in the y-plane for a bunch injected in the axis of the structure with an initial energy of 100, 20 and 5 MeV respectively and a charge of 50 pC. Even for the worst case found after one meter, a relative large value for a X-band section, the offset from axis is the 120 μm, equal to the 12% of the radius of iris meanwhile for the best case the offset is 1%. The propagation of the bunch is not exactly on the axis of the PCAS and for this reason the integrated voltage seen by the bunch is lower. That justifies the difference between the analytical energy gained (16.9 MeV) with the numerical value (16.5 MeV).

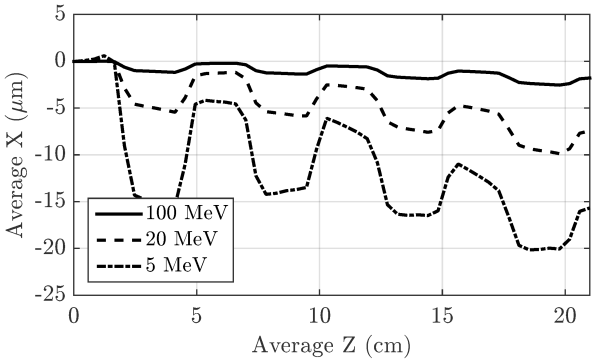

FIGURE B.4: Average position of the particle of the simulated bunch in the x-plane versus the position of the mass centre of the bunch.

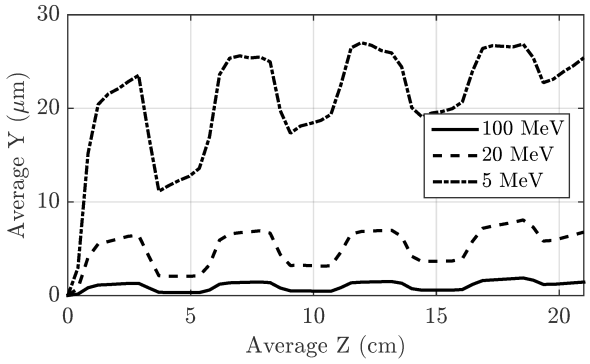

FIGURE B.5: Average position of the particle of the simulated bunch in the y-plane versus the position of the mass centre of the bunch.

In fig. B.6 and B.7 the envelope in the x and y planes versus the position of mass centre of the bunch are shown. The transverse spot size decreases during the acceleration as predicted by the beam dynamics theory [31, pp. 167]. The initial longitudinal momentum p_0 is increased during the acceleration $p_f = p_o + p_a$, where p_a is the momentum gained due to RF acceleration. The transverse momentum in instead roughly the same after the passage in the accelerating structure. The shrinking of the transverse size during acceleration can be heuristically demonstrated with the following inequality $x' = p_f/p_{\|} > x'_0 = p_0/p_{\|}$, because $x'/x'_0 > 1$ the transverse spot size is shrunk. The reduction of the spot size is from 100 μm to 89, 66 and 44 μm in the x plane and 91, 72 and 49 μm in the y plane. The reduction is greater at lower energy because the gained longitudinal momentum is, in percentage, greater at low energy.

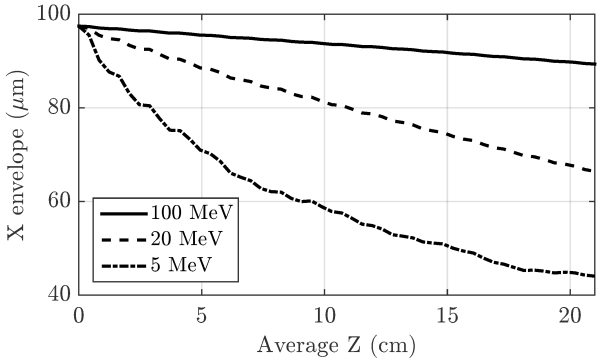

FIGURE B.6: Dimension of the bunch envelope in the x-plane versus the position of the mass centre of the bunch.

The "quality" of a beam can be measured with a quantity called emittance. The ideal beam is a beam with a laminar flow. In this regime every particle moves in a laminar fashion, i.e. for each couple of particles the relative distance between them remains unchanged. In the transverse plane a measurable quantity called emittance is used for

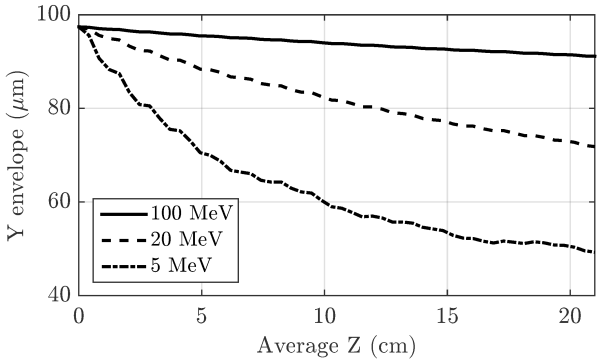

FIGURE B.7: Dimension of the bunch envelope in the y-plane versus the position of the mass centre of the bunch.

the evaluation of the variation of the relative distance. It is measured in mm mrad: for example an emittance of 1 mm mrad means that two particles after one millimetre the relative angle between them is increased by one milli-radian[2]. In an accelerating structure because the longitudinal momentum is not conserved the emittance normalized by the energy is commonly used. The emittance has been chosen equal to 1 mm mrad at the entrance of the PCAS. A finite initial emittance is required in order to avoid un-physical results. The normalized emittance slowly grows in the PCAS with a rate of 10% after 10 cm with a greater grow rate for low energy beam, see fig B.8.

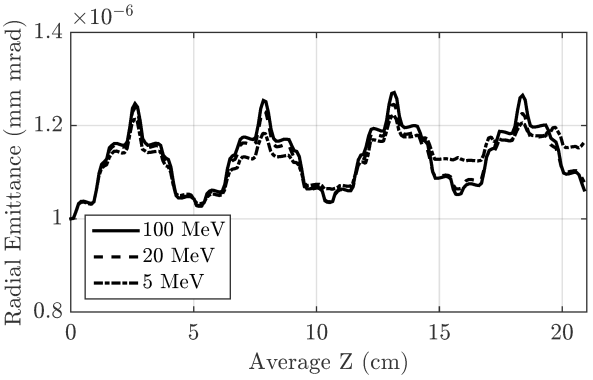

FIGURE B.8: Radial emittance value in the x-plane versus the position of the mass centre of the bunch.

The emittance in the longitudinal dimension (z axis) is often called energy spread defined as the relative difference in energy of the particles. The main source of energy spread in a LINAC is the curvature of the RF electric field. Even for a very short bunch on crest the particles on the head and tail of the bunch "see" a lower field respect to centre of the bunch. For the PCAS the energy spread is under 0.1% for high energy beam and below 0.5% for low energy beam after 20 cm of acceleration.

[2]In this thesis it is assumed the common value of emittance divided by π.

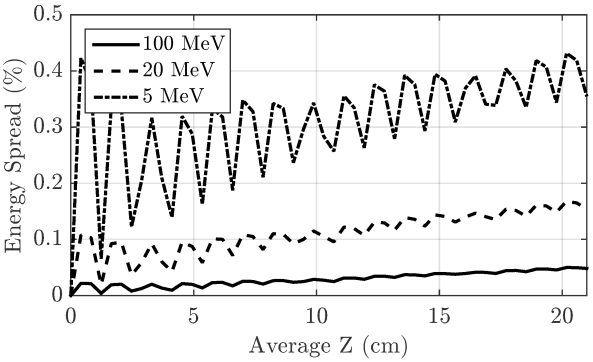

FIGURE B.9: Energy spread versus the length of section normalized to the energy.

For the sake of completeness the input spot size and the output spot size for the three energy investigated are here reported in the fig. B.10. For 100 MeV no evident deformation of the spot is present.

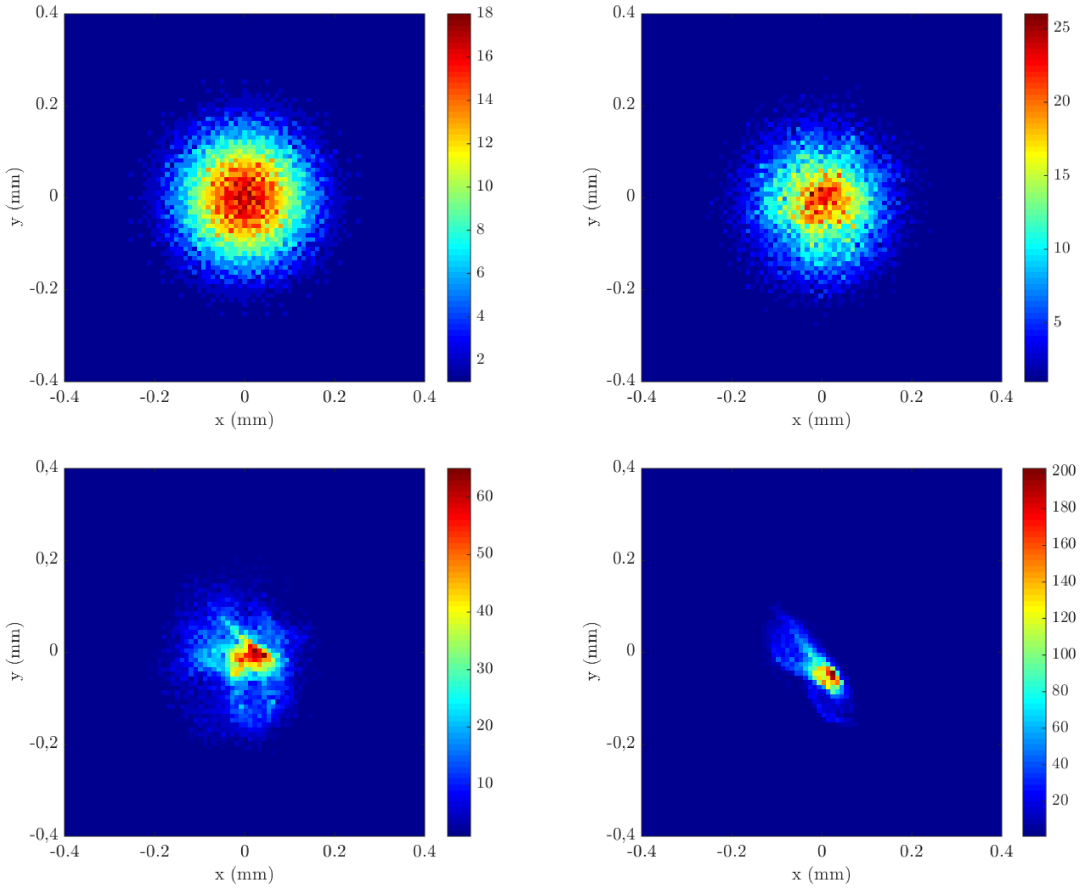

FIGURE B.10: Spot size of the bunch at the beginning of section (top left) and the at the output of the PCAS for 100 (top right), 20 (bottom left) and 5 (bottom right) MeV initial energy.

Bibliography

[1] Thomas P Wangler. *RF Linear Accelerators*. John Wiley & Sons, 2008.

[2] Gregory A Loew and Richard Talman. Elementary principles of linear accelerators. In *AIP Conference Proceedings*, volume 105, pages 1–91. AIP, 1983.

[3] K Halbach, RF Holsinger, WE Jule, and DA Swenson. Properties of the cylindrical rf cavity evaluation code superfish. In *Proc. of 1976 Proton Linac Conf.*, page 122, 1976.

[4] PN Ostroumov and KW Shepard. Multiple-charge beam dynamics in an ion linac. *Physical review special topics-accelerators and beams*, 3(3):030101, 2000.

[5] O Adriani, S Albergo, D Alesini, M Anania, D Angal-Kalinin, P Antici, A Bacci, R Bedogni, M Bellaveglia, C Biscari, et al. Technical design report eurogammas proposal for the eli-np gamma beam system. *arXiv preprint arXiv:1407.3669*, 2014.

[6] Alexej Grudiev, Daniel Schulte, and Walter Wuensch. Optimum frequency and gradient for the clic main linac accelerating structure. Technical report, 2006.

[7] E Somersalo, P Yla-Oijala, and D Proch. Analysis of multipacting in coaxial lines. In *Particle Accelerator Conference, 1995., Proceedings of the 1995*, volume 3, pages 1500–1502. IEEE, 1995.

[8] L Ge, C Adolphsen, LK Ko, Z Li, C Ng, G Schussman, F Wang, B Rusnak, et al. Multipacting simulations of ttf-iii power coupler components. In *Particle Accelerator Conference, 2007. PAC. IEEE*, pages 2436–2438. IEEE, 2007.

[9] Massimo Dal Forno, Valery Dolgashev, Gordon Bowden, Christine Clarke, Mark Hogan, Doug McCormick, Alexander Novokhatski, Bruno Spataro, Stephen Weathersby, and Sami G Tantawi. rf breakdown tests of mm-wave metallic accelerating structures. *Physical Review Accelerators and Beams*, 19(1):011301, 2016.

[10] Parry Y Chen, Ross C McPhedran, C Martijn de Sterke, Chris G Poulton, Ara A Asatryan, Lindsay C Botten, and Michael J Steel. Group velocity in lossy periodic structured media. *Physical Review A*, 82(5):053825, 2010.

[11] Richard B Neal and John P Blewett. The stanford two-mile accelerator. *Physics Today*, 23:76, 1970.

[12] David Alesini. Power coupling. *arXiv preprint arXiv:1112.3201*, 2011.

[13] Roger H Miller. Comparison of standing wave and traveling wave structures. In *Conf. Proc.*, volume 860602, page 200, 1986.

[14] GA Loev, RH Miller, RA Early, and KL Bane. Computer calculation of travelling-wave periodic structure properties. 1979.

[15] Mattia Schaer, Alessandro Citterio, Paolo Craievich, Sven Reiche, Lukas Stingelin, and Riccardo Zennaro. rf traveling-wave electron gun for photoinjectors. *Phys. Rev. Accel. Beams*, 19:072001, Jul 2016. doi: 10.1103/PhysRevAccelBeams.19.072001. URL https://link.aps.org/doi/10.1103/PhysRevAccelBeams.19.072001.

[16] W Wuensch. Progress in understanding the high-gradient limitations of accelerating structures. Technical report, 2007.

[17] Walter Wuensch. Observations about rf breakdown from the clic high-gradient testing program. In *AIP Conference Proceedings*, volume 877, pages 15–21. AIP, 2006.

[18] A Descoeudres, T Ramsvik, S Calatroni, M Taborelli, and W Wuensch. Dc breakdown conditioning and breakdown rate of metals and metallic alloys under ultra-high vacuum. *Physical Review Special Topics-Accelerators and Beams*, 12(3):032001, 2009.

[19] JW Wang and GA Loew. Field emission and rf breakdown in high gradient room temperature linac structures. In *Talk given at*, number SLAC-PUB-7684, pages 768–794, 1997.

[20] Hans Heinrich Braun, Steffen Döbert, Ian H Wilson, and Walter Wuensch. Frequency and Temperature Dependence of Electrical Breakdown at 21, 30 and 39 GHz. Jun 2003. URL http://cds.cern.ch/record/625408.

[21] Valery Dolgashev, Sami Tantawi, Yasuo Higashi, and Bruno Spataro. Geometric dependence of radio-frequency breakdown in normal conducting accelerating structures. *Applied Physics Letters*, 97(17):171501, 2010.

[22] Ralph Howard Fowler and L Nordheim. Electron emission in intense electric fields. In *Proceedings of the Royal Society of London A: Mathematical, Physical and Engineering Sciences*, volume 119, pages 173–181. The Royal Society, 1928.

[23] Lisa Laurent, Sami Tantawi, Valery Dolgashev, Christopher Nantista, Yasuo Higashi, Markus Aicheler, Samuli Heikkinen, and Walter Wuensch. Experimental study of rf pulsed heating. *Physical review special topics-accelerators and beams*, 14 (4):041001, 2011.

[24] Faya Wang, Chris Adolphsen, and Christopher Nantista. Performance limiting effects in x-band accelerators. In *AIP Conference Proceedings*, volume 1299, pages 280–285. AIP, 2010.

[25] Alexej Grudiev, S Calatroni, and W Wuensch. New local field quantity describing the high gradient limit of accelerating structures. *Physical Review Special Topics-Accelerators and Beams*, 12(10):102001, 2009.

[26] Mohamed El Khaldi and Luca Garolfi. Rf design of a high gradient s-band travelling wave accelerating structure for thomx linac. In *IPAC'15, the sixth International Particle Accelerator Conference,*, 2015.

[27] WZ Bruno and AK Semyon. Impedance and wakes in high-energy particle accelerators, 1998.

[28] L Palumbo, Vittorio G Vaccaro, and M Zobov. Wake fields and impedance. *arXiv preprint physics/0309023*, 2003.

[29] Alexander Wu Chao, Karl Hubert Mess, Maury Tigner, and Frank Zimmermann. *Handbook of accelerator physics and engineering*. World scientific, 2013.

[30] A Mosnier. Instabilities in linacs. Technical report, CERN, 1993.

[31] Martin Reiser. *Theory and design of charged particle beams*. John Wiley & Sons, 2008.

[32] G Schaffer. High power UHF components for desy. *IEEE Transactions on Nuclear Science*, 12(3):208–212, 1965.

[33] RM Sundelin, JL Kirchgessner, and M Tigner. Parallel coupled cavity structure. *IEEE Transactions on Nuclear Science*, 24(3):1686–1688, 1977.

[34] ON Brezhnev, PV Logatchev, VM Pavlov, OV Pirogov, SV Shiyankov, Ju D Chernousov, VI Ivannikov, and IV Shebolaev. Parallel-coupled accelerating structures. In *Proceedings of LINAC*, pages 215–217, 2002.

[35] Jeffrey Neilson, Sami Tantawi, and Valery Dolgashev. Design of rf feed system for standing-wave accelerator structures. In *AIP Conference Proceedings*, volume 1299, pages 463–466. AIP, 2010.

[36] Valery Dolgashev. Traveling wave linear accelerator with rf power flow outside of accelerating cavities. In *28th Linear Accelerator Conf.(LINAC'16), East Lansing, MI, USA, 25-30 September 2016*, pages 48–51. JACOW, Geneva, Switzerland, 2017.

[37] Guide periodiche. URL http://microwave.unipv.it/pages/complementi_di_campi/guide_periodiche_new.pdf.

[38] Christopher Nantista, Sami Tantawi, and Valery Dolgashev. Low-field accelerator structure couplers and design techniques. *Physical Review Special Topics-Accelerators and Beams*, 7(7):072001, 2004.

[39] Wolfgang Maichen. *Digital timing measurements: from scopes and probes to timing and jitter*, volume 33. Springer Science & Business Media, 2006.

[40] Yu D Chernousov, V Ivannikov, I Shebolaev, A Barnyakov, A Levichev, and V Pavlov. Localization of the rf breakdown in the parallel coupled accelerating structure. 2012.

[41] David M Pozar. *Microwave engineering*. John Wiley & Sons, 2009.

[42] Sophocles J Orfanidis. *Electromagnetic waves and antennas*. Rutgers University New Brunswick, NJ, 2002.

[43] AS Sharkhov VM Pavlov, AS Bogomolov. Multistage slowing down structure, Russian Patent, SU1295466A1, 12/05/1985.

[44] JW Wang, GA Loew, RJ Loewen, Ronald D Ruth, AE Vlieks, I Wilson, and W Wuensch. SLAC/CERN high gradient tests of an X-band accelerating section. In *Particle Accelerator Conference, 1995., Proceedings of the 1995*, volume 1, pages 653–655. IEEE, 1995.

[45] Valery A Dolgashev, Sami G Tantawi, Steven H Gold, and Gregory S Nusinovich. Effect of rf parameters on breakdown limits in high-vacuum X-band structures. In *AIP Conference Proceedings*, volume 691, pages 151–165. AIP, 2003.

[46] Hao Zha, Valery Dolgashev, and Alexej Grudiev. Rf design of the clic structure prototype optimized for manufacturing from two halves. Technical report, 2015.

[47] Alexej Grudiev and Walter Wuensch. Design of the clic main linac accelerating structure for clic conceptual design report. Technical report, 2010.

[48] Robin Rajamaki. *Vacuum arc localization in CLIC prototype radio frequency accelerating structures*. PhD thesis, Helsinki Inst. of Phys., 2016.

[49] Kek-slac international study group on linear colliders. Technical report, 1998-2004.

[50] ZD Farkas, TL Lavine, A Menegat, AE Vlieks, JW Wang, and PB Wilson. Two-klystron binary pulse compression at slac. In *Particle Accelerator Conference, 1993., Proceedings of the 1993*, pages 1208–1210. IEEE, 1993.

[51] M Ferrario, V Fusco, M Migliorati, and L Palumbo. Emittance degradation due to wake fields in a high brightness photoinjector. *International Journal of Modern Physics A*, 22(23):4214–4234, 2007.

[52] SA Heifets. Diffractive model of the high-frequency impedance. *Physical review D*, 40(9):3097, 1989.

[53] JC Sheppard, MJ Lee, MC Ross, JT Seeman, RF Stiening, and MD Woodley. Beam steering in the slc linac. *IEEE Transactions on Nuclear Science*, 32(5):2180–2182, 1985.

[54] Peter Forck, D Liakin, and P Kowina. Beam position monitors. 2009.

[55] Shigeru Okabe and Tatsuo Tabata. Beam position monitor for accelerators. *Review of Scientific Instruments*, 36(1):97–98, 1965.

[56] F Marcellini, M Serio, A Stella, and M Zobov. Daϕne broad-band button electrodes. *Nuclear Instruments and Methods in Physics Research Section A: Accelerators, Spectrometers, Detectors and Associated Equipment*, 402(1):27–35, 1998.

[57] V Sargsyan. Comparison of stripline and cavity beam position monitors. Technical report, CM-P00047837, 2004.

[58] Peter Forck, Piotr Kowina, and Dmitry Liakin. Beam position monitor: Detector principle, hardware and electronics. *Gesellschaft für Schwerionenforschung, Darmstadt, Germany*, 2008.

[59] Ji Ho Jang, Hyeok-jung Kwon, Dae-il Kim, Han-sung Kim, Kyung-jean Min, Bumsik Park, Kyung Tae Seol, Sung Su Cha, and Yong Sub Cho. Design and fabrication of a prototype stripline bpm for pefp beam lines. In *Transactions of the Korean Nuclear Society Spring Meeting, Taeback*, 2011.

[60] Giovanni Franzini, Fara Cioeta, Oscar Coiro, Valerio Lollo, Marco Marongiu, Andrea Mostacci, Andriy Nosych, Donato Pellegrini, Stefano Pioli, Luca Sabato, et al. Analysis and correction of geometrical non-linearities of eli-np bpms on position and current measurements. In *8th Int. Particle Accelerator Conf.(IPAC'17), Copenhagen, Denmark, 14-19 May, 2017*, pages 235–237. JACOW, Geneva, Switzerland, 2017.

[61] Giovanni Castorina, Andrea Mostacci, Marco Maroungiu, Giovanni Franzini, Bruno Spataro, and Andriy Nosych. Stripline beam position monitor modelling and simulations for charge measurements. In *International Beam Instrumentation Conf. (IBIC'17), Grand Rapids, USA, 20-24 August*, 2017.

[62] Andriy Nosych, Fara Cioeta, Carles Colldelram, Alejandro Crisol, Antonio Falone, Andrea Ghigo, Ubaldo Iriso, Andrea Mostacci, Angel Olmos, Mario Serio, et al. Measurements and calibration of the stripline bpm for the eli-np facility with the stretched wire method. In *4th International Beam Instrumentation Conference (IBIC2015), Melbourne, Australia, 13-17 September 2015*, pages 423–427. JACOW, Geneva, Switzerland, 2016.

[63] William H Press. *Numerical recipes 3rd edition: The art of scientific computing*. Cambridge university press, 2007.